Transactions on Intelligent Welding Manufacturing

Volume III No. 3 2019

Springer

Transactions on Intelligent Welding Manufacturing

Editors-in-Chief

Shanben Chen
Shanghai Jiao Tong University
Shanghai, China

Yuming Zhang,
Department of Electrical
and Computer Engineering
University of Kentucky
Lexington, KY, USA

Zhili Feng,
Oak Ridge National Laboratory
Oak Ridge, USA

Honorary Editors

G. Cook, USA
K. L. Moore, USA
Ji-Luan Pan, PRC
S. A. David, USA
S. J. Na, KOR
Lin Wu, PRC
Y. Hirata, JAP
J. Norrish, AUS
T. Lienert, USA
T. J. Tarn, USA

Guest Editors

H. P. Chen, USA
J. C. Feng, PRC
H. J. Li, AUS
X. Q. Chen, NZL
D. Hong, USA
W. Zhou, SGP
D. Du, PRC
X. D. Jiao, PRC
D. Fan, PRC
I. Lopez-Juarez, MEX

Regional Editors

Asia: L. X. Zhang, PRC
America: Y. K. Liu, USA
Australia: Z. X. Pan, AUS
Europe: S. Konovalov, RUS

Associate Editors

Q. X. Cao, PRC
B. H. Chang, PRC
J. Chen, USA
H. B. Chen, PRC
S. J. Chen, PRC
X. Z. Chen, PRC
A.-K. Christiansson, SWE
Z. G. Li, PRC
X. M. Hua, PRC
Y. Huang, USA
S. Konovalov, RUS
W. H. Li, PRC
X. R. Li, USA
Y. K. Liu, USA
L. M. Liu, PRC
H. Lu, PRC
Z. Luo, PRC
G. H. Ma, PRC
Pedro Neto, PRT
G. Panoutsos, UK
Z. X. Pan, AUS
X. D. Peng, NL
Y. Shi, PRC
J. Wu, USA
J. X. Xue, PRC
L. J. Yang, PRC
M. Wang, PRC
S. Wang, PRC
X. W. Wang, PRC
Z. Z. Wang, PRC
G. J. Zhang, PRC
H. Zhang, B, PRC
H. Zhang, N, PRC
L. X. Zhang, PRC
W. J. Zhang, USA

Academic Assistant Editors

J. Cao, PRC
B. Chen, PRC
Y. Luo, PRC
N. Lv, PRC
F. Li, PRC
S. B. Lin, PRC
Y. Shao, USA
Y. Tao, PRC
J. J. Wang, PRC
H. Y. Wang, PRC
S. L. Wang, PRC
J. Xiao, PRC
J. J. Xu, PRC
Y. L. Xu, PRC
C. Yu, PRC
H. W. Yu, PRC
K. Zhang, PRC
W. Z. Zhang, PRC
Z. F. Zhang, PRC

Editorial Staff

Executive Editor (Manuscript and Publication): Dr. Yan Zhang, PRC
Responsible Editors (Academic and Technical): Dr. Na Lv, PRC
Dr. Jing Wu, USA

More information about this series at http://www.springer.com/series/15698

Shanben Chen · Yuming Zhang · Zhili Feng
Editors

Transactions on Intelligent Welding Manufacturing

Volume III No. 3 2019

Springer

Editors
Shanben Chen
Shanghai Jiao Tong University
Shanghai, China

Zhili Feng
Oak Ridge National Laboratory
Oak Ridge, TN, USA

Yuming Zhang
Department of Electrical and Computer Engineering
University of Kentucky
Lexington, KY, USA

ISSN 2520-8519 ISSN 2520-8527 (electronic)
Transactions on Intelligent Welding Manufacturing
ISBN 978-981-15-7214-2 ISBN 978-981-15-7215-9 (eBook)
https://doi.org/10.1007/978-981-15-7215-9

© Springer Nature Singapore Pte Ltd. 2020
This work is subject to copyright. All rights are reserved by the Publisher, whether the whole or part of the material is concerned, specifically the rights of translation, reprinting, reuse of illustrations, recitation, broadcasting, reproduction on microfilms or in any other physical way, and transmission or information storage and retrieval, electronic adaptation, computer software, or by similar or dissimilar methodology now known or hereafter developed.
The use of general descriptive names, registered names, trademarks, service marks, etc. in this publication does not imply, even in the absence of a specific statement, that such names are exempt from the relevant protective laws and regulations and therefore free for general use.
The publisher, the authors and the editors are safe to assume that the advice and information in this book are believed to be true and accurate at the date of publication. Neither the publisher nor the authors or the editors give a warranty, expressed or implied, with respect to the material contained herein or for any errors or omissions that may have been made. The publisher remains neutral with regard to jurisdictional claims in published maps and institutional affiliations.

This Springer imprint is published by the registered company Springer Nature Singapore Pte Ltd.
The registered company address is: 152 Beach Road, #21-01/04 Gateway East, Singapore 189721, Singapore

Editorials

This issue of the Transactions on Intelligent Welding Manufacturing (TIWM) is also selected in part from the high-quality contributions recommended by "The 2019 International Workshop on Intelligentized Welding Manufacturing (IWIWM'2019)". It includes one feature article, eight research papers and one short paper.

The featured article in this issue, "The Review of Spectrum Detection and Ultrasonic Vibration Control of Porosity Defects in Aluminum Alloy Welding", is contributed by Jingyuan Xu and Shanben Chen, from Shanghai Jiao Tong University. This paper discusses the research status of pore detection and control methods in aluminum alloy welding. The development prospect of spectral detection technology and ultrasonic-assisted welding and the advantages compared with the traditional methods are also analyzed.

The first selected paper of research articles, "Microstructure and Mechanical Properties of TC4 Titanium Alloy by Electron Beam Free-form Fabrication", is contributed by Wenjun Sun, Liming Ke, Shanlin Wang, Wende Bu, a research team from Nanchang Hangkong University. In this paper, TC4 titanium alloy was investigated as the research materials, and it was particular to research on the uniformity of TC4 titanium alloy by electron beam free-form fabrication. The structure was manufactured by controlling the heat input to reveal the microstructural evolution and analyze its mechanical properties, and the heat treatment was utilized to control the microstructural uniformity for improving its comprehensive mechanical properties.

For the second research paper, "Weld Flaw Recognition with Improved Convolutional Neural Network", is contributed by a research team from Lanzhou University of Technology. This paper uses simple linear iterative clustering (SLIC) algorithm and the improved exponential linear unit (ELU) activation function to construct CNN model for weld flaw detection image recognition. Through the extraction of the interest region of weld detection image and the establishment of the CNN model described in this paper, the results show that the proposed method has better performance than the traditional convolution neural network in feature extraction, training time and recognition accuracy of weld flaw detection image.

The third research paper titled "Mask R-CNN-based Welding Image Object Detection and Dynamic Modeling for WAAM" is contributed by jointed research teams from University of Wollongong and Shanghai Jiao Tong University. This paper studies wire arc additive manufacturing. In this paper, researchers develop a passive visual sensing system for a robotic WAAM system. A new deep learning technique (Mask R-CNN) is proposed to detect and segment the melt pool area, and the width of melt pool can be measured based on the coordinate of the bounding rectangle.

The fourth research paper, "Research on Fuzzy Comprehensive Evaluation of Seam Quality in Double-Wire Double-Pulsed MIG High-Speed Welding" is from Huangsheng Xie, Zhihe Fu, Jiaxiang Xue and Yu Hu, affiliated to Longyan University, China. In this paper, the quantitative evaluation method of the welding stability and quality based on current sample entropy and current probability density distribution function were explored. The MIG high-speed welding process stability and weld quality were quantitatively evaluated. The current sample entropy algorithm was used to analyze the effects of twin wire welding speed, waveform modulation mode and low frequency on welding stability.

The fifth research paper, "Welding Deviation Extraction during K-TIG Welding Based on K-means Clustering" is from South China University of Technology. In this paper, a novel welding deviation visual inspection method is proposed. A high dynamic range camera is used to capture the welding images. The experiment proves that the proposed algorithm can realize the automatic identification of K-TIG welding deviation.

The sixth research paper, "Thermal Characteristics of Narrow Gap GMA Welding at Vertical Position with Arc Swinging and Shifting", is contributed by jointed research teams from Zhejiang Normal University and Harbin University of Science and Technology. This paper studies thermal characteristics of narrow gap GMA welding. The results show that the line energy of the process is pulsed and alternately assigned to both sides of the sidewall, which lead to a narrow coarse grain heat-affected zone.

The seventh research paper, "Kinematics Analysis of Mechanical Arm of a 10-Joint Tunnel Arch Installation Trolley" is a contribution from Beijing Institute of Petrochemical Technology and Beijing University of Chemical Technology. Kinematics analysis is one of the key technologies to realize automatic installation of supporting steel arch for multi-joint and heavy-load arch centering manipulator. In this paper, through D-H method, the link coordinate system of the trolley manipulator is established, the transformation matrix between the joints is obtained, the forward kinematics model is established, and the initial position and pose of the grab at the end of the manipulator are determined.

The last research paper, "Research of Multi-source Information Sensing Technology in Defect Detection on Automatic Welding", is a contribution from Guangxi University of Science and Technology, Shanghai Jiao Tong University and Beibu Gulf University. In the process of robot welding, the accurate extraction and analysis of the effective feature information in the dynamic process of welding are an effective guarantee for the automation and intelligence of welding. Through the real-time monitoring and analysis of defects, the corresponding features can be extracted to the penetration of the dynamic process of welding.

The short paper, “Research on Resonant High-Voltage Plasma Power Supply” is from Nanchang Hangkong University and South China University of Technology. This paper introduces the working principle of circuit and builds the main circuit model with MATLAB/Simulink to analyze the working process in the circuit.

This issue of TIWM shows the new perspectives and developments in the field of intelligent welding research, as well as the topics related to the IWIWM’2019 conference. The publication of this issue will certainly give readers new inspiration, as we hope so.

Zhili Feng Ph.D.
fengz@ornl.gov
TIWM Editor-in-Chief
Oak Ridge National Laboratory
USA

Contents

Feature Articles

The Review of Spectrum Detection and Ultrasonic Vibration Control of Porosity Defects in Aluminum Alloy Welding 3
Jingyuan Xu and Shanben Chen

Research Papers

Microstructure and Mechanical Properties of TC4 Titanium Alloy by Electron Beam Freeform Fabrication 27
Wenjun Sun, Liming Ke, Shanlin Wang, and Wende Bu

Weld Flaw Recognition with Improved Convolutional Neural Network 45
Ande Hu, Ding Fan, Jiankang Huang, and Zhenya Xu

Mask R-CNN-Based Welding Image Object Detection and Dynamic Modelling for WAAM 57
Chunyang Xia, Zengxi Pan, Shiyu Zhang, Joseph Polden, Huijun Li, Yanling Xu, and Shanben Chen

Research on Fuzzy Comprehensive Evaluation of Seam Quality in Double-Wire Double-Pulsed MIG High-Speed Welding 75
Huangsheng Xie, Zhihe Fu, Jiaxiang Xue, and Yu Hu

Welding Deviation Extraction during K-TIG Welding Based on K-Means Clustering 93
Baori Zhang and Yonghua Shi

Thermal Characteristics of Narrow Gap GMA Welding at Vertical Position with Arc Swinging and Shifting 109
Hu Lan, Huajun Zhang, Jinjun Shao, Gang Li, Rui Pan, and Bin Wang

Kinematics Analysis of Mechanical Arm of a Ten-Joint Tunnel Arch Installation Trolley 125
Long Xue, Junfen Huang, Jiqiang Huang, Kang Huang, Yingyu Cao, and Wei Fang

Research of Multi-source Information Sensing Technology in Defect Detection on Automatic Welding 137
Dapeng Yang, Junfeng Han, Na Lv, and Zhiqiang Feng

Short Papers and Technical Notes

Research on Resonant High-Voltage Plasma Power Supply 149
Zixin Hu, Song Yuan, Zhuoran Wang, and Min Zeng

Information for Authors 159

Author Index 161

Feature Articles

The Review of Spectrum Detection and Ultrasonic Vibration Control of Porosity Defects in Aluminum Alloy Welding

Jingyuan Xu and Shanben Chen

Abstract The porosity defect in aluminum alloy welding is one of the common internal defects in the welding process. The traditional detection method is time-consuming and complex, the equipment requirements are high, and the existing pores are difficult to repair. The arc spectral signal contains a large amount of welding process information. It can be used as a signal for judging the internal porosity defects. The ultrasonic-assisted welding can effectively clean up the internal pores in the molten pool. By combining the two methods, it can realize online detection and feedback control of porosity defects in aluminum alloy welding. In this paper, the research status of pore detection and control methods is reviewed. The development prospect of spectral detection technology and ultrasonic-assisted welding and the advantages compared with the traditional methods are analyzed.

Keywords Aluminum welding · Spectral detection · Ultrasonic-assisted welding

1 Introduction

As a typical light alloy, aluminum alloy is widely used in aerospace, automobile manufacturing and other fields due to its high corrosion resistance, excellent electrical and thermal conductivity, high mechanical properties and easy processing and forming [1]. In recent years, the research on intelligent welding technology has been developed, and the quality requirements for aluminum alloy welding have also been improved. This is mainly reflected in the fact that not only the appearance of the product is required to be perfect, but also the mechanical properties and internal defects of the welding need to be controlled. However, the aluminum alloy is prone to oxidize and adsorb the water in the air, which makes the welds easy to produce different defects. Among all the defects, the porosity defects are internal defects of the weld, which is more difficult to detect and control than other defects. Its existence

---

J. Xu · S. Chen (✉)
Intelligentized Robotic Welding Technology Laboratory, School of Materials Science and Engineering, Shanghai Jiao Tong University, Shanghai 200240, China
e-mail: sbchen@sjtu.edu.cn

© Springer Nature Singapore Pte Ltd. 2020

S. Chen et al. (eds.), *Transactions on Intelligent Welding Manufacturing*,
Transactions on Intelligent Welding Manufacturing,
https://doi.org/10.1007/978-981-15-7215-9_1

will not only lead to the reduction of the compactness of the aluminum weld line, but also reduce the effective working area and bearing area of the weldment, thereby causing stress concentration, greatly reducing the fatigue strength and toughness of the weld, and the dynamic load strength of the structure. When the problem gets more serious, it can cause cracks in the weld line. All the internal defects of welding, especially the detection of porosity defects, have been carried out offline after welding, using destructive testing or non-destructive testing methods, which seriously restricts the production efficiency of the welding process and is time-consuming and complex. And the existing porosity defects are difficult to be repaired. Therefore, the search for new porosity defect detection and inhabitation methods and the development of welding quality real-time detection technology are important for ensuring the consistency and reliability of welding product quality and achieving automation and intelligent welding process [2].

2 Forming Mechanism of Aluminum Welding Pore

Studies have shown that hydrogen is the main factor leading to the formation of porosity defects in the welding process of aluminum alloys [3, 4]. In the welding process, the solubility of oxygen, nitrogen and other gases in the molten pool is much lower than that of hydrogen, and it can escape quickly, so it is not the main cause of welding pores. The solubility of hydrogen in aluminum alloy is greatly affected by temperature (as shown in Fig. 1) [5], and hydrogen atoms will diffuse at a faster rate in the aluminum metal lattice at high temperature, when the base metal is melted. As the heat source leaves, the molten pool begins to cool and solidify from the boundary to the center of the weld. At this time, due to the steep drop of the solubility of

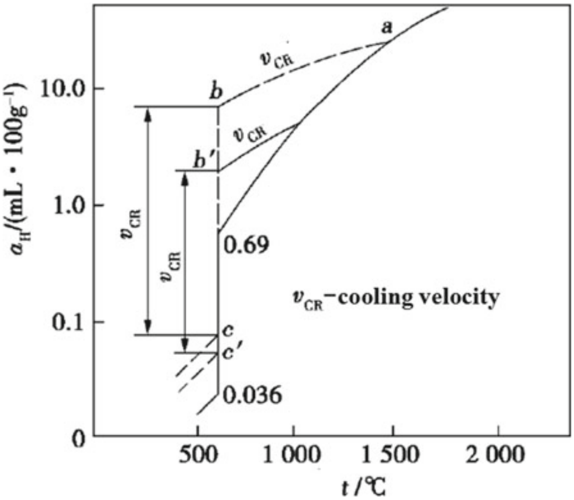

Fig. 1 Solubility of hydrogen in aluminum in different temperature [5]

the hydrogen in aluminum alloy at the freezing point, the difference can even reach dozen times, it will lead to precipitation during solidification. The hydrogen cannot be uniformly diffused into the molten pool, but is concentrated at a solid–liquid interface. The supersaturated hydrogen is easily heterogeneously nucleated in the molten pool by inclusions such as alumina and the surface of the semi-molten weld material.

Many scholars have put forward their own opinions on the growth and escape of bubbles during welding. Among them, Li [6] proposed in the book that in the process of bubble growth, if the internal pressure is greater than the sum of external pressures such as atmospheric pressure, metal static pressure and surface tension, that is, the growth power exceeds the resistance, and the bubble will continue to grow. Huang et al. [7] studied the mechanism of pore formation in titanium alloy laser welding process and proposed a bubble growth model controlled by hydrogen diffusion, and the phenomenon of bubble growth tends to increase according to electron beam migration. The bubbles can escape from the pores of the molten pool liquid film area. Guo et al. [8] used AZ31B and AZ61 thin plates as the research object and analyzed the pore morphology at different positions of the joints. The welds with excellent surface morphology were obtained by CO_2 laser welding, the joint samples were cut, and observed by Microscope, it revealed that the pores were dispersed, in which the pores at the bottom of the weld were relatively small, the pores at the weld line were large, and the shape of the pores mostly showed a relatively regular circle, and a few were oval. Huang [9] combined the classical solidification nucleation theory and established the growth model of the bubble in the TIG welding process of aluminum alloy. The quantitative analysis of the formation mechanism of hydrogen pores was carried out, and the related welding test and stomatal observation were carried out. It is concluded that the ratio of the growth rate of the bubble to the solidification rate of the molten pool directly determines the shape and size of the pore. Specifically, in order to increase the solidification rate of the molten pool, the bubbles after nucleation can be wrapped in the solid metal without being grown, so that it is insufficient to constitute a detectable pore defect; increasing the bubble growth rate and reducing the solidification rate allow the bubbles to fully grow out before being wrapped, without forming pores.

3 The Detection of Aluminum Welding Pore

Welding porosity defects can cause great damage to the toughness and performance of the weldment, so the detection of internal porosity defects is particularly important. At present, more common detection methods include X-ray detection, ultrasonic detection and spectral detection.

3.1 Traditional Detection Method

X-ray detection uses the law that the intensity of the X-ray weakens when it penetrates objects. According to the different X-ray absorption and scattering effects between weld metal and internal defects, it is judged whether or not defects are generated inside the weld [10]. Many scholars have done research on the extraction of porosity defects in X-ray images. Selvan et al. [11] used image processing techniques to obtain the size, shape and position of defects by acquiring the X-ray film of the weld, and using this information as the input of the feedforward neural network distinguishes the defects of the pores and the welds. Valavanis and Kosmopoulos [12] extracted 43 eigenvalues from the texture features of the weld X-ray image and the shape features of the interest region to characterize the six defects including pores and unfused; when using support vector machine (SVM) to classify and identify, the recognition of the pores is high, but the effect of incomplete fusion and crack is poor. Anand et al. [13] used morphological methods to distinguish defects in weld X-ray images, which can be used to classify defects based on their geometric features. Shi and Gang [14] used X-ray detection on the I-shaped complex structure from two different directions. They constructed the longitudinal and lateral position models of small pores in the weld and established a 3D model to visualize the spatial distribution of the small holes. However, X-ray detection method is a post-weld detection method, which takes a long time, high cost and complicated operation process. It is not sensitive enough for thick-walled workpieces. These shortcomings have hindered its practical application. Although some researchers have proposed a system for real-time acquisition and presentation of X-ray images [15] (as shown in Fig. 2), the ray source is expensive, and the limitations on human body damage restrict its application.

Ultrasonic detection method is much simpler than X-ray detection method. Hu [16–18] developed an ultrasonic detection system based on image locating and the signal of ultrasonic test under the weld test specimens containing cracks, slag inclusions, pores, unfused and non-penetration defects. The ultrasonic signal characteristics of defects and the multi-domain characteristics of defect shapes are used for classification and recognition. Based on the BP neural network, an intelligent recognition classifier is constructed for five types of actual welding defects. Compared with traditional methods, the recognition rate is improved. Yong et al. [19] used acoustic emission technology to perform non-destructive testing on the structural components of the orbital crane arm and effectively distinguished the two typical welding defects, such as porosity and infusibility, based on characteristic parameters such as amplitude and centroid frequency. However, acoustic detection technology still has the disadvantages of high equipment and high environmental requirements, and it is difficult to achieve real-time and continuous monitoring. Therefore, the spectral detection method has gradually received attention, and it is expected to become a new type porosity defects detection means by its real-time and information-rich features.

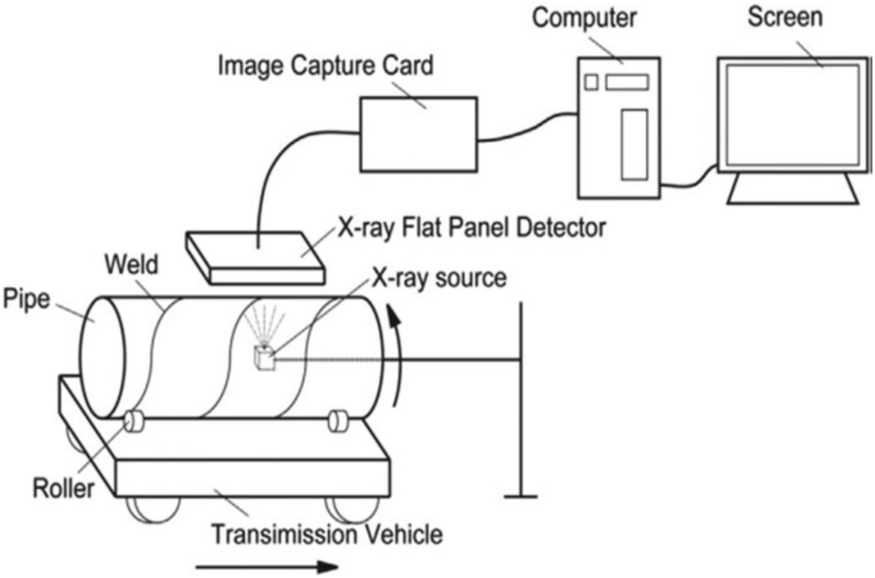

Fig. 2 Real-time X-ray image and automatic weld defect detection system [15]

3.2 Spectral Detection Method

The arc spectral information in the welding process has the advantages of rich information, signal sensitivity, high objectivity and essential relationship with internal defects of welding. In addition, it is not in direct contact with the arc. So it is expected to become a feasible method for real-time detection of weld defects [20, 21].

In the non-arcing state, the metal atoms in the base metal and the welding wire and the atoms in the shielding gas are in the lowest energy ground state. When excited by arc energy, the atom transforms from the ground state to the excited state. The excited state of the atom is in a very unstable state, so it will be the transition to a lower-energy level according to the selection rule, and the radiation emits energy to form an emission spectrum [22]. Among them, the spectral line contains metal elements, nitrogen, hydrogen, oxygen and other gas composition information and can also describe the arc temperature and the particle density of the arc column region from the side [23]. Based on this information, the prediction of defects in the welding process can be realized, and the purpose of real-time monitoring can be achieved.

Harooni et al. [24] performed a zero-gap lap laser welding test on magnesium alloys, using spectral plasma sensors to collect plasma information, and calculating the electron temperature, as shown in Fig. 3, to obtain the relationship between the pores and the spectral signals. It is indicated that the oxidation film can cause the generation of pores. Sibillano et al. [25] used a covariance mapping technique (CMT) to correlate electron temperature collected by spectral sensor with weld defects in real time and determine the presence of defects when the electron temperature exceeds

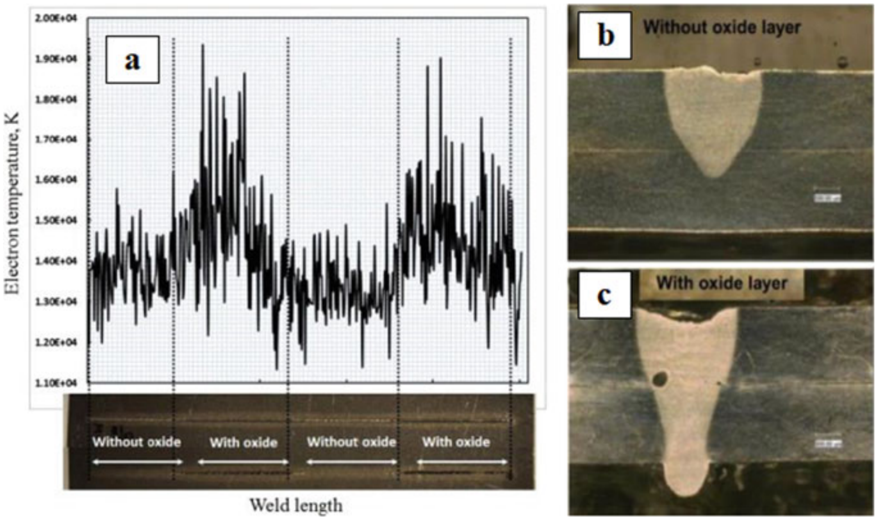

Fig. 3 **a** Laser plasma temperature curve. **b** Surface without oxide film weld cross section. **c** Surface with oxide film weld surface [24]

a set threshold. Although the arc spectrum contains a large amount of information, at the same time, there are many problems such as large number of dimensions, large-scale and complicated structure. These problems bring great difficulty to data mining. Therefore, how to efficiently and accurately mine the effective information we need from rich spectral data is also an important research direction. Yu Huanwei and others of Shanghai Jiao Tong University [26] used the PCA method to remove the redundant information in the arc data for dimensionality reduction. The first and second principal components of the analysis represent the Ar line and the metal line, respectively. The former can characterize the energy state of the arc changes, and the latter can characterize the stability of the weld pool. They also explore the relationship between these characteristic information and weld defects, as shown in Fig. 4. Zhang et al. [27] proposed a real-time non-destructive method

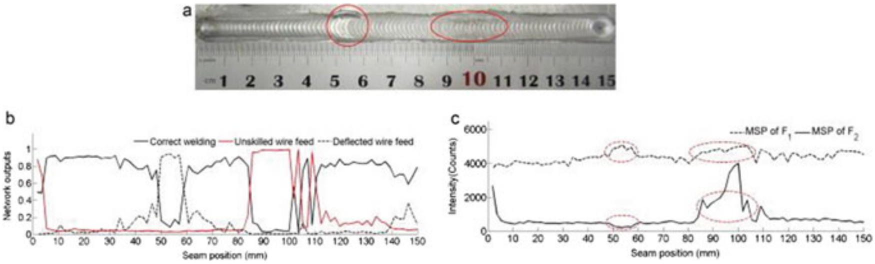

Fig. 4 **a** Defects caused by the wire. **b** BP neural network output. **c** MSP signal results of principal components F1 and F2 [26]

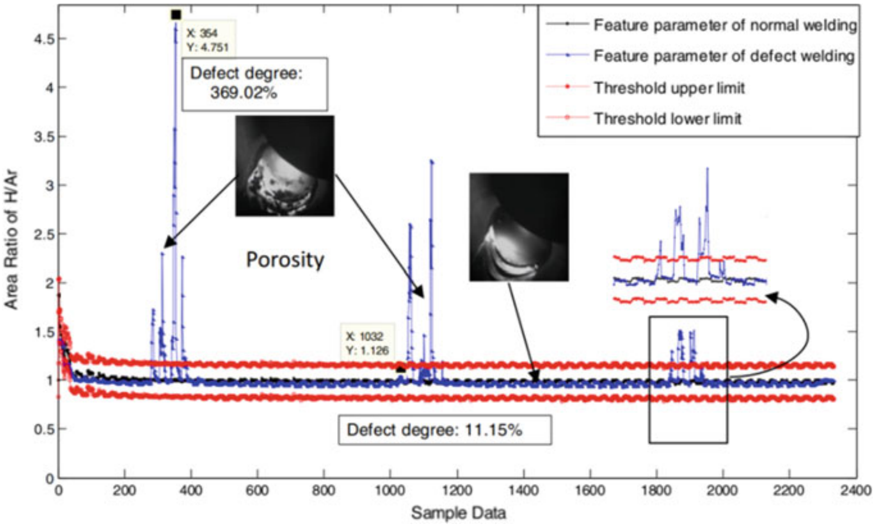

Fig. 5 Hydrogen argon line ratio and porosity defect diagram [27]

for detecting hydrogen holes in GTAW welding process based on plasma arc signal of welding arc. The hydrogen atom at 656.3 nm and the emission line of argon atom at 641.63 nm were analyzed. Multiple feature parameters are extracted and then detected by Fisher's distance criteria to select more sensitive features. It was found that the threshold detection method based on the features selected from the spectrum is feasible in detecting welding defects, and the results are shown in Fig. 5. Huang [28] used the EMD algorithm to perform adaptive decomposition to solve the non-stationarity and nonlinearity of the hydrogen/argon line intensity ratio signal and proved that the EMD reconstructed characteristic signal can be used for internal pore detection. Chen [29] used characteristic spectrum and continuous spectrum separation methods to process spectral information and used VMD algorithm to decompose signals according to different frequencies. Combined with machine learning methods to characterize stomatal defects, more accurate results were obtained.

4 The Inhabitation of the Porosity Defects in Aluminum Welding

4.1 *Research Status of Welding Porosity Inhabitation Measures*

Porosity defects have a great influence on the performance of the weld. Therefore, scholars have made many efforts and attempts to realize the reduction of the porosity defects in the welding process, which can be mainly divided into two aspects: pre-weld treatment and welding process improvement. In the pre-weld treatment, pre-treatment of the weldment can effectively reduce the defects in the welding process. Ryazantsev and Fedoseev [4] did pre-treatment on the surface of various types of aluminum alloy by chemical pickling and mechanical scraping, respectively. The results show that both methods can reduce the hydrogen content of the alloy surface and reduce the amount of bubbles during the welding process. In the Al–Li alloy welding test, Xiao et al. [30] found that the pore size and quantity in the weld seam were significantly reduced as the amount of oxide film removed from the base metal increased.

In the improvement of the welding process, Yan [31] found that increasing the current of MIG welding can increase the arc force and accelerate the flow rate of the molten pool in the fiber optic laser-MIG hybrid welding of 5-mm-thick high-strength aluminum alloy, thus facilitating melting. The escape of bubbles during solidification of the cell has a positive effect on the elimination of pores. Da Silva et al. [32] compared the propensity of P-GMAW and DP-GMAW (double-pulsed GMAW) to produce pores under different welding parameters. The results show that both methods have a certain inhibitory effect on the production of pores. Moreover, DP-GMAW does not cause an increase in the number of pores, at the same time, improving the welding efficiency, and can better meet the requirements of the industrial department for welding production efficiency and weldment quality.

Similar to the pulse current mechanism, the ultrasonic energy field also has an inhibitory effect on the generation of pore defects in the welding process. At the same time, it also has the effect of refining the microstructure of the weld microstructure, improving the mechanical properties of the joint and increasing the penetration depth. In recent years, it has been widely concerned by academic circles and has been applied to the welding of aluminum alloys, magnesium alloys, titanium alloys, stainless steels and dissimilar metals, as well as ceramic, glass and metal matrix composites, because of its advantages of easy regulation and control, improved welding performance [33]. For the effect of ultrasonic composite welding on the inhibition of porosity defects, Morisada [34] used high-frequency TIG to cross-weld A1050 aluminum alloy and studied the effect of different frequencies on the degassing effect. The results are shown in Fig. 6. Compared with 60 Hz, the number of pores at high frequencies is reduced. When the frequency is 15 kHz, the porosity in the weld is the lowest.

4.2 Porosity Defect Inhabitation Based on Ultrasonic Energy Field

The mechanism of action of the ultrasonic energy field includes increasing the heterogeneous nucleation rate and cavitation effect. Chen et al. [35] analyzed the results of ultrasonic application of 2195 Al–Li alloy and pure aluminum welding before arc extinction and found that the mechanism of ultrasonic refining the grain of Al–Li

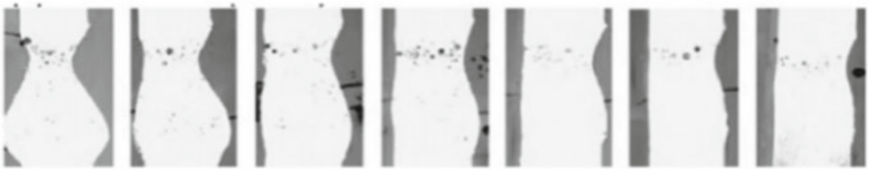

(a) TIG (60Hz)

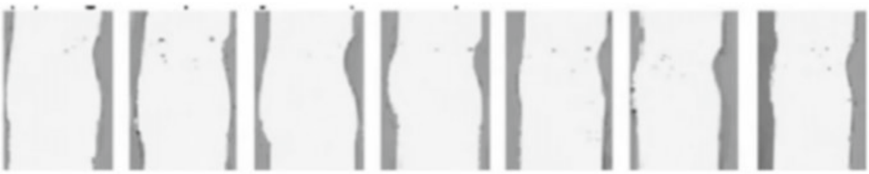

(b) U-TIG (15kHz)

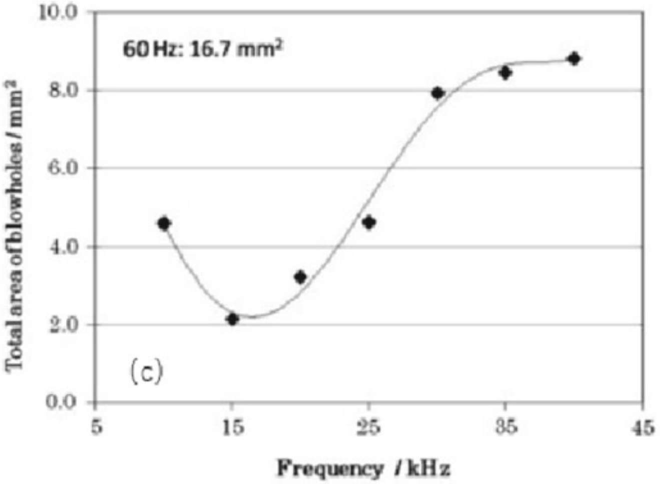

Fig. 6 **a** Porosity of arc welding seams (60 Hz). **b** Porosity of arc welding seams (15 kHz). **c** Relationship of total area of weld pores at different frequencies [34]

alloy welding is mainly to increase heterogeneous nucleation rate. In the welding process of pure aluminum, the heterogeneous nucleation rate in the molten pool is not significantly refined due to the small number of heterogeneous nucleation sites in the pure aluminum. On this basis, pure aluminum was used as the research object to eliminate the influence of heterogeneous nucleation, and ultrasonic was applied during the solidification stage. The result is shown in Fig. 7 [36], indicating that the ultrasonic has the effect of breaking the crystal grains in the solidification stage of the solution pool.

Cavitation effect of ultrasonic is the critical mechanism to control the porosity defects. It vibrates the tiny bubbles present in the liquid metal, and the sound field

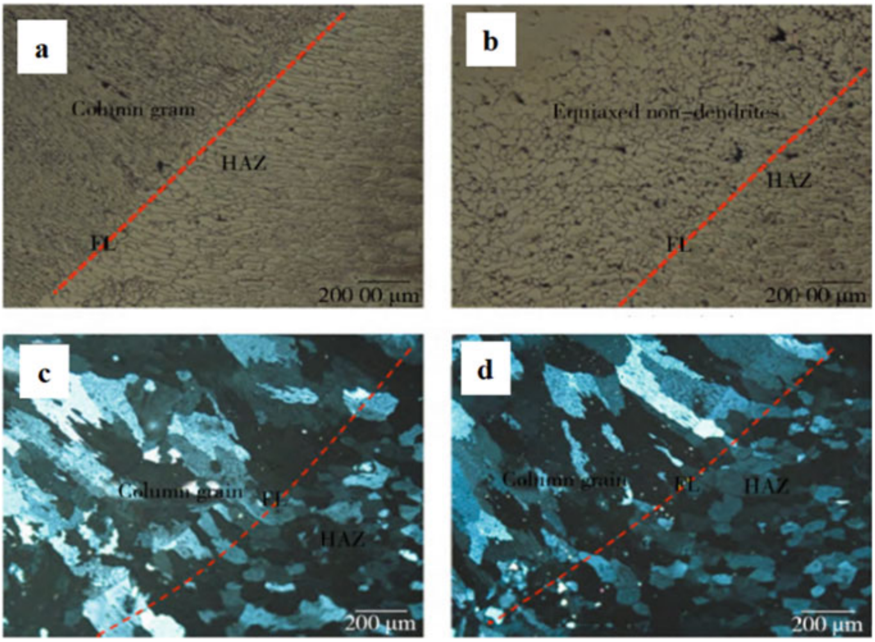

Fig. 7 Microstructure near the fusion zone of aluminum alloy and pure aluminum weld (**a** Al–Li alloy with no ultrasonic; **b** Al–Li alloy with ultrasonic; **c** Pure aluminum with no ultrasonic; **d** Pure aluminum with ultrasonic) [35, 36]

energy is accumulated. When the energy reaches a certain threshold, it will suddenly collapse, and it can clean up the bubbles while generating high temperature and high pressure and breaking the crystal branches. The process happens in a very short time, in a very small space, and produces a high temperature of more than 5000 K and a high pressure of 5×10^7 Pa, which provides a new and very special physical environment for the welding process. Some of the research on ultrasonic degassing in the casting field have been done so far, and the results suggest that the ultrasound could decrease the number of pores for the casting [37, 38]. Chen et al. [39] carried out the ultrasonic-assisted tungsten inert gas welding on a thin plate of 2195 Al–Li alloy, and the characteristics of the weld pores were analyzed in terms of their size and porosity. They put forward that ultrasonic cavitation can be divided into steady and transient cavitation. The transient cavitation can help break the bubbles in the molten pool, thus decreases the porosity of the weld, as shown in Fig. 8. They also found that the unreasonable transient cavitation, both too high and too low, will affect the degassing effect, as shown in Fig. 9.

For the ultrasonic-assisted arc welding technology, according to the different ways of adding the ultrasonic energy field, it can be divided into the following categories [40]: (1) Arc ultrasonic, that is, the ultrasonic signal is excited by the ultrasonic frequency current to generate the ultrasound, so that the ultrasonic effect is in the molten pool; (2) the ultrasonic and arc coaxially combined, that is, by

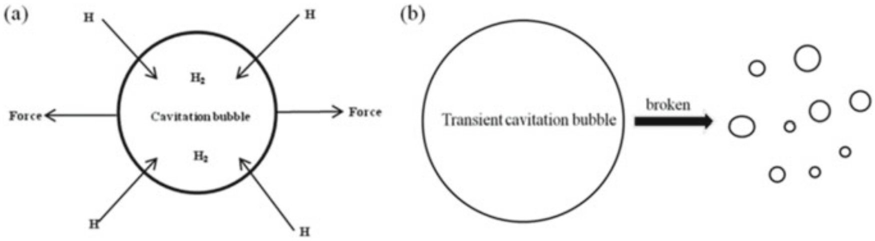
(a)
H
H
H_2
Force
Cavitation bubble
Force
H_2
H
H
(b)
Transient cavitation bubble
broken

Fig. 8 Effect of cavitation bubble on degassing by different routes: **a** Cavitation bubble expands, **b** Cavitation bubble collapses [39]

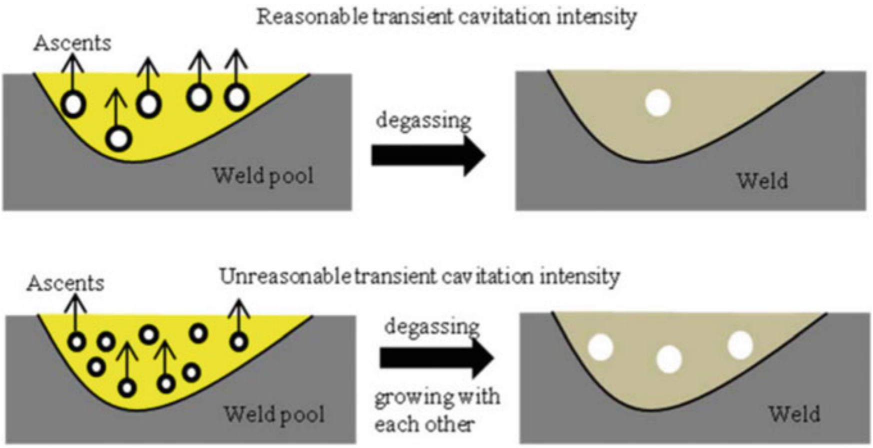
Reasonable transient cavitation intensity
Ascents
degassing
Weld pool
Weld
Unreasonable transient cavitation intensity
Ascents
degassing
growing with each other
Weld pool
Weld

Fig. 9 Effect of transient cavitation intensity on degassing in the weld pool [39]

installing an ultrasonic horn coaxially outside the welding torch, emitting ultrasonic waves to the molten pool and the arc through the emitting end; (3) ultrasonic acting on the welding wire, that is, ultrasonic transmission acts on the molten pool to improve the solidification process of the molten pool through the welding wire; (4) ultrasonic acting on the weldment or weld seam, that is, the ultrasonic tool directly passes the ultrasonic wave through the base metal into the molten pool, affecting the flow and solidification of the molten pool. Each method has its own advantages and disadvantages. Different techniques will be introduced below.

Arc ultrasonic technology is to modify the ultrasonic energy field by the circuit itself. In 1999, Wu Minsheng of Tsinghua University [41] proposed the arc ultrasonic technology for the first time. The high-frequency current was used to modulate the arc, and the arc was excited to generate ultrasonic waves. Wang et al. [42] proposed a double-tungsten argon arc welding method by arc ultrasonic excitation, as shown in Fig. 10. A common DC TIG arc is combined with an ultrasonic frequency arc acting on a molten pool. Ordinary DC TIG arc is used as the main heat source to melt the base metal, and the ultrasonic arc causes ultrasonic vibration in the molten

Fig. 10 Schematic of twin-arc system [42]

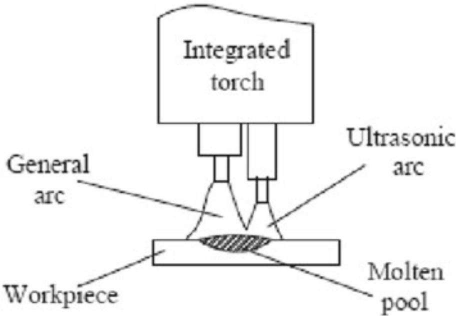

pool. Using this welding method to weld 304 stainless steel, the results show that, compared with the conventional TIG welding, the tensile properties of the joint after the double-tungsten argon arc welding of the arc ultrasonic excitation eutectic pool are significantly improved. The effect of exciting ultrasonic waves by high-frequency current also needs to consider the form of welding current. For both DC and AC TIG welding, scholars have done related research. Hua et al. [43] superimposed the high-frequency current in the DC TIG welding and successfully excited the ultrasonic energy field. The experimental results show that the grain of the nickel-filled metal FM-52M weld is successfully refined by this method, and the crack sensitivity was reduced. Wang et al. [44] conducted a study on the case of AC TIG welding and proposed a method of superimposing high-frequency pulses only at the base current. The experimental results show that the welding effect is improved after superimposed ultrasonic, and the effect of new method proposed is more pronounced for the plasma morphology, weld bath morphology and grain refinement, as shown in Fig. 11.

The ultrasonic and arc coaxially composite method mainly includes two parts: the welding system and the ultrasonic exciting system. The influence factors of the sound field excited by this method include the ultrasonic frequency and amplitude generated by the transducer, the height of the transmitting end, the shape and the diameter of the end face of the horn. Sun [45] successfully introduced ultrasonic into the GTAW and GMAW welding process by coaxially combining the ultrasonic transmitting end with the welding torch, as shown in Fig. 12. In GTAW or GMAW, the ultrasonic transmitting end emits ultrasonic waves, and the ultrasonic waves act on the arc and the droplets and then propagate to the inside of the molten pool to improve the welding effect. For the influence of the geometry and shape of the ultrasonic emission system, some scholars have conducted related research. Xie et al. [46] found through research that the use of small central through holes, large emission end face and appropriate curvature can effectively improve the acoustic effect. Compared with the rotating paraboloid and the rotating single-surface emitting end, the spherical acoustic emission end has a better effect on improving the acoustic radiation force. Wang [47] and others proposed the design form of the stepped ultrasonic radiation end and found through experiments that this method can greatly improve the sound field level of the welding area and improve the welding performance.

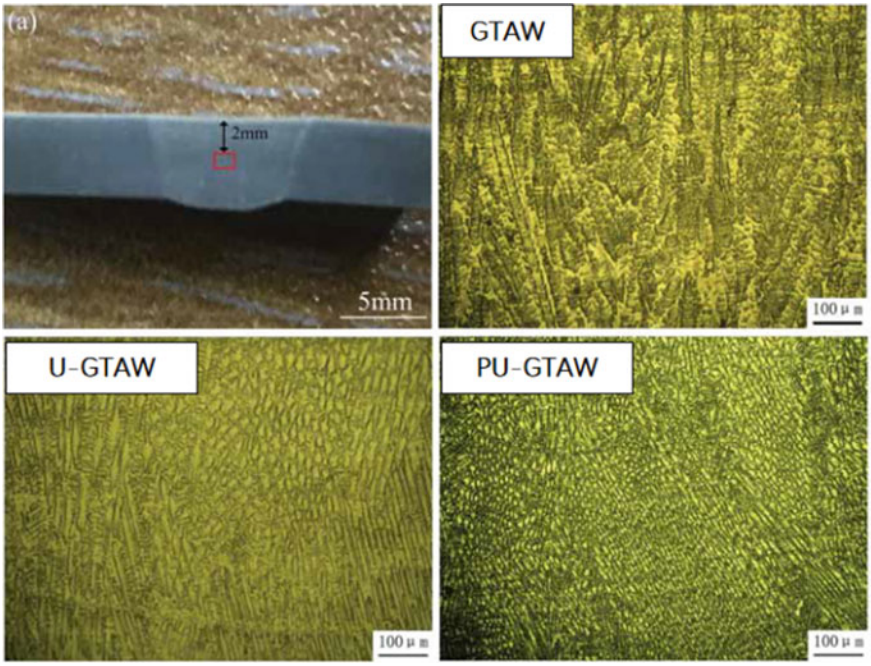
(a)
2mm
5mm
GTAW
100 μ m
U-GTAW
100 μ m
PU-GTAW
100 μ m

Fig. 11 Microstructure of welds under ordinary GTAW, ultrasonic GTAW and pulsed ultrasonic GTAW welding [44]

Fig. 12 Schematic of experimental equipment with a coaxial compound of ultrasonic and arc [45]

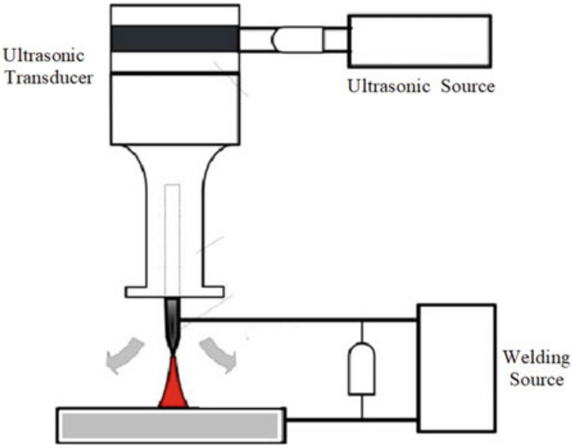
Ultrasonic Transducer
Ultrasonic Source
Welding Source

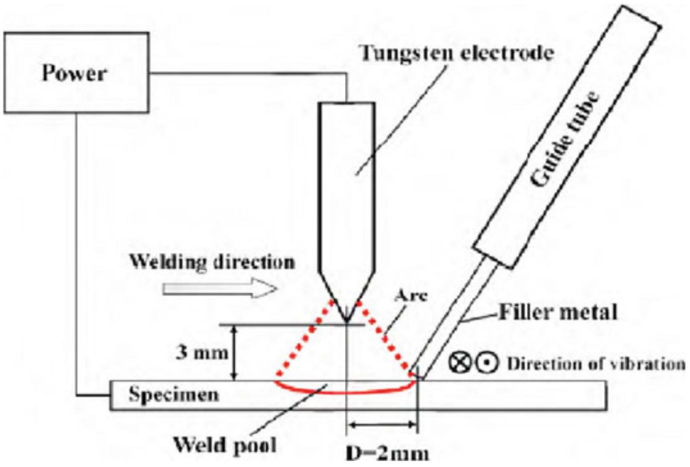

Fig. 13 Schematic of a welding apparatus with ultrasonic vibration induced by filler metal [48]

Ultrasonic adding by the wire is connecting the wire to the ultrasonic horn through the conduit. The wire is ultrasonically vibrated and introduced the vibration into the interior of the molten pool. Watanabe et al. [48] studied the effect of wire ultrasonic vibration on the solidification structure and mechanical properties of ferritic stainless steel weld metal. The schematic is shown in Fig. 13. It was found that this method can successfully transmit ultrasonic vibration to the weld pool. Ultrasonic vibration causes equiaxed grains to form in the central region of the weld metal. Under the condition of low welding speed, the grain in the weld is remarkably refined after ultrasonic application, and at the high welding speed, the grain refinement is not obvious after the application of ultrasonic.

Ultrasonic directly acts on the base metal, which is simpler in technology, easier to manufacture and less in interference between ultrasound and arc or wire. Dai [49] added the ultrasonic through the base metal into the molten pool in the 7075-T6 aluminum alloy GTAW welding process, and the results show that after the application of ultrasonic, the grain in weld zone and heat-affected zone is refined, while the weld hardness increases. Cui [50] introduced ultrasonic from the backside of the base metal during the welding of stainless steel manual welding electrodes. Studies have shown that after applying ultrasonic, the microstructure of the weld can be changed from columnar crystal to equiaxed crystal. In the GTAW welding of aluminum alloy, Chen [51] designed a new type of wheeled ultrasonic vibration tool head, which can roll on the weldment, as shown in Fig. 14, on the one hand, it reduces the damage to the horn and ultrasonic transducer during the movement, and on the other hand, this kind of the movable tool head can keep the relative distance between the ultrasonic vibration source and the welding pool constant during the welding process, avoiding the influence of the distance factor on the ultrasonic effect. The results show that the grain in the weld is refined, the second phase is finer, and the mechanical properties of the joint improve. Chen [52] has also done a lot of research on the mechanism of

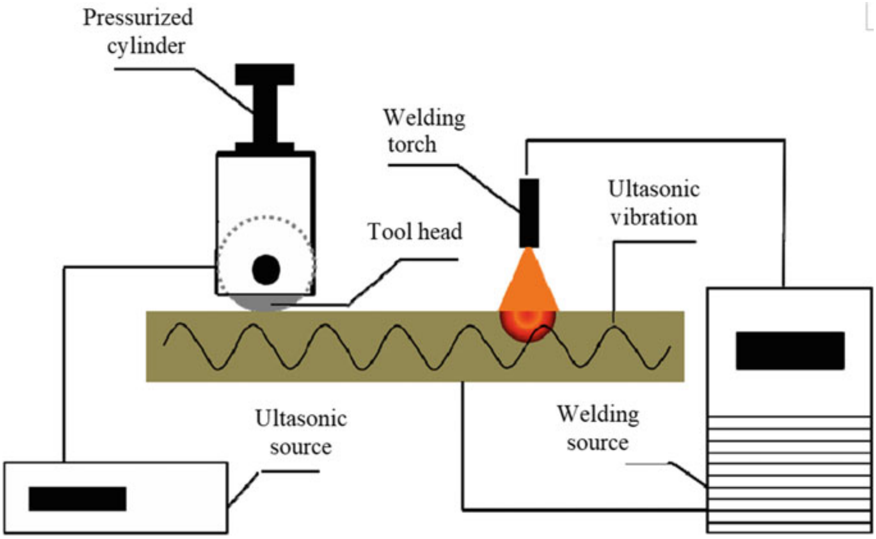

Fig. 14 Schematic of ultrasonic-assisted TIG welding system [51]

this method of ultrasonic energy field inhibiting stomatal defects. He first simulated the ultrasonic field distribution in the base metal and molten pool and established a finite element model of the sound field. Afterward, the formation, growth and floating behavior of bubbles in the molten pool were theoretically analyzed under the influence of ultrasound. By simulating the floating speed of bubbles under the influence of ultrasound, it is found that after applying ultrasound, the speed of bubbles floating in the molten pool is significantly accelerated under the effect of the sound pressure gradient force, and the results are shown in Figs. 15, 16 and 17.

In general, no matter which way the ultrasonic energy field is introduced in the welding process, as long as the parameters are properly selected, they will improve the properties of the weldment, especially have a good effect on the suppression of pore defects. However, each of the four ultrasound introduction methods has its own characteristics and advantages. The method of introducing ultrasound through the base metal and the welding wire is a direct contact type, and the method of introducing ultrasound through the welding torch and arc is a non-contact type, which requires the use of an air medium. Among them, the method of introducing ultrasound through the welding wire is relatively simple, but the effect will be affected by the welding speed and wire feeding speed, making its influencing factors more complicated and difficult to control; the introduction of ultrasound through the base material is also more intuitive, although the research has overcome the influence of the volume of the base material on its effect, but the frequency adjustment range of the power ultrasonic transducer is very narrow, making its adjustment not flexible enough; introducing ultrasound through the transformation of the welding torch does not need to spread through the solid medium, and an ultrasonic field is formed directly

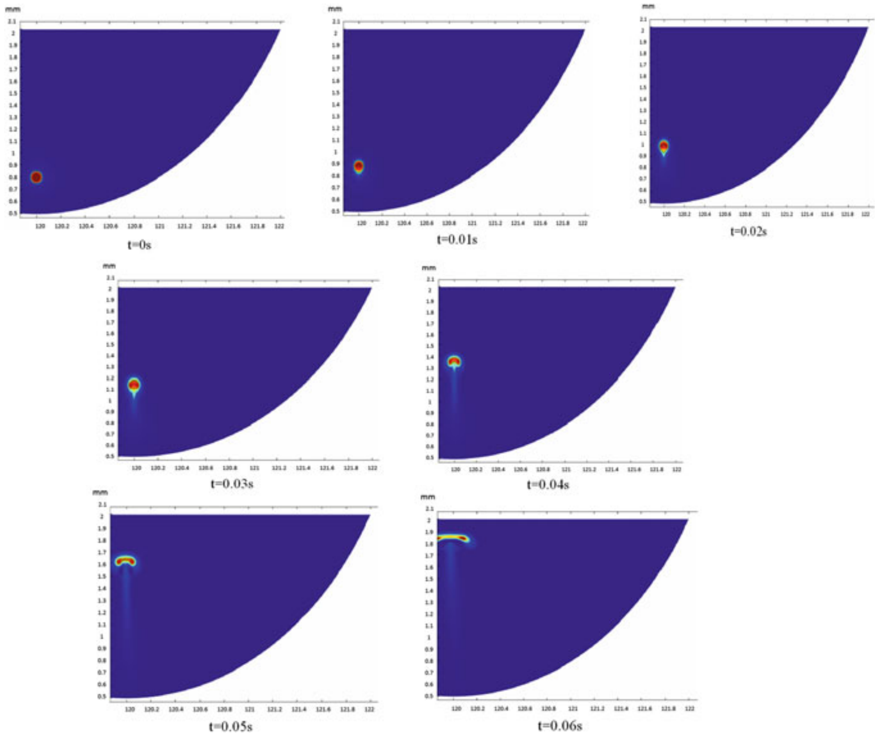

t=0s t=0.01s t=0.02s

t=0.03s t=0.04s

t=0.05s t=0.06s

Fig. 15 Bubble movement without ultrasonic [52]

above the molten pool to act on the solidification process of the molten pool. The disadvantage is that the transformation cost of the welding torch is higher, and there is also a defect that the relatively small adjustable range of frequency; the introduction of ultrasound through circuit transformation is to introduce the ultrasonic energy field into the welding process through the arc, in this method, the frequency and amplitude of the high-frequency electrical signal has a larger adjustable range, which will influence the ultrasonic energy field parameters and is more flexible than other methods, but in the high frequency, the matching of the electrical signal and the original welding circuit is more difficult, the heat dissipation and efficiency of the device are necessary problems, and the actual application is more difficult. Therefore, it is necessary to select the most suitable ultrasound introduction method according to different application scenarios.

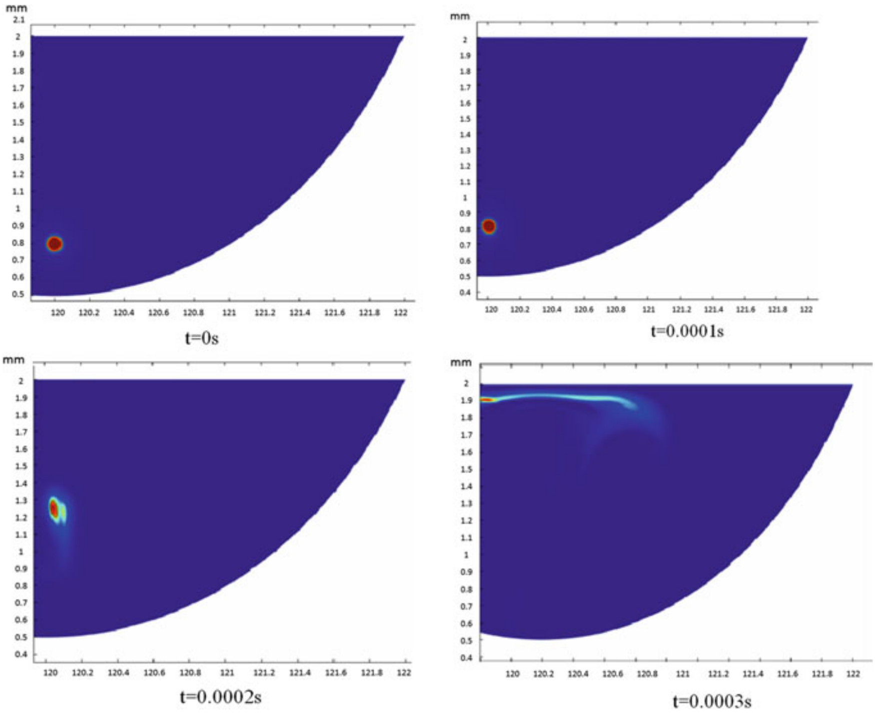

t=0s

t=0.0001s

t=0.0002s

t=0.0003s

Fig. 16 Bubble movement with ultrasonic [52]

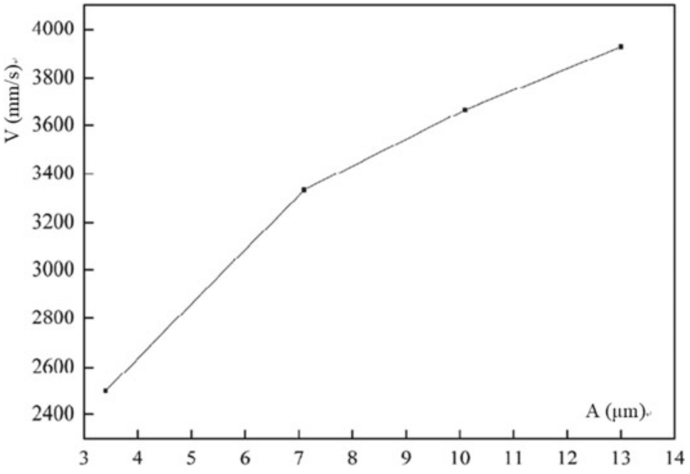

Fig. 17 Bubble movement velocity with different ultrasonic input amplitude [52]

5 Key Difficulties and Research Direction

In terms of spectrum detection, the redundancy and high dimensionality of spectral data are a necessary problem needing to solve. Hydrogen is closely related to the formation of pore defects in the welding process, but the content of hydrogen in the welding atmosphere is very low, the corresponding spectrum is very low and can be influenced by background spectrum. So how to extract effective information is the key step. It is important to explore a more effective method to deal with the spectrum data and a reliable algorithm to predict the pore defects by using multi-element spectral lines. The pore detection accuracy and the responding speed should be as high as possible.

In terms of the application of ultrasonic vibration, there are also some problems need to be considered. First is the way to produce the ultrasonic vibration in the welding area, and different methods have different advantages and disadvantages. It is not adequate to only consider the ultrasonic vibration effects of different methods. The cost, the compatibility with other devices and the effect must be considered at the same time. Secondly, the parameters should be researched more deeply. Although many advantages and effects of ultrasonic-assisted welding have been confirmed, there are few studies on the relationship between the defect control effect and the electrical or acoustic parameters in the literature. The matching research on welding and ultrasonic parameters is not deep enough, so the matching and combination problems between acoustic parameters and temperature field and stress field have not been solved. More regular conclusions need to be explored to realize feedback control.

The research direction on the intelligent control of aluminum alloy welding porosity defects can be divided into the following main parts:

Firstly, the welding experiment system needs to be set up. Considering multi-sensor systems and ultrasonic vibration systems, the structure that welding gun is fixed and the welding piece is moving is more suitable. By this structure, the sensors and the ultrasonic vibration equipment do not need to be fixed on the welding gun, and it can remove the disadvantage of adding ultrasonic directly on the base metal because of the constant position between ultrasonic equipment and welding pool. Both circuit modification and physical vibration adding ultrasonic methods can be studied on this system. The impact of vibration on the sensors can also be minimized.

Secondly, in the porosity defects detection, it is necessary to compare the existing algorithm through repeated experiments and analyze the accuracy rate of each method for the same spectral signal and the corresponding weldment pore defect position. The simplest and most reliable algorithm should be chosen to reduce the dimensionality of the data. The machine learning method, as a recent popular research area, can also be applied to the establishment of porosity defect prediction model.

Thirdly, the effect of different methods of adding ultrasonic vibration needs to be compared. For each method, the relationship between the defect control effect and the electrical or acoustic parameters needs to be explored. The electrical parameters include frequency and amplitude. When using ultrasonic transducer, the position

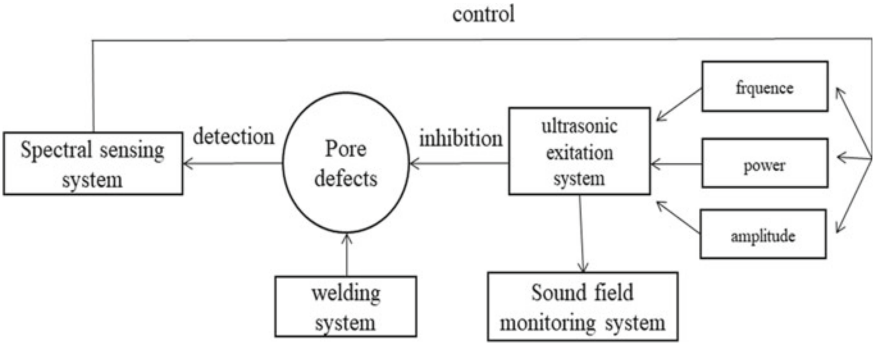

Fig. 18 Composition of porosity defects control system conclusion

and the power should be considered. The total area of pores in the weld and the penetration status are important measures of control effectiveness.

After the completion of the research work in the two aspects, it is necessary to combine the control theory with the control method of the pores to form a closed-loop feedback control. The response speed and accuracy of spectral detection are key issues. The specific idea is to collect the spectral signal of the welding process through the spectrograph, analyze whether there are porosity defect through the algorithm, then adjust the high-frequency pulse current parameter to the optimal value through the controller, thus control the porosity defect, and finally collect the signal through the spectral sensor. A closed-loop control system is formed to control the generation of porosity defects during the welding process, as shown in Fig. 18.

6 Conclusion

Spectrum detection can predict pore defects by information in welding process. Ultrasonic vibration can control the pore defects and improve the weld line performance. Combining the two methods with each other is expected to achieve intelligent control of welding quality. Compared to traditional post-weld inspection, it can greatly improve production efficiency.

Acknowledgements This work was supported by the National Natural Science Foundation of China, No. 51575349 and 61873164.

References

1. Chen SB, Lv N (2013) Research evolution on intelligentized robotic welding technologies. Dianhanji/Electr Weld Mach 43:28–36

2. Yu HW (2013) Research on dynamic process and defect features of aluminum alloy pulsed GTAW based on the welding arc spectral information. Dissertation, Shanghai Jiao Tong University
3. Liangxi T, Yun X, Zhigang L et al (2011) Porosity prevention in MIG welding aluminum and aluminum alloy. Weld Dig Mach Manuf 05:35–39
4. Ryazantsev V, Fedoseev V (2002) Metallurgical and technological porosity of aluminium alloys in arc welding. Weld Int 16:320–324
5. Zhou ZF (2005) Welding metallurgy: weldability of metal. China Machine Press, Beijing, pp 125–129
6. Li JY (2007) Welding metallurgy: weldability of material. China Machine Press, Beijing
7. Huang JL, Warnken N, Gebelin J-C et al (2012) On the mechanism of porosity formation during welding of titanium alloys. Acta Mater 60:3215–3225
8. Guo Y, Tong Y, Xiaona HE et al (2011) Effect of laser welding parameters on porosity rate in magnesium alloy. Hot Working Technol 03:173–174
9. Huang Y, Zhang Z, Lv N et al (2014) On the mechanism and detection of porosity during pulsed TIG welding of aluminum alloys. In: International conference on robotic welding, intelligence and automation, Springer, p 133–143
10. Wu S, Yu C, Zhang W et al (2015) Porosity induced fatigue damage of laser welded 7075-T6 joints investigated via synchrotron X-ray microtomography. Sci Technol Weld Joining 20:11–19
11. Selvan KA, Moorthy S, Rani BS (2013) Detection of weld defects in radiographic images based on region counting and classification using feed forward neural network with back propagation. Compos Mech Comput Appl Int J 04:279–289
12. Valavanis I, Kosmopoulos D (2010) Multiclass defect detection and classification in weld radiographic images using geometric and texture features. Expert Syst Appl 37:7606–7614
13. Anand R, Kumar P (2006) Flaw detection in radiographic weld images using morphological approach. NDT E Int 39:29–33
14. Shi D, Gang T (2013) Automatic extraction and visualization of spatial position data for bulk porosities in laser weldments with complex structures. NDT E Int 54:133–141
15. Zou Y, Du D, Chang B et al (2015) Automatic weld defect detection method based on Kalman filtering for real-time radiographic inspection of spiral pipe. NDT E Int 72:1–9
16. Hu W, Gang T (2013) Weld defect identification based on ultrasonic signal and image fusion. Trans China Weld Inst 34(4):53–56
17. Hu W (2012) Ultrasonic detection and identification of weld defects based on multi-range features and data fusion. Dissertation, Harbin Institute of Technology
18. Hu W, Gang T, Wang J (2011) Ultrasonic detection technology of weld defects based on video location. Trans China Weld Inst 32(9):49–52
19. Tao Y, Wang W, Sun B (2014) Nondestructive online detection of welding defects in track crane boom using acoustic emission technique. Adv Mech Eng 6:50–64
20. Sreedhar U, Krishnamurthy C, Balasubramaniam K et al (2012) Automatic defect identification using thermal image analysis for online weld quality monitoring. J Mater Process Technol 212:1557–1566
21. Węglowski M (2007) Investigation on the arc light spectrum in GTA welding. J Achievements Mater Manuf Eng 20:519–522
22. Kernahan J, Pang P-L (1975) Experimental transition probabilities of forbidden sulphur lines. Can J Phys 53:1114–1115
23. Li J, Song Y, Li H et al (2002) Basic theory and method of welding arc spectral information. Trans China Weld Inst 23(6):5–8
24. Harooni M, Carlson B, Kovacevic R (2014) Detection of defects in laser welding of AZ31B magnesium alloy in zero-gap lap joint configuration by a real-time spectroscopic analysis. Opt Lasers Eng 56:54–66
25. Sibillano T, Ancona A, Berardi V et al (2009) A real-time spectroscopic sensor for monitoring laser welding processes. Sensors 9:3376–3385

26. Yu H-W, Ye Z, Zhang Z-F et al (2013) Arc spectral characteristics extraction method in pulsed gas tungsten arc welding for Al-Mg alloy. J Shanghai Jiaotong University 47(11):1655–1660
27. Zhang Z, Kannatey-Asibu E, Chen S et al (2015) Online defect detection of Al alloy in arc welding based on feature extraction of arc spectroscopy signal. Int J Adv Manuf Technol 79:2067–2077
28. Huang YM (2017) Feature detection and compensation control of porosity during ac-GTAW of aluminum alloys based on arc spectral data. Dissertation, Shanghai Jiao Tong University
29. Chen HP (2019) Online detection of characteristics of porosity formation during ac GTAW based on arc spectrum. Dissertation, Shanghai Jiao Tong University
30. Xiao R, Zhang X, Yang W (2012) Progress in laser beam welding of Al-Li alloys. Laser Tera-Hertz Sci Technol 5:3
31. Yan J (2011) Study on technology, defects and joint quality by fiber laserarc hybrid welding high strength aluminum alloys. Dissertation, Huazhong University of Science & Technology
32. Da Silva CLM, Scotti A (2006) The influence of double pulse on porosity formation in aluminum GMAW. J Mater Process Technol 171:366–372
33. Jiuchun Y, Chunli Y, Huijie L (2015) Overview on ultrasonic-assisted welding and its scientific issues. J Mech Eng 51:41–49
34. Morisada Y, Fujii H, Inagaki F et al (2013) Development of high frequency tungsten inert gas welding method. Mater Des 44:12–16
35. Chen Q-H, Lin S-B, Yang C-L et al (2016) Effect of ultrasound on heterogeneous nucleation in TIG welding of Al–Li alloy. Acta Metallurgica Sinica (English Letters) 29:1081–1088
36. Chen Q, Lin S, Yang C et al (2017) Grain fragmentation in ultrasonic-assisted TIG weld of pure aluminum. Ultrason Sonochem 39:403–413
37. Abramov V, Abramov O, Bulgakov V et al (1998) Solidification of aluminium alloys under ultrasonic irradiation using water-cooled resonator. Mater Lett 37:27–34
38. Xu H, Han Q, Meek TT (2008) Effects of ultrasonic vibration on degassing of aluminum alloys. Mater Sci Eng A 473:96–104
39. Chen Q, Ge H, Yang C et al (2017) Study on pores in ultrasonic-assisted TIG weld of aluminum alloy. Metals 7:53
40. Fan CL, Chen QH, Lin SB et al (2018) Application of ultrasonic in arc welding. J Netshape Forming Eng 10(01):57–66
41. Wu MS, Duan XY, Li LM (1999) Study of arc-ultrasonic excitation and its characteristics. J Tsinghua University 39:110–112
42. Wang JJ, Hong XO (2011) Research on twin-arc TIG welding with ultrasonic excitation and its effect to weld. Key Eng Mater 974(450):300–303
43. Hua C, Lu H, Yu C et al (2017) Reduction of ductility-dip cracking susceptibility by ultrasonic-assisted GTAW. J Mater Process Technol 239:240–250
44. Wang J, Sun Q, Liu J et al (2017) Effect of pulsed ultrasonic on arc acoustic binding in pulsed ultrasonic wave-assisted pulsed gas tungsten arc welding. Sci Technol Weld Joining 22:465–471
45. Sun QJ (2010) Research on ultrasonic-arc behaviors and ultrasonic assisted TIG welding method. Dissertation, Harbin: Harbin Institute of Technology
46. Xie WF, Lin SB, Yang CL et al (2016) Effect of acoustic field parameters on arc acoustic binding during ultrasonic wave-assisted arc welding. Ultrason Sonochem 29:476–484
47. Wang J, Qingjie S, Junbo T et al (2018) Enhanced arc-acoustic interaction by stepped-plate radiator in ultrasonic wave-assisted GTAW. J Mater Process Technol 262:19–31
48. Watanabe T, Shiroki M, Yanagisawa A et al (2010) Improvement of mechanical properties of ferritic stainless steel weld metal by ultrasonic vibration. J Mater Process Technol 210:1646–1651
49. Dai WL (2002) Effects of high-intensity ultrasonic-wave emission on the weldability of aluminum alloy 7075-T6. Mater Lett 57:2447–2454
50. Cui Y, Xu C, Han Q (2007) Microstructure improvement in weld metal using ultrasonic vibrations. Adv Eng Mater 9:161–163

51. Chen QH, Lin SB, Yang CL et al (2016) Effect of ultrasonic impact during welding on microstructures and mechanical properties of TIG welded joint of 2A14 aluminum alloy. Chin J Nonferrous Metals 26(10):2071–2077
52. Chen QH (2018) Acoustic propagation characteristics and grain refinement mechanism of weld during ultrasonic assisted TIG welding of aluminum alloy. Dissertation, Harbin Institute of Technology

Research Papers

Microstructure and Mechanical Properties of TC4 Titanium Alloy by Electron Beam Freeform Fabrication

Wenjun Sun, Liming Ke, Shanlin Wang, and Wende Bu

Abstract Titanium alloy was known as the intelligent metal of the twenty-first century. Its comprehensive mechanical properties were widely used in the high-end equipment manufacturing industries, such as modern aerospace and national defense industries. Especially, more and more experts paid attention to the technology of additive manufacturing technology for titanium alloys at home and abroad. Electron beam freeform fabrication of TC4 titanium alloy is a new generation of high-efficiency, pollution-free, and low-cost rapid prototyping technology. In this paper, TC4 titanium alloy was investigated as the research materials, and it was particular to research on the uniformity of TC4 titanium alloy by electron beam freeform fabrication. The structure was manufactured with controlling the heat input to reveal the microstructural evolution and analyze its mechanical properties. At the same time, the heat treatment was utilized to control the microstructural uniformity for improving its comprehensive mechanical properties.

Keywords TC4 titanium alloy · Electron beam freeform fabrication · Microstructural uniformity · Comprehensive mechanical properties

1 Introduction

Additive manufacturing technology was an advanced forming technology developed in the late 1980s with the characteristics of rapid processing and high material utilization. It is especially suitable for the integrated forming of large and complex structures [1, 2] and widely used for equipment manufacturing in aerospace and national defense industry. Modern aerospace and defense industrial equipment manufacturing requirements are increasingly strict, lightweight, high precision and intelligent is the future

W. Sun · L. Ke (✉) · S. Wang (✉) · W. Bu
National Defence Key Disciplines Laboratory of Light Alloy Processing Science and Technology, Nanchang Hangkong University, Nanchang 330063, China
e-mail: liming_ke@nchu.edu.cn

S. Wang
e-mail: slwang70518@nchu.edu.cn

© Springer Nature Singapore Pte Ltd. 2020

S. Chen et al. (eds.), *Transactions on Intelligent Welding Manufacturing*,
Transactions on Intelligent Welding Manufacturing,
https://doi.org/10.1007/978-981-15-7215-9_2

development direction, while titanium alloys meet the needs of the overall upgrade of such equipment manufacturing. High-temperature titanium alloy and Structural titanium alloy were the main material for the development of the modern aerospace and national defense industry [3]. The additive manufacturing technology of titanium alloy is one of the main technologies to meet the requirements of the modern aerospace and defense industry to develop the overall lightweight structure. TC4 titanium alloy plays an important role in the titanium alloy additive manufacturing technology because of its excellent comprehensive mechanical properties [4]. In the field of additive manufacturing technology of titanium alloy, the laser technology [5–8] was often used, but the energy utilization rate of the laser additive manufacturing was relatively low and the forming speed was relatively slow, which hinders the development of the laser. Nevertheless, electron beam freeform fabrication technology [9–11] compared with laser forming technology has higher energy utilization rate, no reflection effect, and vacuum-free environment. While the deposited layers are well combined, it is suitable for processing and forming various shapes. It has shown more great advantages compared with high cost and long processing cycle technologies to manufacture large and complex structure of titanium alloy [12]. However, the deposited layers of TC4 titanium alloy were manufactured by electron beam freeform fabrication technology, and there was a serious heat accumulation in the deposited layers on account of the larger temperature gradient inside the molten pool and the difficulty of heat dissipation in vacuum environment resulting to generate coarse columnar crystals grown along the epitaxial grain boundary. At the same time, the special thermal cycle history in the deposited layers gave rise to the inhomogeneous distribution of α phase in the crystals [13–15]. The existence of these adverse factors made the mechanical properties of the deposited layers decreased, and there was obvious anisotropy, which seriously restricts the application of the structural deposition in practice. In this paper, the microstructural evolution and mechanical properties of deposited layers were researched to provide a reference for the engineering application about additive manufacturing of titanium alloy.

2 Materials and Methods

TC4 titanium alloy wires with a diameter of 0.8 mm were used in the test as the feeding material, and the annealed TC4 plate was used as the base material. The base material size was 200 mm × 100 mm × 15 mm. The KS15-PN150KM vacuum electron beam welding equipment made in Germany was used to manufacture the deposited test with the wire feeding system. Before manufacturing the deposition, the surface of the base material needed to clean up stains. After the cleaning was completed, the base material was placed to be clamped in the vacuum chamber, and then the wire feeding position must be adjusted well so that the wires were fed into the molten pool perpendicularly to the deposition direction (X direction). when the vacuum was drawn below 7×10^{-4} Pa, the test could be started. The position and angle of the nozzle were unchanged, only the substrate moves with the

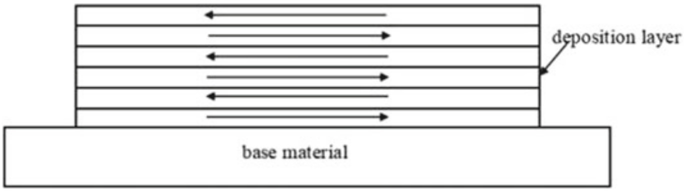

Fig. 1 Electron beam freeform fabrication deposition pattern schematic diagram

worktable. During the deposited process, the accelerating voltage was kept at 60 kV. The focusing current needed to be adjusted to target the focus to the surface of the base material with directly placing the feed nozzle below the focus. Using the heat input of 210 J/mm, 10 layers are continuously deposited in one direction on the base material, then the deposited process must be suspended for 20 min to fully cool the 10 layers so that the repeated heat cycle effect of the deposited layers was reduced to room temperature. At the same time, in order to reduce the heat accumulation in the initial section and fill up the arc-shaped collapse of the end section, the initial section and the end section were interchanged after the cooling was finished when every 10 layers were deposited. The above steps need to repeat to complete the deposition process. The specific deposition method is shown in Fig. 1.

The heat treatment of the deposited samples is carried out by using GSL1600X vacuum tube-type high-temperature heat treatment furnace. The heat treatment process of 960 °C, 2 h/AC + 550 °C, 4 h/AC was established to investigate the effect of heat treatment on the uniformity of electron beam freeform fabrication.

The metallographic specimen perpendicular to the deposition direction (YOZ cross section) was acquired. After grinding and polishing the specimen, it was corroded by the corrodent prepared with nitric acid, hydrofluoric acid, and water in 2:1:7 proportion. The microstructure of the specimen was observed by 4XBTV inverted optical microscope (OM) and FEI NOVA NANOSEM 450 scanning electron microscope (SEM).

The microhardness of the deposited layers along the deposition height direction (Y-direction) was measured using a WT-401MVD dimensional microhardness tester. From the top of deposited layers to the base material, the interval between each two points is 0.2 mm, the load is 200 g, and the pressing time is 10 s. The hardness values of the three rows were measured parallel to the height direction of the deposited layers, and the adjacent two rows were separated by 0.25 mm.

The position intercepted on the deposited layers and the size of specimen are shown in Fig. 2. The tensile specimens were non-standard. Tensile specimens are acquired parallel to the deposition direction (X-direction) and parallel to the deposition height direction (Z-direction) to test the anisotropy of the mechanical properties. In the X-direction, the upper, middle, and lower parts were sampled along the height of the deposited layers to test the mechanical properties by WDW-50 universal tensile testing machine. The tensile rate was 1 mm/min. Each group has three tensile specimens, and the average value was the tensile properties of the group. After tensile

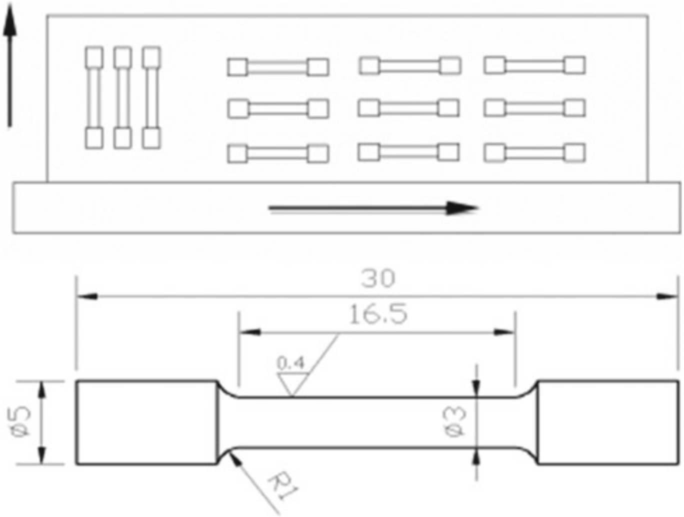

Fig. 2 Diagram of tensile specimen intercepted position and size

tests were completed, the fractures were analyzed by FEI NOVA NANOSEM 450 scanning electron microscopy (SEM).

3 Results and Discussions

3.1 Macroscopic Morphology of the Deposited Layers by Electron Beam Freeform Fabrication

Figure 3 is a macromorphology and cross section of the deposited layers obtained by electron beam freeform fabrication with the method in which Fig. 1 shows. It can be seen from the figure that there are distinct stratifications between the deposited layers, no defects such as unmelted between the layers, and the interlayer welding is good. Since the test is suspended once each 10 layers, the boundary between each 10 layers is very obvious, and the layer stacking characteristics are clear. Because the initial section and the ending section are interchanged after each 10 layers deposited, the protrusions in the initial section fill up the collapse of the end section, so the difference between the height of the initial section and the end section on the whole deposition layer is small, the uppermost surface of the deposited layers which have not obvious fish scales is flat and smooth. The 60 layers obtained in this experiment are divided into four zones: The bottom part of the deposited layers: The heat-affected zone (A zone); the middle part of the deposited layers: the gradient-organized zone (B zone) in the 40-layer zone from the base material to the 40th deposited layer; the

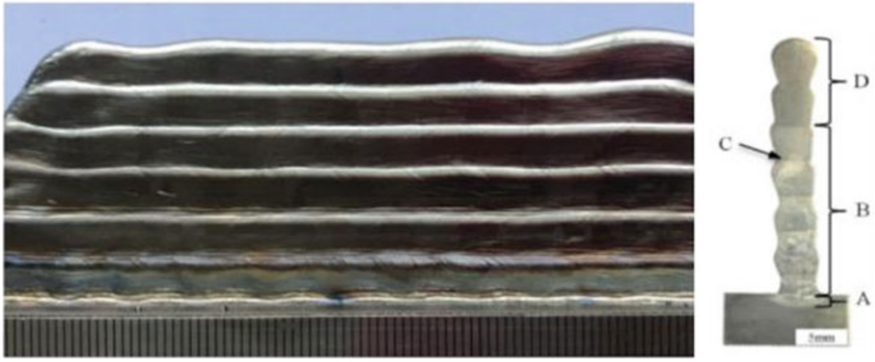

Fig. 3 Macromorphology and cross section of the deposited layers

deposited stratification zone (C zone); the upper deposited layer: uniform zone (D zone) in the range of 40–60 layers. It can be seen from Fig. 3 that The A zone is small due to the small heat input amount; In the B zone, there is a clear strip line of the light and dark stripes that is the C zone on the pause interface after continuous deposition process; It can be seen from the D zone that although the cooling is suspended after deposition, the light and dark strips at the pause interface disappear, and the overall area is almost uniform, with no other obvious macroscopic features.

3.2 *Microstructure Morphology of the Deposited Layers*

Figure 4 is a microstructure of the deposited layers along the height. When the heat input is 210 J/mm, it can be seen from Fig. 4a that at the bottom of the deposited layers, there are obvious grain boundaries, and α phase grows along the grain boundary. The α phase precipitated at the boundary of the original β grain is called the grain boundary α phase, collectively, all of them are called αGB. There are two distinct α phases in the grains, one is a lath-shaped α phase growing inside the grains, which are interlaced in the original β grains to form a basket weave structure, and

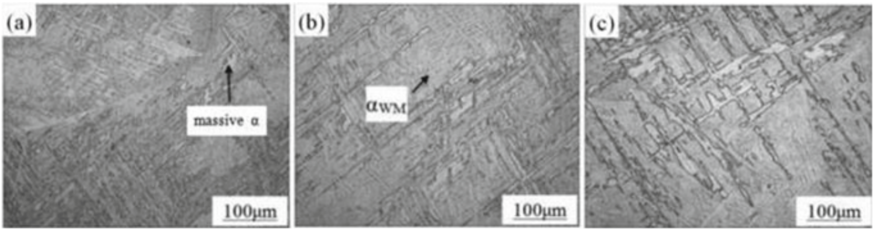

Fig. 4 Deposited layer structure **a** bottom, **b** middle, **c** top

it is denoted as α_{wm}; the other starts to nucleate at the grain boundary and grows parallelly to the interior of the original β grain, and it is denoted as α_{Gwm}. The α phase inside the original β grains is mainly distributed in the form of α_{wm}, and a small amount of fine α_{Gwm} is distributed at the grain boundary, and some lath-shaped α phases are coarsened or fused to each other to forming a few bulk α phase. There is a certain number of lamellar α' phases which have a significant directional dependence with the original β grains. According to the Burgers orientation relationship [16] $\{0001\}\alpha \| \{110\}\beta$, $<1120>\alpha \| <111>\beta$, it has 12 phase variants produced during the $\beta \rightarrow \alpha$ transition occurs, so the lamellar α' in different grains always constitute a certain angle with each other. It can be found from Fig. 4b that the structure is mainly composed of a dark region and a light region in which the dark region is a cross-lamellar α' phase and the light region is α_{wm} that the lath-shaped α phase is woven with each other and contains a amount of bulk α phase in the middle of the deposited layers. From Fig. 4c, it shows that a number of lath-shaped α phase broken grow up to form bulk α phase in which the number and size are both significantly increased in the upper deposited layers.

According to the analysis, the main reason for the different α phase morphology of the height direction is that the thermal cycling history in the bottom, middle, and upper regions of the deposited layers is different. With the height of the deposited layers rising, the number of the bulk α phase increases, and the thickness and length of the lamellar α' phase also increase. The lower temperature of the molten pool and the smaller temperature gradient are favorable for the formation of α_{wm}. As the heat input increases, the temperature of the molten pool can increase and α_{wm} fuses to form a bulk phase. When the heat input is further accumulated, the temperature of the molten pool is high and the temperature gradient is large relatively, the cooling rate in the molten pool become faster, and the temperature is rapidly reduced from the high-temperature β phase region to the two-phase region, so that the high-temperature β phase occurs in which the transformation of $\beta \rightarrow \alpha + \alpha' + \beta$, the bulk α phase and the lath-shaped α phase will transform into a lamellar α' phase, causing lath-shaped α phases, a bulk α phases, a lamellar α' phases and β phases to coexist in the deposited layers.

Figure 5 is a SEM image of the α phase in different regions of the deposited layers with a heat input of 210 J/mm. It can be seen from the figure that the α phase is a

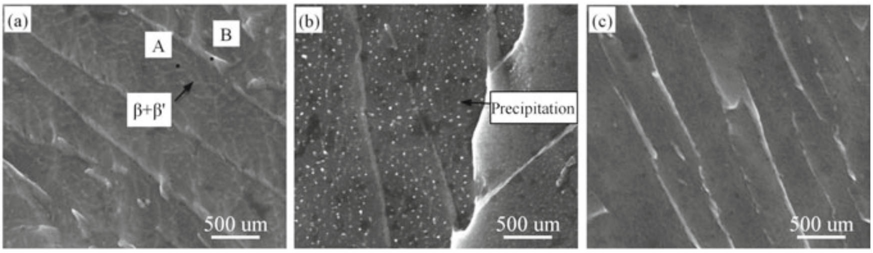

Fig. 5 Deposition layer structure **a** bottom, **b** middle, **c** top

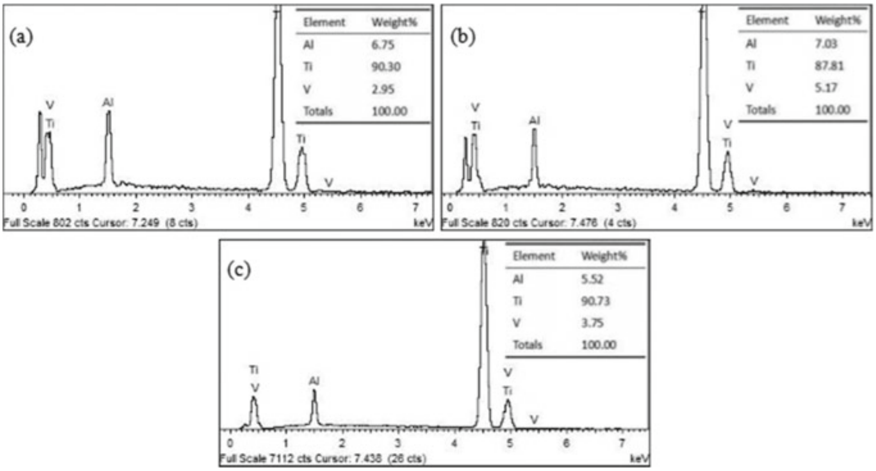

(a)

Element	Weight%
Al	6.75
Ti	90.30
V	2.95
Totals	100.00

(b)

Element	Weight%
Al	7.03
Ti	87.81
V	5.17
Totals	100.00

(c)

Element	Weight%
Al	5.52
Ti	90.73
V	3.75
Totals	100.00

Fig. 6 Analysis of alloying elements in the marking area. **a** Content of alloying elements at point A. **b** Content of alloying elements at point B. **c** Content of alloying elements in entire region of Fig. 5a

lath-shaped phase having a width of 250–500 nm and has no significant difference in morphology. In the α phase at the bottom of the deposited layers, as shown in Fig. 5a, it can be found that the crisscross lath-shaped phases are distributed on the α phase matrix in the β-transformed structure, and the EDS point scan result is obtained at the lath-shaped A as shown in Fig. 6a, the EDS point scan on B at the surrounding of β phase is shown in Fig. 6b. After comparison, it shows that the number of stable element V in β phase at A is significantly lower than that at B. This is due to the separation reaction of β phase, $\beta \rightarrow \beta + \beta'$, β' phase is a metastable phase of solute depletion, which is coherent with β phase [17]. Because of the segregation of the stable elements in β phase, such as V, beta-stable elements enriched to stabilize β phase become beta-labile elements, thus β phases form β' phases restrict with β phase each other and the morphology is constituted of them in Fig. 5a. The EDS scan results for the entire Fig. 5a are shown in Fig. 6c. It can be seen that the V element content percentage is 3.75%, which is similar to the content of 4% in related grades with only a small decrease, indicating that elemental diffusion is limited to local microregion, while the total content remains substantially constant on the whole. In the middle of the deposited layers, as shown in Fig. 5b, no separation reaction of the β phase was observed, but a fine dispersed phase is found to be uniformly precipitated on the α matrix in the α phase. These fine precipitated particles are compounds of V and V [18, 19]. Due to the rapid cooling rate of the deposition process, the V element is not sufficiently diffused but remains in the solid solution, V is a beta-stable element in which its solubility in the α phase is not large, so that the V element is supersaturated in the matrix to form a supersaturated solid solution. During the subsequent deposition process, the bottom and middle part of the deposited layers are reheated to a sufficiently high temperature due to the heat input accumulated in the upper is transferred down. The particles contain V are precipitated from the supersaturated matrix in a very fine and uniformly distributed form. Although the bottom of the deposited layers is also heated to a sufficiently high temperature, cooling rate in the bottom of the deposited layers is faster than the middle, so that the particles have no time to precipitate out and then cooled, eventually causing only the middle of the deposited layers to have dispersed second phases. However, the V element is still dissolved in the matrix. At the upper of the deposited layers, as shown in Fig. 5c, the separation reaction of the β phase and the precipitation of the dispersed phase are not observed in the α phase, indicating that the segregation of beta-stable elements is decreased at this time, therefore β-transition tissue is uniformly distributed.

Figure 7 shows the XRD scan results of the deposited layers with a heat input of 210 J/mm. It can be seen from the figure that almost all of the diffraction peaks of the α phase are in the deposited layers. Comparing with the diffraction peaks between the middle and upper part of the deposited layers, the two strong peaks in the middle of the deposited layers are significantly weakened in the upper part of the deposited layers. However, the intensity of other weaker diffraction peaks increased, indicating that the α phases in the middle of the deposited layers show a distinct orientation distribution, but the α phase texture in the upper part of the deposited layers is weakened and the orientation becomes disordered. At the same time, it can be found from the figure that some fragile precipitates AlV_3 and Al_3Ti are formed in the deposited layers. The intensity of the diffraction peak is lower in the middle of the deposited layers, but the intensity of the diffraction peak in the upper part of the deposited layers slightly increases.

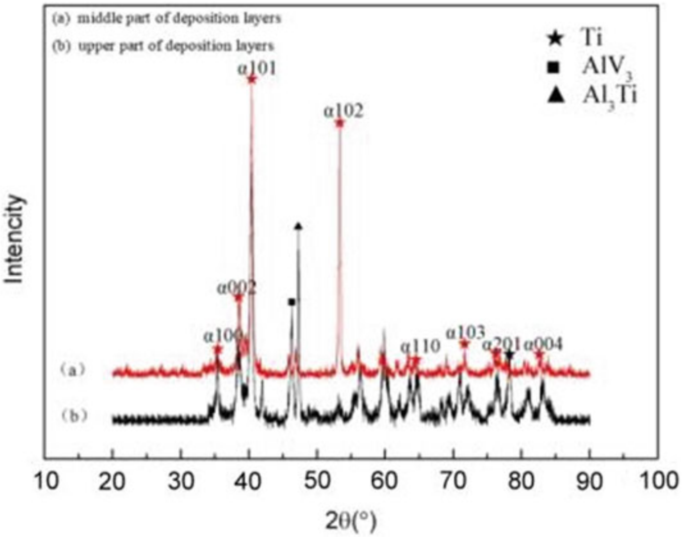

Fig. 7 XRD scan results of the middle and upper parts

3.3 Microstructure of Electron Beam Freeform Fabrication after Solution Aging

Figure 8 shows the microstructure of a single 60-layer deposition layer after solution aging. The macroscopic structure is similar to that of the uniform microstructural region before heat treatment, and the obvious dark and light stripes existed in the interlayer suspensions completely disappear. The microstructure of the deposited layers is almost homogeneous organization along the height, which all of them are lath-shaped α phases with similar aspect ratio. There is no obvious regional and gradient microstructure. This is obviously different from the microstructure of the deposited layers before heat treatment. The results show that the overall uniformity of the microstructure of TC4 titanium alloy by electron beam freeform fabrication is significantly improved after the heat treatment at 960 °C, 2 h/AC + 550 °C, 4 h/AC.

Figure 9 is a SEM comparison of the deposited layers between before and after heat treatment. From the figure, the results show that the SEM images of the microstructure of the deposited layers before and after the heat treatment are basically the same, all of which are small strip-like α phase. Before the heat treatment, the inner wall of the lath-shaped α phases in the middle and the upper of the deposited layers is smooth and flat, and the inner wall of the lath-shaped α phases in the bottom has obvious “mesh gully.” After the heat treatment, there are obvious precipitated particles in the lath-shaped α phases of the entire deposited layers, indicating that the precipitated particles in different positions of the deposited layers after heat treatment are compounds of V and V. The precipitated phase in the bottom part of

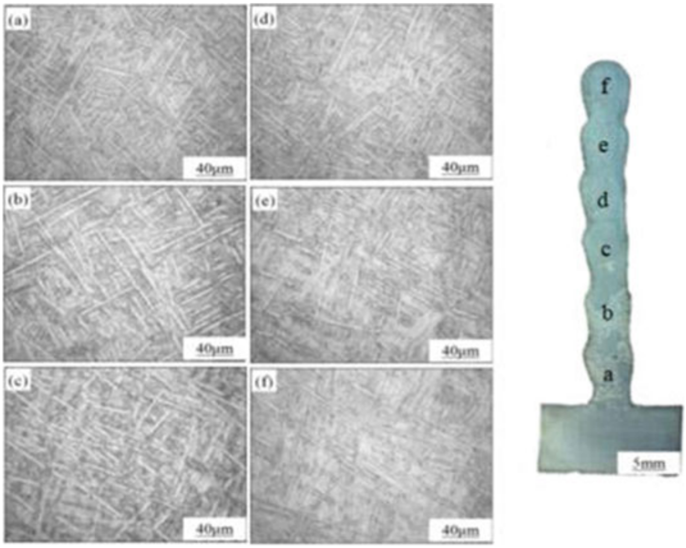

Fig. 8 Microstructure of the deposited layers after solution aging

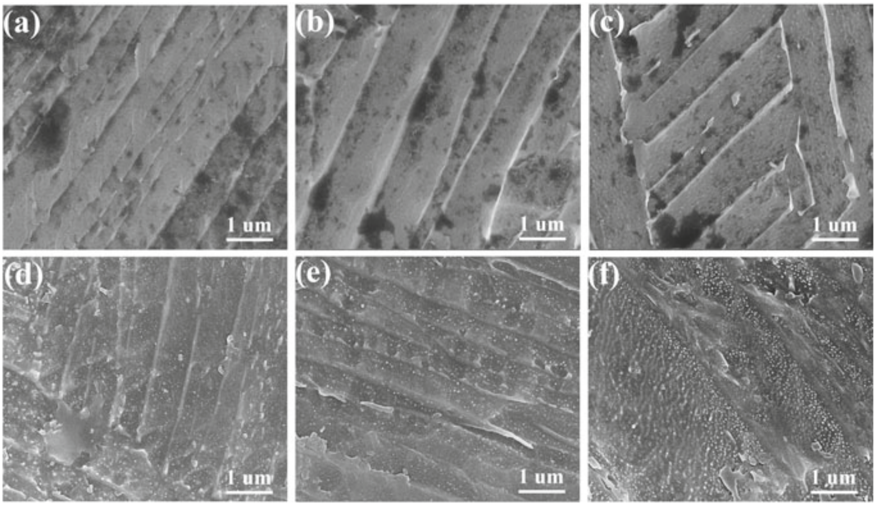

Fig. 9 SEM pictures of different positions in deposition layer. Before solution aging: **a** top, **b** middle, **c** bottom. After solution aging: **d** top, **e** middle, **f** bottom

the deposited layers is the densest and the size is larger than that of the precipitated phase in other positions. In the middle of the deposited layers, the density and size of the precipitated particles slightly decrease. In the upper part of the deposited layers, the density and size of the precipitated phases were further reduced, and only a small amount of precipitated phases is scattered in the lath-shaped α phase, because the deposited layers are cooled in the high-temperature zone to form a large number of metastable phases after solution aging for a long time, and then the aging of the metastable phase in the medium-temperature region for a long time results in the aging decomposition of the metastable phases which can precipitate a large number of fine dispersed second-phase particles. These disperse phases can produce a dispersion strengthening effect on the deposited layers, increasing the mechanical properties.

3.4 *Microstructural Evolution of Deposition Layer Before and After Solution Aging*

According to the above research on the microstructure of the deposited layers before and after the heat treatment, the microstructural evolution diagram shown in Fig. 10 is obtained. It can be concluded from the figure that before the heat treatment, when depositing to the Nth layer, the uppermost layer is crystallized directly from the molten state. In the state of cooling solidification crystallization, the cooling rate is so extremely fast that the β phases have no time to diffuse and cannot transform into

Fig. 10 Diagram of microstructural evolution in the deposited layers

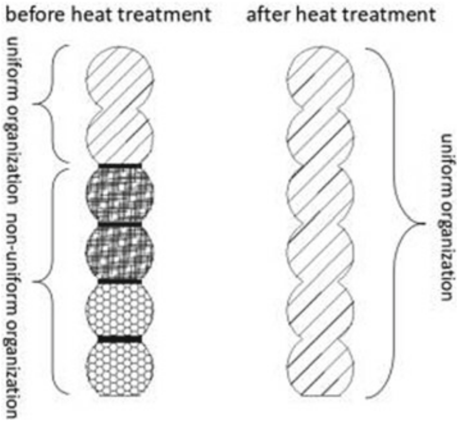

the α phase while the supersaturated non-equilibrium hexagonal lattice α' phase is formed in a shear manner, resulting in a large number of α' phases at the top of the deposited layers. When deposited to the $n + 1$th layer, the electron beams re-melted a portion at the nth layer while reheating the other unmelted portions above the beta transition temperature. During the subsequent rapid cooling process, most of the β phases re-shear to transform into the α' phase in the molten region and the rest of the deposited layers reheated to the single-phase region is mostly transformed from a high-temperature β phase into a basket weave structure interlaced with lath-shaped α phases. When deposited to the $n + 2$th layer, a portion of the $n + 1$th layer is re-melted similar to the previous one and the remaining portion is reheated to a single-phase region, and a larger range of basket weave region is formed than that in $n + 1$th layer after cooling. When the $n + 3$th layer is deposited, the electron beam is not enough to reheat all the deposited layers above the transition temperature, so the part above the transition temperature is cooled to form lamellar α' phases and basket weave structure, while the lath-shaped α phases are coarsened to form a stratification line in the region where the single-phase region and the two-phase region intersect. In the region below the stratification line, the higher the temperature is, the closer it is to the stratification line along the height direction of the deposited layers. Due to the large-scale crossing of the two-phase region, the temperature of the deposition layer changes gradient in the height direction and the thermal effect of the lath-shaped α phase also shows gradient change, resulting in the formation of gradient structure below the top stratification line [20]. After solution aging, the microstructure become uniform which are all the lath-shaped α phase and the stratification lines disappear in the deposited layers.

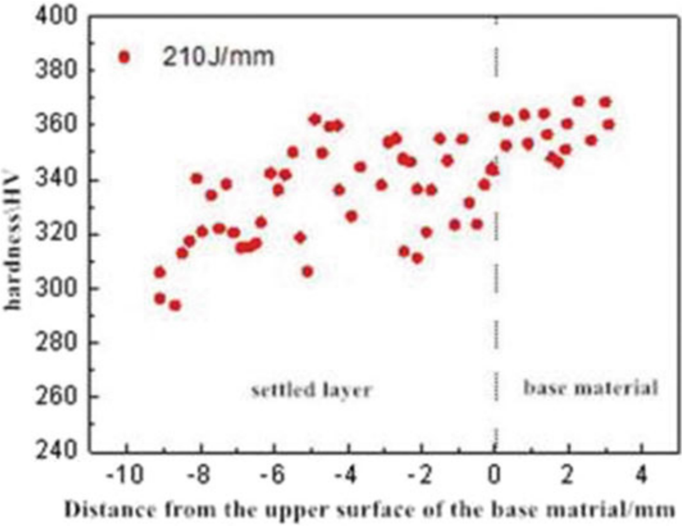

Fig. 11 Microhardness of the deposited layers

3.5 *Effect of Heat Input on Microhardness*

Figure 11 shows the results that microhardness measurement of the deposited layers with a heat input of 210 J/mm. As can be seen from the figure, there is no obvious difference in the hardness of the substrate area on the right, which is about 350 HV. With the height of the deposited layer increased, the hardness value gradually shows a discrete distribution, but the overall trend is decline. When the heat input amount is 210 J/mm, the overall hardness values are not much different and both fluctuate within 310–360 HV.

3.6 *Mechanical Properties of the Deposited Layers Electron Beam Freeform Fabrication*

Figure 12 and Table 1 show the tensile properties of the deposited layers in different directions. X_1–X_3 is the tensile properties from the bottom to the top of the deposited layers parallel to the deposition direction before heat treatment, and X_4 and Z_2 are the tensile properties of the deposited layers in different directions after the solid solution aging. It can be seen from the graph that the tensile strength of specimen X_1 in the bottom of the deposited layers is relatively the lowest, only 810.63 MPa, and the extensibility is also slightly lower than other positions at 5.23%. With the increase of the height, the tensile strength of the specimen X_2 in the middle of the deposited layers slightly increases to 816.29 MPa and the extensibility also rises to

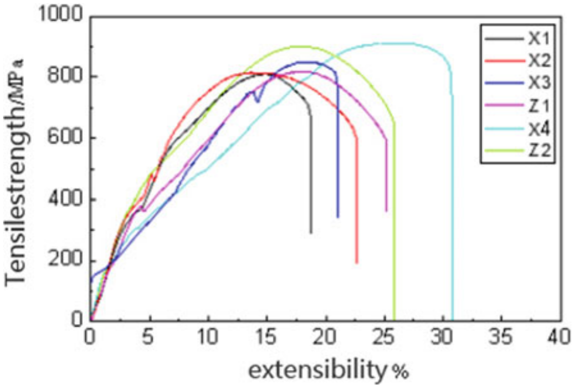

Fig. 12 Extensibility of deposition layer in normal temperature

Table 1 Tensile properties of specimens after solution aging

Tensile specimen	Tensile strength (MPa)	Extensibility (%)
Before heat treatment X_1	810.63	5.23
Before heat treatment X_2	816.29	8.65
Before heat treatment X_3	851.65	7.03
Before heat treatment Z_1	819.12	9.14
After heat treatment X_4	911.87	10.72
After heat treatment Z_2	893.67	9.81
TC4 base material	998	8.45
AMS4999A standard X	≥889	≥6
AMS4999A standard Z	≥861	≥5

8.65%. At the bottom of the deposited layers, the specimen X_3 has the highest tensile strength at 851.65 MPa and the extensibility can be maintained to 7.03%. The tensile strength of the specimens in the Z-direction is equivalent to that in the bottom and middle of the deposited layers in the X-direction, while the tensile strength differs by 32.53 Mpa from that in the top of the deposited layers. The tensile strength in all directions in the deposited layers is lower than that of the base material, and the extensibility in the Z_1-direction alone is slightly higher than that of the base material. X_4 and Z_2 are the tensile properties in different directions of the deposited layers after solution aging. Due to the effect of homogenization heat treatment, the mechanical properties of the deposited layers along the X-direction do not have the stratification phenomenon looked like the case before heat treatment. In other words, with the increase of the height of the deposited layers, the tensile strength in the X-direction does not change significantly.

The analysis shows that the stratification mechanical properties in the X-direction before solution aging are mainly caused by the heterogeneous microstructure of the deposited layers generated from different thermal cycles at different heights. The microstructure of X_1 is mainly lath-shaped α phases with large length and width, and the morphology of the α phase hinders the slip deformation, which makes it easy to produce cracks caused by local stress concentration at the interface between α phase and β phase when the specimen is subjected to tensile force so that the plasticity of the specimen is relatively low. At the same time, because the deposited environment is in vacuum in which the heat of deposition layer is difficult to dissipate and the subsequent deposition process will repeatedly heat the lower part of the deposited layers, producing an annealing-like effect to reduce the number of dislocations, the tensile strength at the bottom of the deposited layers is slightly decreased. The microstructure of X_2 in the middle of the deposited layers also undergoes annealing, so that the tensile strength is equivalent to that of the bottom while the aspect ratio of the microstructure of X_2 is significantly lower than that of X_1 and most of them are short rod-like α phase. Due to the short rod-like α phase which can absorb more energy during the crack, propagation phase belongs to the soft region in the β transition structure with the relatively good plasticity, thus the tensile strength in the middle of the deposited layers is not much different from the bottom but the plasticity is improved. In the microstructure of X_3 specimen that is the upper part of the deposited layers, there are many slender α clusters of close-packed hexagonal structure which has few slip systems and poor slip deformation energy, resulting in high resistance to dislocation movement and high tensile strength during the slip process. Therefore, the tensile strength in the upper deposited layers is higher than that of the middle and bottom as well as the tensile strength of the specimen in the Z-direction of the deposited layers is equal to that in the middle and bottom part of the X-direction. When the coarse columnar crystals on the surface are improved, the anisotropy in the deposited layers is reduced. However, after solution aging, the tensile strength of the deposited layers in the X_4 direction is 911.87 MPa with the extensibility is 10.72% and the tensile strength which is 893.67 MPa with that the extensibility is 9.81% in the Z_2-direction is slightly lower than the X_4 direction. Compared with the tensile properties of the specimens before solution aging, it can be seen that the tensile strength in the X_4-direction is increased by 60.22 MPa with the extensibility is increased by 3.69% and the tensile strength in the Z_2-direction is increased by 74.55 MPa, but the extensibility has no significant change. The tensile strength of the X_1 specimens before heat treatment does not meet the minimum requirements of the standard [21]. The tensile strength of the specimens in different directions after homogenization heat treatment meets the standard requirements, and the extensibility is significantly higher than the lower limit of the standard.

The concept of anisotropy index [22], index of plane anisotropy (IPA), is introduced to investigate the anisotropy of the deposited layers. IPA can be calculated by the following formula:

$$\mathrm{IPA} = \{[(n-1)\mathrm{X}_{\max} - \mathrm{X}_{\mathrm{mid}} - \mathrm{X}_{\min}]/(n-1)\mathrm{X}_{\max}\} \times 100 \tag{1}$$

In theory, the less obvious the anisotropy of the material, the more its IPA value tends to zero. In this test, since only the X-direction and Z-direction are tested for mechanical properties, the formula can be simplified as:

$$\mathrm{IPA} = [\mathrm{X_{max}} - \mathrm{X_{min}}/\mathrm{X_{max}}] \times 100 \tag{2}$$

where X_{max} is the larger of the two directions, X_{min} is the smaller value, and the anisotropy index of each position of the deposited layers calculated by the formula is shown in Table 2. It can be found from Table 2 that the IPA values of the ultimate tensile strength (UTS) are significantly smaller than the IPA values of the total extensibility (TE) in different positions of the deposited layers. The anisotropy in the middle of the deposited layers is the least obvious, because the middle part of the deposited layers is continuously heated by the upper part during the deposited process, while the heat dissipation of the middle part is slower and the heat preservation effect is good, which is equivalent to the continuous heat treatment for the middle part of the deposited layers, so the anisotropy in the middle part is reduced. The anisotropy in the upper part of the deposited layers is most obvious because the upper part is directly cooled from the molten state without a subsequent deposited process. The bottom part of the deposited layers has better heat dissipation conditions but the effect of heat treatment is not as good as the middle part, so the anisotropy is between the upper and middle. Compared with the IPA value of the specimen before heat treatment, the IPA-UTS value and the IPA-TE value of the specimen X_4-Z_2 after heat treatment are between the maximum value and the minimum value before the heat treatment. It indicates that the anisotropy of the deposited layers is further improved after heat treatment.

Figure 13 is SEM images of tensile fracture on specimens in different directions of the deposited layers. (a) The heat treatment front of specimen in the X-direction is stretched to exhibit a tear-type fracture, the surface is inhomogeneous, and sharp protrusions are distributed throughout the section. When the surface is enlarged, it can be clearly seen that there are fine equiaxed dimples uniformly distributed on the fracture surface; (b) is the fracture morphology in the X-direction after heat treatment, which has the characteristics of smooth fracture of homogeneous material without obvious fiber region and shear lip. After the fracture is enlarged, it can be seen that it has obvious ductile fracture characteristics, and the fracture is covered with equiaxed dimples; (c) is the fracture morphology of specimen in the Z-direction of the heat treatment front after stretching, showing ductile fracture. The specimen has obvious necking shrinkage before fracture. When the fracture is enlarged, it could be seen that there are also a large number of dimples with large differences on the fracture surface; (d) is the fracture surface of specimen in Z-direction after heat treatment, which appears partial step-like stratification, but the height difference of the step surface is very small, showing the characteristics of transgranular fracture.

Table 2 Anisotropy index of mechanical properties of specimens at different positions of the deposited layers

Tensile specimen	IPA-UTS	IPA-TE
X_1-Z_1	1.04	23.51
X_2-Z_1	0.35	9.9
X_3-Z_1	3.82	16.35
X_4-Z_1	1.99	15.98

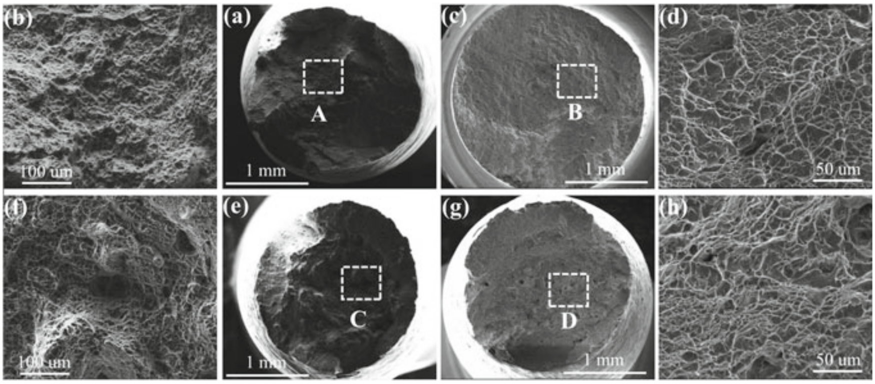

Fig. 13 Fracture morphology of specimen **a** X-direction before heat treatment; **b** X-direction after heat treatment **c** Z-direction before heat treatment; **d** Z-direction after heat treatment

When the fracture is enlarged, it can be seen that the surface of the fracture is full of dimples with non-uniform size and different depth. Compared between (a) and (c), different sizes of dimples are distributed in the protuberances and depressions of the region, resulting in overall unevenness and large fluctuation. As well as (b) and (d), the fracture surface is slightly smooth without step-like stratification, and the extensibility in the X-direction is higher than that in the Z-direction.

4 Conclusions

- The sample undergoes different thermal cycles during the deposition process, resulting in different characteristics of the phase microstructure in the height direction. The structure of α phase in the heat-affected zone changes from equiaxed structure of annealed base material to basket weave structure. The structure of α phase in the first 40 layers of the deposition presents the characteristics of gradient change, while the latter 20 layers mainly consist of $\alpha + \alpha'$ phase. The hardness of deposition layer decreases with the increase of height.
- Before heat treatment, the microstructure of the deposited layers along the height direction is not uniform, which leads to the characteristic of stratification mechanical properties in the X-direction. The tensile strength gradually increases in the X-direction from bottom to top and the anisotropy of the specimens in the middle of the deposited layers is the minimum. The tensile strength in the Z-direction is the same as that of the middle and bottom parts in the X-direction with a difference of 32.53 Mpa from that of the upper part in the X-direction. The fracture of the specimen in the X-direction is tear-type fracture, and the fracture of the specimen in the Z-direction is ductile fracture.
- After solid solution aging, the homogeneity of the structure in the deposited layers is significantly improved and the mechanical properties are optimized to meet the

requirements of AMS 4999A standard. At the same time, the anisotropy of the deposited layers reduces further. The tensile specimens change from a tear-type fracture to a smooth fracture in the X-direction as well as from a ductile fracture to a step-like fracture in the Z-direction.

Acknowledgements The authors would like to acknowledge the Aviation Science Fund (2017ZE56010) and the Jiangxi Province Advantage Science and Technology Innovation Team Key Project (20181BCB19002).

References

1. Zhang XJ, Tang SY, Zhao HY et al (2016) Research status and key technologies of 3D printing. J Mater Eng 44(2):122–128
2. Lin X, Huang WD (2015) High performance metal additive manufacturing technology applied in aviation field. Mater China 34(9):684–688
3. Zou W (2016) Application and prospect of titanium alloy in aerospace industry. China Nonferrous Metals (1):70 (in Chinese)
4. Liu Y, Chen Z, Jin T, Chai L (2018) Present situation and prospect of 600 °C high-temperature titanium alloys. Mater Reports China 32(6):1863–1869
5. Kobryn PA, Semiatin SL (2001) The laser additive manufacturing of Ti-6Al-4V. JOM 53 (9):40–42
6. Wang H, Zhang L, Li A et al (2004) Rapid solidification laser advanced materials processing and manufacturing. Beijing Univ Aeronaut Astronaut 30(10):962–967
7. Baufeld B, Brandl E, van der Biest O (2011) Wire based additive layer manufacturing: comparison of microstructure and mechanical properties of Ti-6Al-4V components fabricated by laser-beam deposition and shaped metal deposition. J Mater Process Technol 211(6):1146–1158
8. Kelly S, Kampe S (2004) Microstructural evolution in laser-deposited multilayer Ti-6AI-4V build s: part II. Thermal modeling. Metall Mater Trans A 35(6):1869–1879
9. Chen G, Xi S et al (2018) Development status of electron beam fuse deposition additive manufacturing technology at home and abroad. Trans China Weld Inst 39(8):123–128
10. Stecker S, Lachenberg KW, Wang H et al (2006) Advanced electron beam free form fabrication methods & technology. Session 2:12
11. Yan W, Yue Z, Zhang J (2016) Study on the residual stress and warping of stiffened panel produced by electron beam freeform fabrication. Mater Des 89:1205–1212
12. Pan S (2014) Research on high-energy beam rapid prototyping of TC4 titanium alloy [D]. Harbin, Northeastern University
13. Chen Zheyuan, Suo Hongbo, Li Jinwei (2010) The forming character of electron beam freeform fabrication. Aerosp Manufact Technol 1:40–43
14. Suo HB, Liu JR, Gong SL et al (2014) Microstructure and mechanical properties of Ti-6Al-4V fabricated by electron beam rapid manufacturing. Rare Metal Mater Eng 43(4):0780–0785
15. Bush RW, Brice CA (2012) Elevated temperature characterization of electron beam free form fabricated Ti-6Al-4V and dispersion strengthened Ti-8Al-1Er. Mater Sci Eng A 554:12–21
16. Glavicic MG, Kobryn PA, Bieler TR et al (2003) An automated method to determine the orientation of the high-temperature beta phase from measured EBSD data for the low-temperature alpha-phase in Ti-6Al-4V. Mater Sci Eng A 351(1–2):258–264
17. Shewei Xin, Yongqing Zhao (2006) Discussion on heat treatment and precipitation phase of titanium alloy. Heat Treat Met 31(9):39–42
18. Bush RW, Brice CA (2012) Elevated temperature characterization of electron beam freeform fabricated Ti-6Al-4V and dispersion strengthened Ti-8Al-1Er. Mater Sci Eng A 554(5):12–21

19. Brice CA, Fraser HL (2003) Characterization of Ti-Al-Er alloy produced via direct laser deposition. J Mater Sci 38(7):1517–1521
20. Suo H (2014) Microstructure and mechanical properties of Ti6Al4V produced by electron beam rapid manufacturing. Wuhan, Huazhong University of Science and Technology
21. AMS 4999A (2011) Titanium alloy direct deposited products Ti-6Al-4V annealed. Society of automotive engineers (SAE)
22. Banumathy S, Mandal RK, Singh AK (2010) Texture and anisotropy of a hot rolled Ti-16Nb alloy. J Alloy Compd 500(2):26–30

Weld Flaw Recognition with Improved Convolutional Neural Network

Ande Hu, Ding Fan, Jiankang Huang, and Zhenya Xu

Abstract The simple linear iterative clustering (SLIC) algorithm and the improved exponential linear unit (ELU) activation function are used to construct CNN model for weld flaw detection image recognition. First, the ELU activation function is used in the CNN model to generate better robustness to the input noise when the response gradient disappears. At the same time, the SLIC algorithm is used to perform pixel block processing on image pixels, which increases the proportion of interest regions in the weld flaw detection image and improves the feature extraction ability of the model during training. Through the extraction of the interest region of weld detection image and the establishment of the CNN model described in this paper, the results show that the proposed method has better performance than the traditional convolution neural network in feature extraction, training time, and recognition accuracy of weld flaw detection image.

Keywords Weld defect recognition · Convolution neural network · SLIC algorithm · ELU function

1 Introduction

In pipeline welding, various defects are caused by the stability of various parameters during welding process, which are mainly divided into external defects (undercut, overlap, excessive penetration, etc.) and internal defects (crack, gas pore, slag inclusion, incomplete penetration, etc.) [1]. In industrial production, the internal defects of the weld are often detected by the radiation detection technology. It is particularly necessary to find a method for automatic detection and identification of welding

---

A. Hu · D. Fan (✉) · J. Huang · Z. Xu
State Key Laboratory of Advanced Processing and Recycling Non-Ferrous Metals, Lanzhou University of Technology, Lanzhou 730050, China
e-mail: fand@lut.cn

Baoshan Iron and Steel Co., Ltd, Shanghai 201900, China

© Springer Nature Singapore Pte Ltd. 2020

S. Chen et al. (eds.), *Transactions on Intelligent Welding Manufacturing*,
Transactions on Intelligent Welding Manufacturing,
https://doi.org/10.1007/978-981-15-7215-9_3

defects in view of the problems of missed detection, wrong inspection, and inefficiency in the current defect detection, which can lead to the defect detection more efficient, standardized, and intelligent [2].

The convolutional neural network (CNN) does not need to manually describe and extract the target image. The neural network can learn features from the training samples autonomously, and these features are closely related to the classifier, which can solve the problems of artificial extraction and classifier selection, using its 'end-to-end' advantage to solve some problems that are considered difficult to solve in the nowadays flaw detection of image defects. The widely used CNN model is a simplified version of the Hubel–Wiesel model [3]. And the research of this model mainly focuses on algorithm improvement [4] and structural improvement for different fields [5]. The deep learning model improved by the algorithm has achieved remarkable results in image recognition, but it still has some shortcomings. For example, the target area is small in the image, resulting in local information redundancy in the target image. In addition, the redundant information in the CNN training process increases the calculated data and noise, which has an impact on the training time and the fitting effect. In addition, ReLU acts as a non-saturated activation function, and there is a phenomenon of neuron death during training. When a large gradient attenuation flows through the neuron and updates the parameters, the neuron will no longer appear to be activated. If there is a large learning rate, then it leads to excessive neuronal death, affecting the correct rate of training.

In view of the above problems, this paper uses exponential linear unit (ELU) improved activation function [6] feature model selection method and simple linear iterative clustering (SLIC) algorithm [7] to identify weld image defects, study the algorithm, and improve the activation function in the weld flaw detection image. The effect of validity and correct rate is in defect identification.

2 Feature Selection Method Based on Improved CNN

2.1 ELU Activation Function Analysis

For the neural network, the activation function can be used to introduce nonlinear transformation to the neuron, and the neural network can be approximated by any nonlinear function through training, then the different features of the function in the network recognition can be fitted. The sigmoid function has an exponential function shape, which is similar to biological neurons and is widely used in artificial neural networks. However, its output in the x-direction gradually approaches zero and has soft saturation. Once it enters the saturation region during training, appearing gradient disappearance will make it difficult to effectively train the network parameters. The unilateral suppression ability of the ReLU function can make the neurons in the network sparsely activating, and thus better mine relevant features and fit the training data, effectively solving the gradient explosion/gradient disappearance problem. It

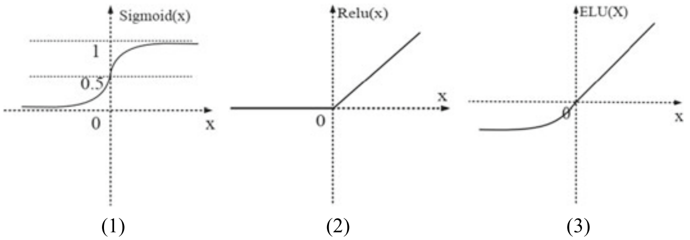

Fig. 1 Activation functions: **1** sigmoid function; **2** ReLU function; **3** ELU function

can be seen that when $x > 0$, there is no saturation problem in the ReLU function, and the gradient can be kept attenuated during the training process, thereby alleviating the problem of gradient disappearance. When $x < 0$, hard saturation occurs. As the training progresses, some of the inputs enter the hard saturation zone, causing the weights to be unchanged. Therefore, the ReLU activation function is weak in the network training process, and the problem is that the neurons no longer react when the large gradient flows through the neurons and updates the parameters.

For the problems in traditional convolutional neural networks, this paper adopts an ELU nonlinear activation function that can comprehensively consider the saturation of the activation function. The activation function can fuse the advantages of the sigmoid and ReLU functions and maintain the unsaturation on the right side of the function. At the same time, the soft saturation on the left side of the function is increased, so that the non-saturation part can alleviate the gradient disappearance phenomenon during the model training process, and the soft saturation can make the model more robust to the input change or the existing noise. Various activation function images and expression are shown, respectively, in Fig. 1.

2.2 Principle and Application of SLIC Algorithm

The SLIC algorithm can transform the weld flaw detection image from pixel level to region level and divide into superpixel area. The main idea is to use the luminance component and the two hue components in the LAB color space and the x, y coordinates to form a five-dimensional space to clustering. The main steps are:

- dividing an image pixel into fixed pixel blocks by setting a predetermined parameter in an existing image and calculating pixel block seed point coordinates;
- Calculating the pixel value of the minimum gradient using the 8-chain code pixel of the seed point and using it as a new seed point;
- After traversing the seed points, cluster the pixels by K-means clustering method;
- Calculate the distance between the pixel and the seed point by the transformed Euclidean distance.

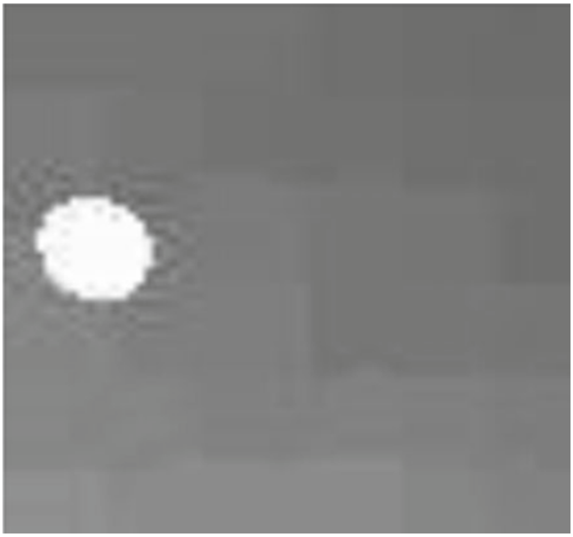

Fig. 2 SLIC algorithm iterative processing

Applying the SLIC algorithm to the weld flaw detection image can reduce the redundancy of local information in the image. The iterative segmentation process is used to obtain the image that satisfies the training. Figure 2 shows the stomatal defect image after pixel block, in which the number of seed points is 30.

2.3 Defect Type Identification Process Based on Improved CNN

In summary, the process of identifying the weld defect type based on the improved convolutional neural network model is shown in Fig. 3. The conventional image preprocessing of the weld flaw detection image meets the input requirements of the convolutional neural network model. Based on this, SLIC processing is performed on the image. By constructing a convolutional neural network model with different activation functions and loading the image data for training and verification, the effects of different activation functions and preprocessed images on training and recognition results are analyzed.

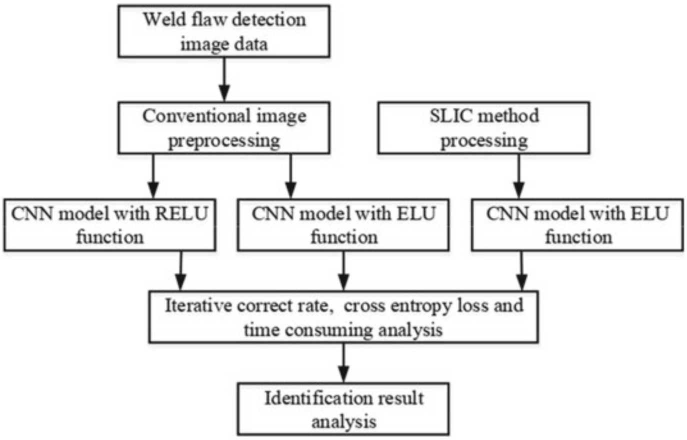
Weld flaw detection image data
Conventional image preprocessing
SLIC method processing
CNN model with RELU function
CNN model with ELU function
CNN model with ELU function
Iterative correct rate, cross entropy loss and time consuming analysis
Identification result analysis

Fig. 3 Defect identification flowchart

3 CNN Model Construction and Defect Identification

3.1 Improve CNN Model Construction

For the convolutional neural network model, the connection layer and depth of the convolutional neural network can be appropriately adjusted according to the size of the input layer. As the depth of the model increases, the learning effect is better, but increasing the depth of the network increases the calculation time. Meanwhile, the amount of training data increases the risk of overfitting when the training data is insufficient. Therefore, increasing the depth of the network layer in the experiment is not the first choice for the network model. In the establishment of the convolutional neural network model, the network parameters are effectively selected to obtain the maximum output with the smallest number of layers. By connecting the local receptive fields of each feature surface, the original pixels of the input image are mapped in a hierarchical manner to extract the receptive fields within each layer. The characteristics of the use of weight sharing strategy to reduce the amount of data in the neural network and additional changes to the activation function to reduce the complexity of the model make the network easier to train. Figure 4 shows the *n*-layer convolutional neural network and BP neural network.

In order to verify the effectiveness of the proposed method, models named CNN-1, CNN-2, and CNN-3 were constructed. CNN-1 model converted ELU function layer to ReLU activation function based on CNN-2 model, and CNN-3 model trains the image data obtained by the SLIC method. The construction methods of each model are shown in Table 1. By constructing different CNN models for comparison experiments, the CNN-1 and CNN-2 model experiments were trained with images not processed by SLIC, and the effectiveness of the ELU activation function was verified by training with different activation functions. Both the CNN-2 and CNN-3

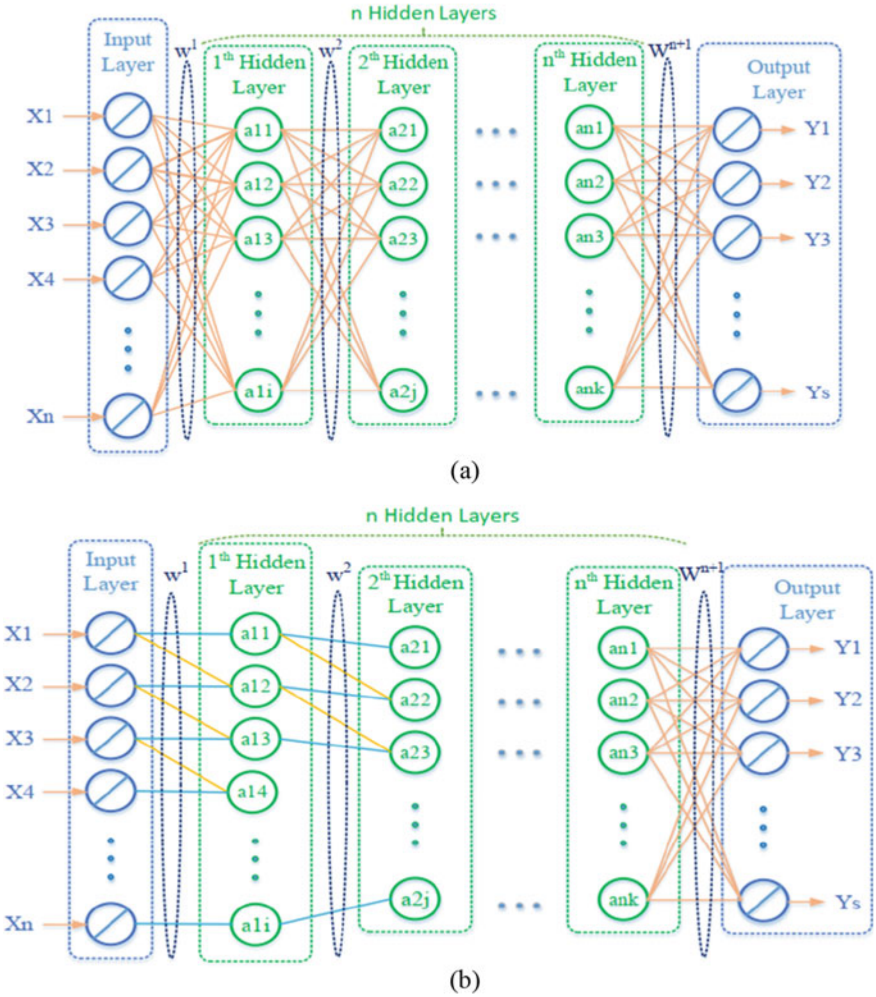
n Hidden Layers
Input Layer
w1
1th Hidden Layer
w2
2th Hidden Layer
nth Hidden Layer
Wn+1
Output Layer
X1
X2
X3
X4
Xn
a11
a12
a13
a1i
a14
a21
a22
a23
a2j
an1
an2
an3
ank
Y1
Y2
Y3
Ys

(a)

(b)

Fig. 4 Neural network: **a** BP neural network, **b** convolutional neural network

Table 1 Model construction method

CNN model name	Training images	Activation function
CNN-1	No SLIC processing	RELU
CNN-2	No SLIC processing	ELU
CNN-3	SLIC processing	ELU

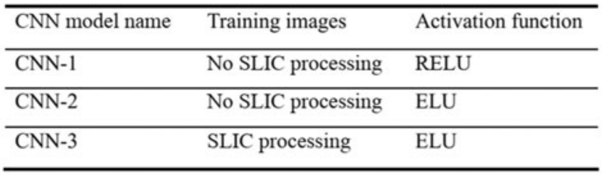

CNN model name	Training images	Activation function
CNN-1	No SLIC processing	RELU
CNN-2	No SLIC processing	ELU
CNN-3	SLIC processing	ELU

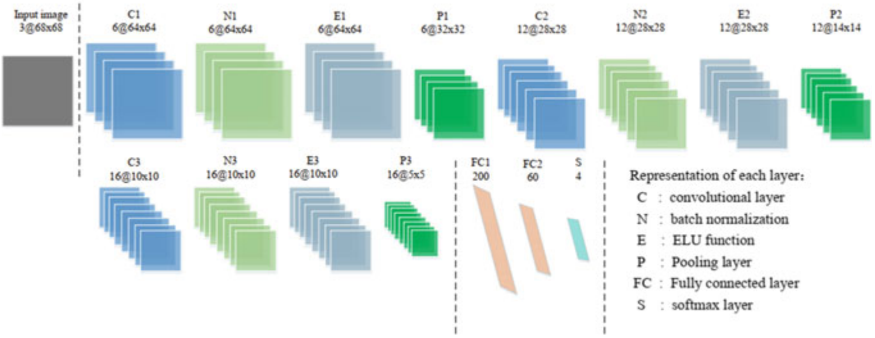
Input image
3@68x68
C1
6@64x64
N1
6@64x64
E1
6@64x64
P1
6@32x32
C2
12@28x28
N2
12@28x28
E2
12@28x28
P2
12@14x14
C3
16@10x10
N3
16@10x10
E3
16@10x10
P3
16@5x5
FC1
200
FC2
60
S
4
Representation of each layer:
C : convolutional layer
N : batch normalization
E : ELU function
P : Pooling layer
FC : Fully connected layer
S : softmax layer

Fig. 5 Improved convolutional neural network model

model tests use the ELU activation function to verify the effectiveness of the SLIC method in this paper by training different weld flaw detection images. The CNN-2 model is shown in Fig. 5. The input image is the input layer, C is the convolution layer, the size of the convolution kernel is 5×5, and the depth is 6, 12, 16. The unit is composed and optimized by the back propagation algorithm to obtain the convolution unit parameters, and the more complex features are extracted iteratively by extracting the different features of the input. N is regularized and can constrain the convolution result. E is the ELU activation function, and the calculation result is de-linearized by the ELU function. P is the pooling layer, the convolution kernel size is set to 2×2, the moving step size is 2, and both the convolutional layer and the pooled layer are filled with all 0. FC is a fully connected layer, and the number of nodes is reduced to 60 by two layers of fully connected layers. Because the defect type identified by the CNN to be classified in this paper is of four types, the number of output layers S is set to 4.

3.2 Overview of Weld Flaw Detection Image Dataset

The weld ray inspection image selected in this paper consists of two parts, one part is taken from the public database named GDXray [8], and the other part is the ray inspection image of the pipe weld provided by a domestic welding processing enterprise. The image has a small area of interest, while the weld flaw detection image has a large proportion of the area of non-interest, and it is more difficult to train with the whole image. Therefore, the image preprocessing is performed before

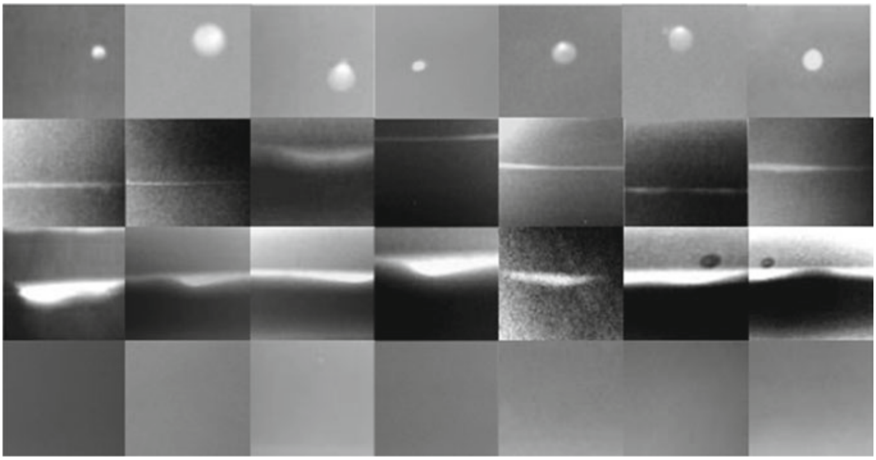

Fig. 6 Partial experimental image data

the CNN model is trained. According to the type and size of the flaw detection image defect, the 68×68 size of the defect in the weld is taken as the region of interest. To further increase the weld flaw detection image, the amount of training data is expanded by 1:10 using image enhancement technology. The expanded weld flaw detection image dataset contains 1255 gas pore images, 200 incomplete penetration images, 75 lack of fusion images, and 1140 flawless pictures; all images are divided into training set and verification set by 4:1. Figure 6 is a partial weld defect image taken.

3.3 *Image Defect Recognition and Analysis*

The test is based on the Linux Ubuntu 16.04 operating system, Inter (R) Core (TM) i5-2400 CPU@ 3.10 GHz processor, under the TensorFlow framework. Using the image dataset provided in this paper, the CNN-1, CNN-2, and CNN-3 models are trained 10,000 times, and the correct rate and cross-entropy loss can be obtained by model iteration as shown in Fig. 6a, b, and the model iteration time is shown in Table 2. It can be seen from the analysis of Fig. 7 and Table 2 that under the

Table 2 Iteration time of each model

CNN model name	Training image	Activation function	Time-consuming reduction
CNN-1	No SLIC processing	RELU	0
CNN-2	No SLIC processing	ELU	1.07%
CNN-3	SLIC processing	ELU	12.87%

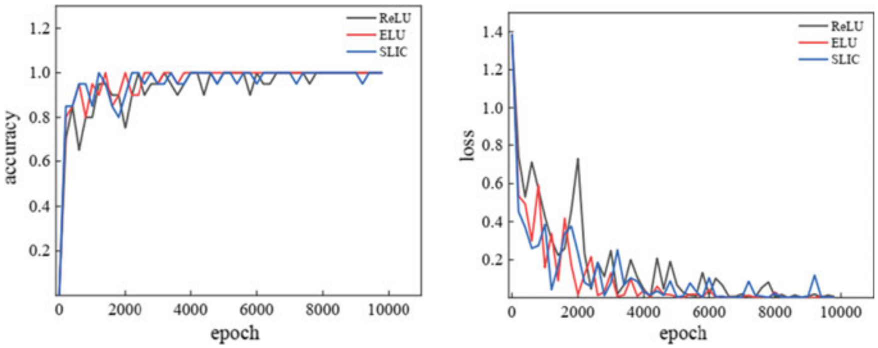

(a)Iterative correct rate (b) Iterative cross entropy loss

Fig. 7 Iterative correct rate and cross-entropy loss. **a** Iterative correct rate. **b** Iterative cross entropy loss

same number of iterations, the CNN model with ELU activation function used in this paper converges faster than the CNN model of ReLU activation function, and the convergence speed in the early iteration is better than that in SLIC method. The training process of the seam image is slow, but the degree of gradient change during the iteration is small. According to the time comparison of different models under the same number of iterations, the CNN model with ELU activation function has a smaller iteration time than the ReLU activation function, but the reduction time is limited, and the CNN model based on SLIC method takes more time to iterate than the other two. The models have been greatly reduced, with a reduction of 12.87%. It can be seen that the SLIC method is used to pixel block the pixel of the weld flaw detection image, which reduces the information redundancy of the weld flaw detection image and effectively reduces the training iteration time, but the method will be in the pixel block. The effect of the amplification noise on the training process is made to make the convergence effect worse during the iterative process in the later stage of training. The improved CNN model has better robustness in input variation or noise presence than the ReLU activation function and can maintain the sparsity of the network during training, meanwhile reducing the risk of accuracy while number of neurons entering the hard saturation region and reducing iterative recognition.

In order to further verify the validity and reliability of the model in the image detection of weld flaw detection, another part of the weld flaw detection image is tested. In the test results, two fault categories are randomly selected and numbered. The recognition results are shown in Table 3. The four numbers in the parentheses of the classification result indicate the probability that the image to be identified is flawless, incomplete penetration, lack of fusion, and gas pore after being calculated by the softmax layer. The maximum probability value determines the defect type of the classification result. It can be seen that CNN-1 was detected the no. 1 lack of fusion defect sample to no. 5 as incomplete penetration, and the probability values in the recognition result are similar, while CNN-2 and CNN-3 have correctly made

Table 3 Weld flaw detection image recognition result table

Experiment	Test sample	CNN-1 (%)	CNN-2 (%)	CNN-3 (%)
1	Flawless	99.9	99.7	99.9
2	Flawless	99.9	99.8	99.9
3	Gas pore	99.9	99.9	99.9
4	Gas pore	99.9	99.9	99.9
5	Incomplete fusion	49.9	56	60.1
6	Incomplete fusion	79.7	54.9	93.6
7	Incomplete penetration	85.9	93.6	96.8
8	Incomplete penetration	90.7	92.5	97.3

the identification samples of the number. Identification, the recognition probability value of the lack of fusion sample no. 1 is very different, indicating that the method has more advantages in feature extraction. Through the overall test sample identification analysis, the proposed method can effectively identify four types of weld flaw detection images, and the overall recognition accuracy rate can reach 97.8%, which is accurate in realizing various defects existing in the weld image. Subdivision identification is completely predictable.

4 Conclusion

In this paper, a new method of image processing and improved activation function of CNN model for weld defect identification is adopted. The SLIC is used to perform pixel block processing on weld flaw detection image and CNN model using ELU activation function, which effectively reduces training iteration and time-consuming. Reducing the hard saturation of the CNN model and verifying the effectiveness of the method are adopted in this paper through comparative experiments.

1. The ELU activation function is used in the construction of CNN model to make the model have better robustness in the training process, and the convergence speed is increased by good network sparsity and smaller output mean.
2. The SLIC method can effectively block the pixels in the weld flaw detection image, increase the proportion of the interest region in the image, enhance the extraction of image features during training, and reduce the redundancy of local information. In addition, the iteration time in the training process is reduced, and the overall degree of reduction needs further improvement.
3. The CNN model constructed by the SLIC method and ELU activation function provided in this paper can be applied to the field of automatic detection of weld flaw detection images and can significantly improve the recognition accuracy of defects in weld flaw detection images. The overall recognition rate can reach 97.8%, the accurate subdivision identification of various defects existing in the

weld image is completely predictable, and the method is versatile and can be extended to other fields.

4. References.

References

1. Wang F, Zhu JJ (2017) Research of machine vision for welding defect in complex environment. Weld Technol 5:127–133
2. Sun Y, Song H-y, Bai P et al (2004) Real-time automatic detection of weld defects in X-ray images. Trans China Weld Inst 25(2):115–118
3. Zhou F-Y, Jin L-P, Dong J (2017) Review of convolutional neural network. Chin J Comput 40(6):1229–1251
4. Boureau Y, Roux NL, Bach F et al (2011) Ask the locals: multi-way local pooling for image recognition[C]. In: IEEE international conference on computer vision. IEEE
5. Wu X, He R, Sun Z et al (2018) A light CNN for deep face representation with noisy labels. IEEE Trans Inf Forensics Secur 13(11):1–11
6. Gu J, Wang Z, Kuen J et al (2018) Recent advances in convolutional neural networks. Comput Sci 77:354–377
7. Achanta R, Shaji A, Smith K et al (2012) SLIC superpixels compared to state-of-the-art superpixel methods. IEEE Trans Pattern Anal Mach Intell 34(11):2274–2282
8. Mery D, Riffo V, Zscherpel U et al (2015) GDXray: the database of X-ray images for nondestructive testing. J Nondestr Eval 34(4):1–12

Mask R-CNN-Based Welding Image Object Detection and Dynamic Modelling for WAAM

Chunyang Xia, Zengxi Pan, Shiyu Zhang, Joseph Polden, Huijun Li, Yanling Xu, and Shanben Chen

Abstract As a new emerging technology, wire arc additive manufacturing (WAAM) has attracted extensive interests from both academia and industry during recent years. WAAM uses welding arc as an energy source to fuse metal wire and deposit layer by layer, which provides the advantages of freeform deposition. In order to improve its manufacture precision, stability and repeatability, it is necessary to develop sensing and control strategy for WAAM process. This research develops a passive visual sensing system for a robotic WAAM system. A new deep learning technique (Mask R-CNN) is proposed to detect and segment the melt pool area, and the width of melt pool can be measured based on the coordinate of the bounding rectangle. The pseudo-random ternary (PRT) signals were used to stimulate the WAAM process, and the corresponding width can be measured by the Mask R-CNN. Based on the width data and corresponding PRT input, a dynamic model of adaptive neuro-fuzzy inference system was built for the WAAM process.

Keywords Additive manufacturing · Vision · Melt pool · Mask R-CNN · ANFIS

1 Introduction

Wire arc additive manufacturing (WAAM) is an emerging concept in manufacturing fields during recent years, although the application of arc welding deposition appeared since 1925 [1]. WAAM utilizes electric arc as heat source to melt metal wire and deposits layer by layer in freeform (as shown in Fig. 1). Compared to powder-based additive manufacturing technologies, WAAM has the advantages

---

C. Xia · Z. Pan (✉) · S. Zhang · J. Polden · H. Li
School of Mechanical, Materials, Mechatronic and Biomedical Engineering,
University of Wollongong, Wollongong, NSW 2522, Australia
e-mail: zengxi@uow.edu.au

C. Xia · Y. Xu (✉) · S. Chen
School of Materials Science and Engineering,
Shanghai Jiao Tong University, Shanghai 200240, China
e-mail: ylxu@sjtu.edu.cn

© Springer Nature Singapore Pte Ltd. 2020

S. Chen et al. (eds.), *Transactions on Intelligent Welding Manufacturing*,
Transactions on Intelligent Welding Manufacturing,
https://doi.org/10.1007/978-981-15-7215-9_4

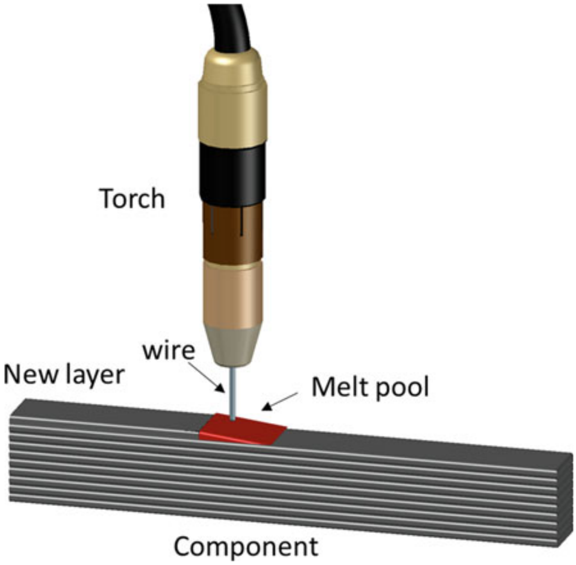

Fig. 1 Diagram of WAAM process

of high deposition rate and lower costs, which make WAAM more applicable for the production of large-scale complex components. Thus, WAMM has extensive potential applications in the modern industry, like the aerospace industry [2, 3], ship building [4] and construction industry [5].

Modern manufacturing states the importance of accuracy, stability and repeatability of production. This issue also exists in WAAM, since it is an emerging manufacturing technology. For example, the accuracy of dimensions for the final components may be influenced by the fluctuations of the machine or the variation of working conditions. Besides, with the deposited layers increasing, the heat accumulation will become more serious, and this will lead to the deposition process difficult to be controlled due to the varying thermal boundary condition. Ding et al. [6] pointed out that monitoring and process control for WAAM process will be a promising solution to achieve stability and repeatability.

With the development of computer vision, extensive studies have focused on visual information acquisition during the manufacturing process. Visual monitoring is able to obtain real-time information from the welding area, and closed-loop control could be implemented based on those information. In the arc welding area, a few researches work on visual monitoring and control has been implemented. Xu et al. [7] designed a passive visual sensor system for GTAW, and the image of welding pool and seam could be obtained during the base current period. Canny edge detection algorithm was used to extract the information of welding pool and seam. Fang et al. [8] developed a passive vision system (CCD + filter) to monitor the weld pool of hump formation during the GMAW process. The Chan–Vese (CV) model with fuzzy C-means (FCM) was proposed to segment the weld pool image. Guo et al. [9] utilized a passive visual sensor to acquire the weld image during MAG welding. An improved Canny algorithm and Hough transform were used for image processing, and the welding deviation between the wire line and V-groove centreline could be computed. In WAAM fields, some research works on monitoring and control have also been implemented. Comas et al. used a special welding camera to monitor the plasma WAAM process. The image of melt pool could be obtained. Through edge detection and Hough transform, the width of melt pool could be measured. Zhan et al. [10] also applied a weld camera to monitor the deflection of wire during WAAM process. Based on adaptive threshold and Hough transform, the wire edges were extracted and the coincident lines were merged. Furthermore, the wire deflection could be measured by the Radon transform. Xiong et al. [11] developed a passive visual sensor to measure the width of deposited layer during WAAM process, and closed-loop control was implemented.

In the above literature, the image processing methods are almost based on traditional edge extraction algorithms. However, the result of object detection and dimension measurement by the traditional method of image feature extraction is easily influenced by disturbance and may have poor stability. When application scenarios or working conditions vary, it may become hard to detect and measure the object accurately.

In recent years, computer vision technology developed rapidly due to the continuous update and perfect of deep convolutional neural network (CNN) technology, which has made a revolutionary development in the image processing field [12, 13]. Because of its advantages in detection and segmentation, it has gradually replaced a part of the traditional image processing method. At the same time, the accuracy of recognition and computational efficiency of the target detection algorithm have been rapidly improved. Combining regions proposal with CNN, Girshick et al. [14] proposed R-CNN to achieve detection and classification, which used selective search to extract the ROI of the input image. Considering the drawback of computational redundancy for R-CNN, Fast R-CNN was proposed by Girshick [15]. In Fast R-CNN, a ROI pooling layer was introduced to directly map the candidate boxes generated by the selective search algorithm, and then the network learns the region proposals. The amount of calculations for Fast R-CNN has been greatly reduced due to the decrease of feature extraction for each image. Furthermore, He et al. proposed Mask R-CNN, which developed Faster R-CNN [16] through introducing a branch to predict the segmentation masks on each region of interest (ROI). The mask branch is a fully convolutional network [17]. It was utilized on ROIs to predict a segmentation mask at an accuracy of pixel. The architecture of Mask R-CNN is summarized in Fig. 2.

Since the background of welding image is complex and noise may be generated in the image, the deep learning algorithm may provide advantages in extracting information from welding image. However, according to existing literature, the applications of deep learning in additive manufacturing or welding fields are still rare. This study aims to explore the feasibility of a deep learning framework in monitoring WAAM or welding process. As Kaiming He (inventor of Mask of R-CNN) said, this work, Mask R-CNN, outplays all current CNN models, even the winners in COCO 2016 challenge. Several recent works have applied Mask R-CNN to different fields from cellular biology [18] to Astronomical Sources [19]. Therefore, in this paper, a target

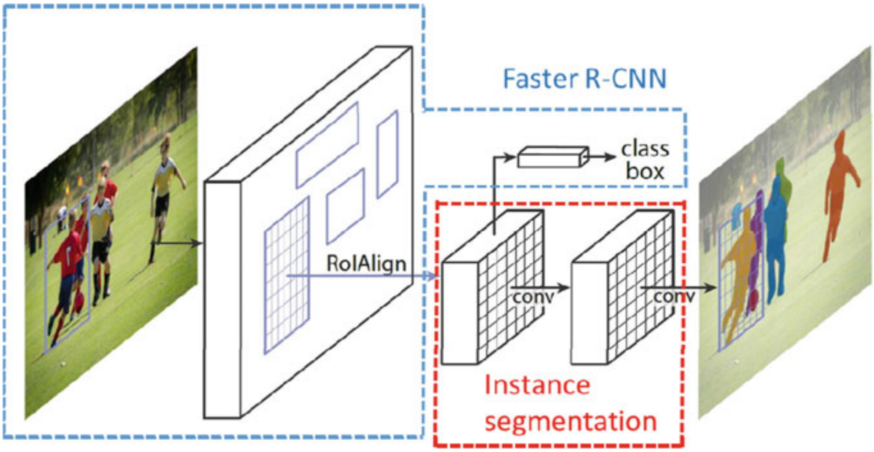

Fig. 2 Framework of Mask R-CNN

detection and segmentation method based on Mask R-CNN for welding image was proposed. The width of melt pool can be measured intelligently by the Mask R-CNN model. Based on this data, an adaptive neuro-fuzzy inference system (ANFIS) could be built to describe the dynamic process of WAAM.

This paper will be organized as follows. In Sect. 2, the experiment system is presented. In Sect. 3, the Mask R-CNN algorithm is introduced, and the detail of implementation in welding image is presented. In Sect. 4, based on the data measured by Mask R-CNN, dynamic models are built. Section 5 concludes this study.

2 Experimental System

The schematic chart of the experimental setup is illustrated in Fig. 3. It includes ABB robot, a Fronius CMT welder, a welding camera and a computer used for controlling. The camera used for melt pool monitoring is a Xiris XVC-1100 welding camera, which is combined with 650 nm narrow-band filter. The welding camera was fixed at the front of welding torch along welding direction. As shown in Fig. 4, the melt pool and wire can be observed clearly without arc disturbance.

The shielding gas used in experiments consisted of 80% Ar and 20% CO_2. The wire is 0.9 mm diameter of mild steel. The robot control cabinet is used for coordinating robot movements and welding processes. The real-time adjustment of wire feed speed (WFS) is implemented by changing the analogy input of the welder. The welding current and voltage were matched automatically by Fronius CMT welder according to WFS.

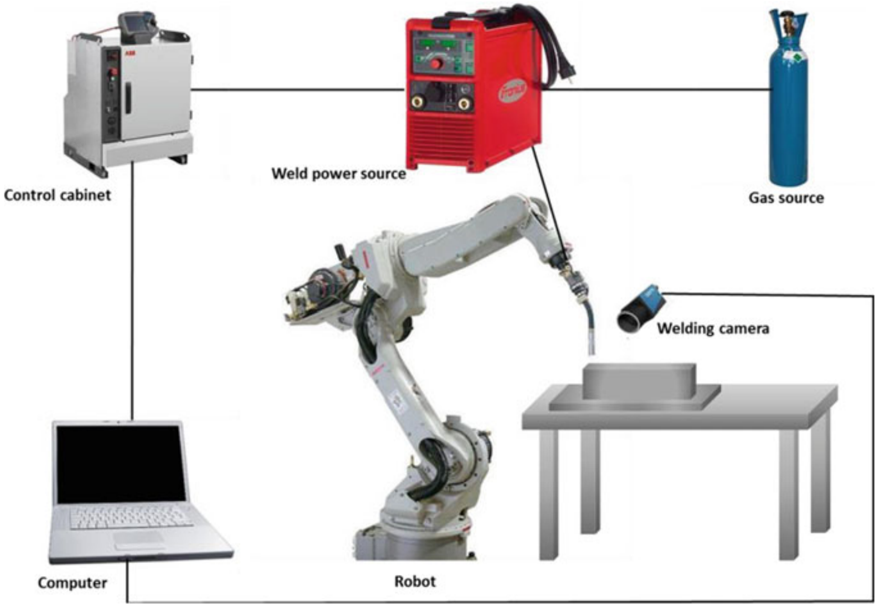
Control cabinet
Weld power source
Gas source
Welding camera
Computer
Robot

Fig. 3 Schematic diagram of the experimental set-up

Fig. 4 Example of welding image

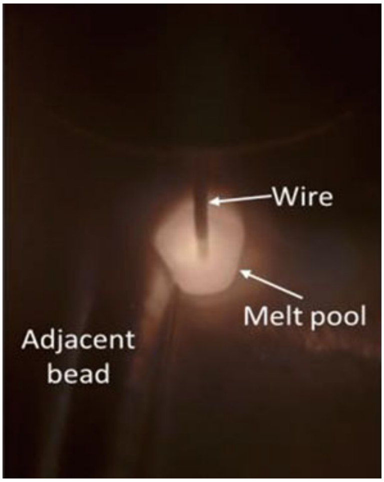
Wire
Melt pool
Adjacent bead

3 Mask R-CNN-Based Objective Detection and Segmentation

3.1 Configuration and Implementation

Mask R-CNN includes two branches: (1) the convolutional subject for feature extraction over the whole image and (2) the network head for bounding-box recognition (classification and regression) and mask prediction that is applied separately to each ROI [20]. ResNet-101-FPN was applied as the backbone architecture, and Faster R-CNN with ResNet was utilized as the head architecture. The ROI align layer is utilized to fix the misalignments between the ROI and the extracted features by RoI pool [15], which enables the network to predict masks at an accuracy of pixel.

This work utilized Python language to implement Mask R-CNN model, which was developed from the work of Abdulla [20]. The code in this paper is developed on Google Colab [21] using TensorFlow backend. In this work, we implement two ROIs classifications and segmentation: melt pool and wire. The background class can be ignored in this study.

3.2 Training and Evaluation

Because CNN consists of multiple layers, a large number of model parameters are included, which will lead to a slow convergence rate during training. Besides, the over-fitting phenomenon may happen, which will weaken the generalized ability for the model. Therefore it is crucial to initialize the model appropriately. When CNN is used for target detection, the pre-trained network weight is usually used as the starting point, which is obtained through training on public data set, such as ImageNet, Caltech-256 and COCO.

In this study, we used the pre-trained weights of Mask R-CNN to start with, which has been trained on COCO data set [21] for object detection. Then, training data set of welding images will be used for transfer learning. Each training image is labelled as three parts: melt pool, wire and background. The training samples have annotated the labels of melt pool and wire in AGG image annotator (VIA) [22]. Melt pool and wire were labelled with polygonal regions as shown in Fig. 5, and the json files which contained the annotation information were generated by AGG for training. The mask for different objects will be generated for training by this Mask R-CNN framework, and an example of a typical training set image with its melt pool and wire masks is shown in Fig. 6.

In our study, the training process can be divided into two stages: heads layer training and fine-tune all layers. At the first stage, only the initialized layers were trained while other layers were fixed. Then, all layers were fine-tuned. During those

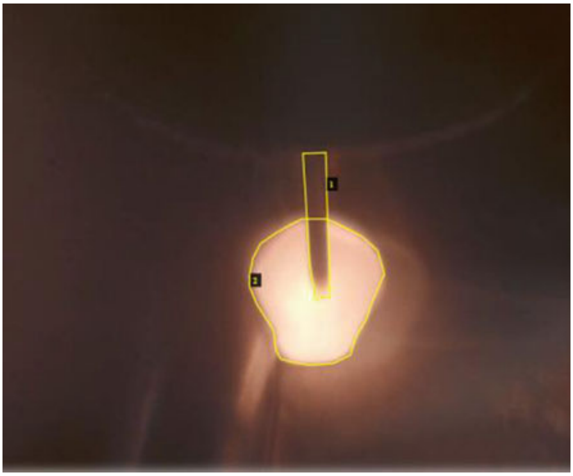

Fig. 5 Example of annotation for welding image

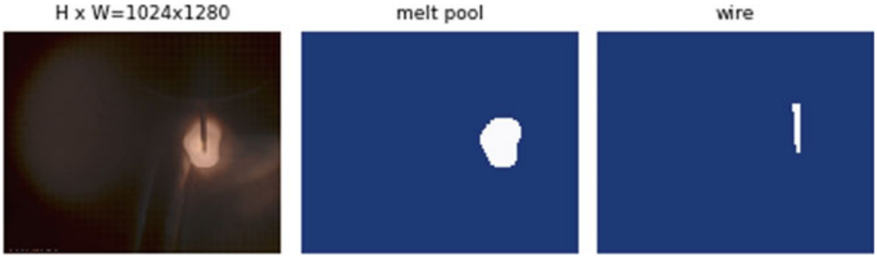

Fig. 6 Typical example of training data

two stages, the network is trained by stochastic gradient descent [23]. Stochastic gradient descent updates the network weights θ_j through minimizing the cost function $J(\theta)$:

$$\theta_{j+1} = \theta_j - \alpha \frac{\partial J\left(\theta_j\right)}{\partial \theta_j}$$

where α is the learning rate, which is fine-tuned so that the model could avoid trapping in local minima and achieve convergence. Because transfer learning is used, the training set is not necessary to be very large. To make training data for objective detection in the welding image, 400 images were captured during WAAM process as the training set. The training was implemented on GPU through Google Colab, and each batch had eight images for a single GPU. The training images were resized to 128 pixels × 128 pixels. The Mask R-CNN model was trained for 100 epochs during each training stage. The details of training implementation are listed in Table 1, and

Table 1 Implementation details of training

Image resize dimension	128 × 128	Total epoch	100
Learning rate	0.001	Number of GPUs	1
Learning momentum	0.9	Batch per GPU	8
Weight decay	0.0001	Steps per epoch	100

it includes model parameters like learning rate, weight decay and so on.

After the training, the melt pool area can be detected and segmented with high accuracy. As shown in Fig. 7, it can be found that the melt pool and wire can be detected and segmented well. Furthermore, the width of melt pool can be considered as same as the width of its bounding box. The training results include the image segmentation map and the coordinates of the bounding box. Therefore, the width of melt pool can be obtained directly.

Based on the above Mask R-CNN framework, the width of melt pool during wire arc additive manufacturing can be measured in real time. In order to understand the WAAM process and develop dynamic models for controller design, system identification for the WAAM process was conducted, which will be presented and discussed in detail in the next section.

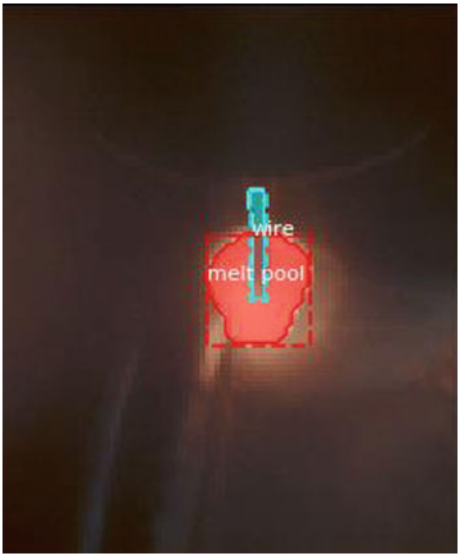

Fig. 7 Example of detection and segmentation in welding image

4 System Identification

In order to implement feedback control or predict the layer geometry, it is essential to understand the process dynamic of WAAM. Based on Mask R-CNN algorithm, the melt pool width can be measured, and the dynamic model could be built, which describes the relationships between melt pool width and process parameters in the time domain.

Neuro-fuzzy algorithm computes the parameters of T-S fuzzy model through the training of neural network, which has been widely applied in extensive area [24, 25]. Jang et al. [28] proposed to apply hybrid learning method in adaptive neuro-fuzzy inference system (ANFIS). This algorithm has the advantages of rule adaption and rapid converging. At the same time, it does not depend on the experiences when building the fuzzy rules. In this section, a data-driven ANFIS model for melt pool dynamic during the WAAM process will be presented. And it will be compared with a linear ARX and nonlinear Hammerstein–Wiener model.

4.1 Pseudo-random Ternary Signal

In order to model the process dynamic of WAAM, dynamic experiments were implemented to model the relationships between wire feed speed and weld pool width. In these experiments, pseudo-random ternary signal responses were studied, which means the WFS varied randomly from 3 to 12 m/min and the fluctuating welding pool width could be obtained. At the same time, the corresponding width could be measured by the Mask R-CNN algorithm proposed above. Figure 8 plots the input

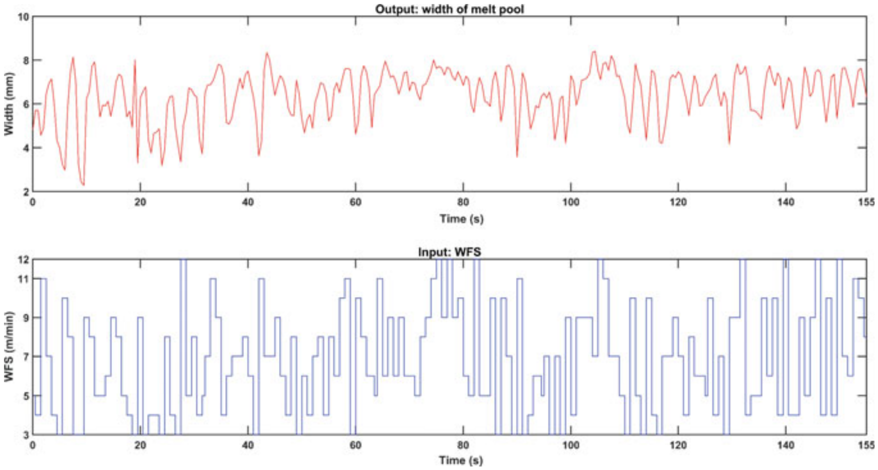

Fig. 8 Response and pseudo-random ternary signal input

and measured the corresponding output. The sampling period in this study is selected to be 0.5 s according to existing literature. [11, 26]

4.2 Dynamic Modelling

The main aim of this section is to obtain a powerful model, which is able to simulate the process dynamic with accept accuracy. The dynamics of WAAM process were modelled in three types of structure, including linear ARX, Hammerstein–Wiener and ANFIS.

Linear ARX model.

Firstly, the process dynamic of WAAM was modelled in linear ARX (autoregressive models with eXogenous variables) form. ARX structure is one of the most widely used linear models in practise due to its simple structure and stable estimation, which can be used as the basis for many methods in process dynamics and control analysis. The structure of ARX could be expressed as Eq. (1):

$$A(z)y(k) = B(\mathrm{z})u(k) + e(k) \tag{1}$$

where $A(z)$ and $B(z)$ are polynomials and can be written as:

$$\begin{aligned} A(z) &= 1 + a_1 z^{-1} + a_2 z^{-2} + \cdots + a_{n_a} z^{-n_a} \\ B(z) &= b_0 + b_1 z^{-1} + b_2 z^{-2} + \cdots + b_{n_b} z^{-n_b} \end{aligned} \tag{2}$$

$a_1 \ldots a_{n_a}$ and $b_1 \ldots b_{n_L}$ are the structural parameters of ARX model, $z - 1$ represents the delay operator, $e(k)$ is the noise. During system identification, the structural parameters of ARX are determined by least squares algorithm. In this study, the ARX model is determined in MATLAB system identification toolbox. The parameters of the identified dynamic model are listed in Table 2.

The estimation performance of the linear ARX model is shown in Fig. 9. Once a model is determined, its performance could be evaluated by the mean square error (MSE), which is defined by Eq. (3). The mean square error (MSE) for the ARX model is 0.339.

$$\mathrm{MSE} = \frac{\sum_{K=1}^{N} (\hat{w}(k) - w(k))^2}{N} \tag{3}$$

Table 2 Structural parameters of ARX model

$a(j), j = 1,\ldots, n_a$	$b(j), j = 1,\ldots, n_b$
[−0.493, −0.000041, 0.162, −0.092, −0.02, −0.046, −0.068, −0.02, −0.104]	[0.166, 0.123]

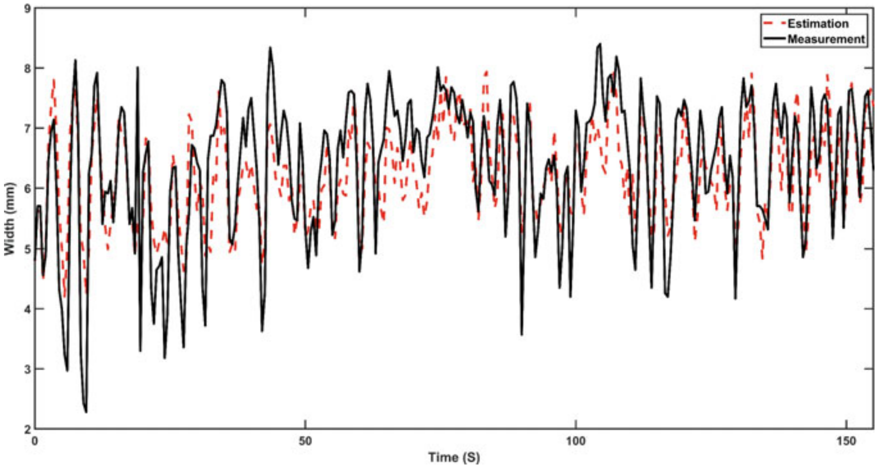

Fig. 9 Linear ARX modelling result

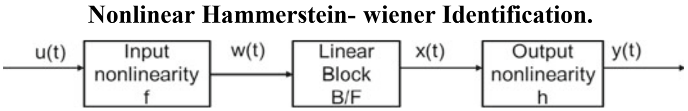
Nonlinear Hammerstein- wiener Identification.
u(t)
Input nonlinearity f
w(t)
Linear Block B/F
x(t)
Output nonlinearity h
y(t)

Fig. 10 Hammerstein–Wiener structure

Nonlinear Hammerstein–Wiener Identification.

A class of popular nonlinear dynamical models consists of linear dynamic blocks and nonlinear memoryless blocks. One typical example is Hammerstein–Wiener model [27]. Figure 10 illustrates the structure of Hammerstein–Wiener model. It includes two static nonlinear blocks and a linear block.

$u(t)$ and $y(t)$ represent the system input and output. Firstly, the input $u(t)$ is transformed by a nonlinear function f, as $w(t) = f(u(t))$. Then, $w(t)$ is transformed by a liner block: $x(t) = (B/F)w(t)$, h block is a nonlinear output function. Equations (4), (5) and (6) are the input nonlinear static function, the linear dynamic subsystem and the output nonlinear static function, respectively.

$$w(t) = f(u(t)) = p_1u(t) + p_2u^2(t) + \cdots + p_mu^m(t) \tag{4}$$

$$\frac{\mathrm{d}x(t)}{\mathrm{d}t} = Ax(t) + Bw(t - T_d) \tag{5}$$

$$z(t) = Cx(t) \tag{6}$$

$$z(t) = g^{-1}(y(t)) = q_1y(t) + q_2y^2(t) + \cdots + q_ry^r(t)$$

T_d is the time delay. The matrices of A, B and C can be expressed in the following forms:

$$A = \begin{bmatrix} 0\,0\,0 & & 0 & -a_n \\ 1\,0\,0 & \cdots & 0 & -a_{n-1} \\ 0\,1\,0 & & 0 & -a_{n-2} \\ \vdots & \ddots & & \vdots \\ 0\,0\,0 & \cdots & 0 & -a_2 \\ 0\,0\,0 & & 1 & -a_1 \end{bmatrix}$$
$$B = \begin{bmatrix} b_n \; b_{n-1} \; b_{n-2} \ldots b_2 \; b_1 \end{bmatrix}^T$$
$$C = \begin{bmatrix} 0\,0\,0 \ldots 0\,1 \end{bmatrix}$$

The main objective of system identification is to estimate A, B, T_d, $p_i(i = 1, 2 \ldots, m)$ and $q_i(i = 1, 2 \ldots, r)$. The identification of Hammerstein–Wiener model was also implemented in MATLAB system identification toolbox. The performance of this predictive model is shown in Fig. 11. The MSE of Hammerstein–Wiener model is 0.2727. Because there are too many structural parameters, they will not be listed in detail.

ANFIS.

The WAAM process involves metal melting, flowing and solidifying, which are inevitably fuzzy and nonlinear. Neuro-fuzzy model combines both advantages of neural network and fuzzy inference. Through training neural network using system input and output data, the parameters for a T-S fuzzy model can be identified. Neuro-fuzzy systems are usually based on Sugeno-type fuzzy model. A T-S fuzzy model has the rules in the following form: [28]

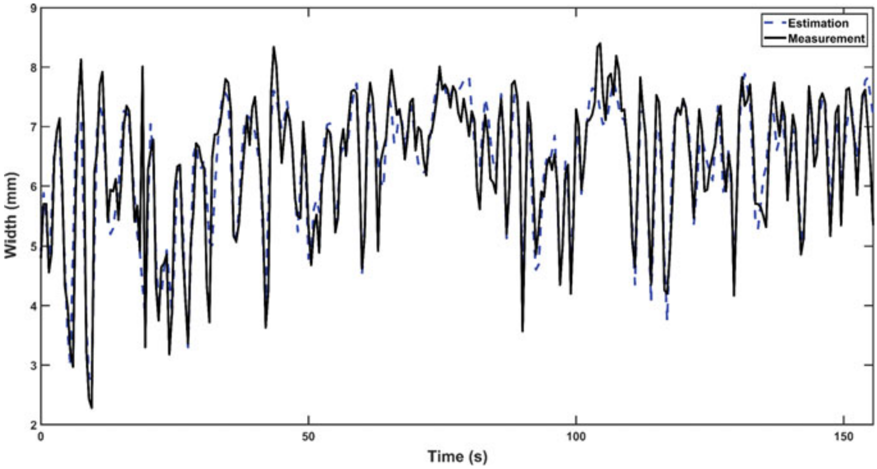

Fig. 11 Hammerstein–Wiener modelling result

R^i: IF x_1 is A_{i1} and x_2 is A_{i2} … and x_n is A_{in},
Then $y_i = a_0 + a_1^i x_1 + \cdots + a_n^i x_n$

where

- $x_1 \ldots x_n$ are the input variables of ANFIS,
- A_i and B_i are the fuzzy sets,
- y_i is the output of ith rule,
- $a_0 \ldots a_n$ are the design parameters, which are determined by the neural network.

Figure 12 illustrates the reasoning mechanism of the Sugeno model with two input and two fuzzy partitions, which is used in ANFIS for inference. The input and output are put into the system for training, and the structural parameters for membership function and Sugeno class function can be obtained. The detail of ANFIS algorithm is described in Table 3.

In this study, we selected $y(k-a)$, $a = 0, 1, 2$ $u(k-b)$, $b = 0, 1, 2$ as the input of ANFIS, and $y(k+1)$ as the output. The modelling result is illustrated in Fig. 13. The RMSE of ANFIS is 0.103.

In order to compare the predictive accuracy of those dynamic models, their MSE are listed in Table 4. It can be observed that the ANFIS model has the smallest MSE among those models. The estimation errors of those three models are plot in Fig. 14. It can be also observed that compared to linear ARX and nonlinear Hammerstein–Wiener, ANFIS model has the best accuracy in describing the dynamic of the WAAM process.

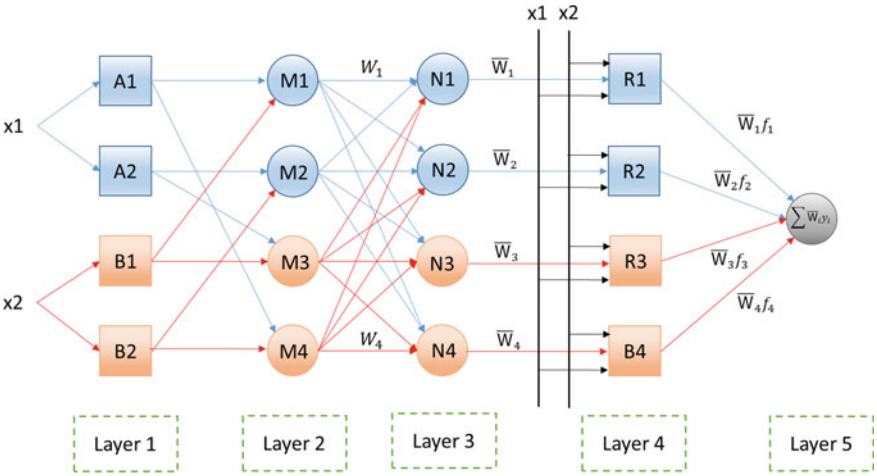
x1 x2
x1
x2
A1
A2
B1
B2
M1
M2
M3
M4
W_1
W_4
N1
N2
N3
N4
$\overline{W}_1$
$\overline{W}_2$
$\overline{W}_3$
$\overline{W}_4$
R1
R2
R3
B4
$\overline{W}_1 f_1$
$\overline{W}_2 f_2$
$\overline{W}_3 f_3$
$\overline{W}_4 f_4$
$\sum \overline{W}_i y_i$
Layer 1
Layer 2
Layer 3
Layer 4
Layer 5

Fig. 12 Structure of ANFIS

Table 3 Detail of ANFIS algorithm

Type		Function	Output
Layer 1	Adaptive	This layer generates fuzzy membership value for inputs, which can be expressed as μ_{Ai} and μ_{Bi}. When generalized bell membership function is used, then: $\mu_{Ai}(x) = \frac{1}{1+\left[\left(\frac{x-c_i}{a_i}\right)^2\right]b_i}$ where a_i, b_i and c_i are the parameters of membership function, known as premise parameters, which adapt during the training process	$\mu_{Ai}(x)$
Layer 2	Fixed	The weights for the output of each rule are calculated in this layer as: $\omega_i = \mu_{Ai} * \mu_{Bi}$	ω_i
Layer 3	Fixed	In this layer, normalized firing strengths are calculated as: $\overline{\omega_i} = \frac{\omega_i}{\sum_1^n \omega_j}$	
Layer 4	Adaptive	'Defuzzification' layer, the second adaptive node, computes output for each rule: $\overline{\omega_i} y_i = \overline{\omega_i}\left(a_0 + a_1^i x_1 + \cdots + a_n^i x_i\right)$ where $a_0 \ldots a_n$ are tuned during the training process to obtain the best match	$\overline{\omega_i} y_i$
Layer 5	Fixed	The output of ANFIS can be expressed as the summation of each rule's output: $y = \sum_1^n \overline{\omega_i} y_i$	y

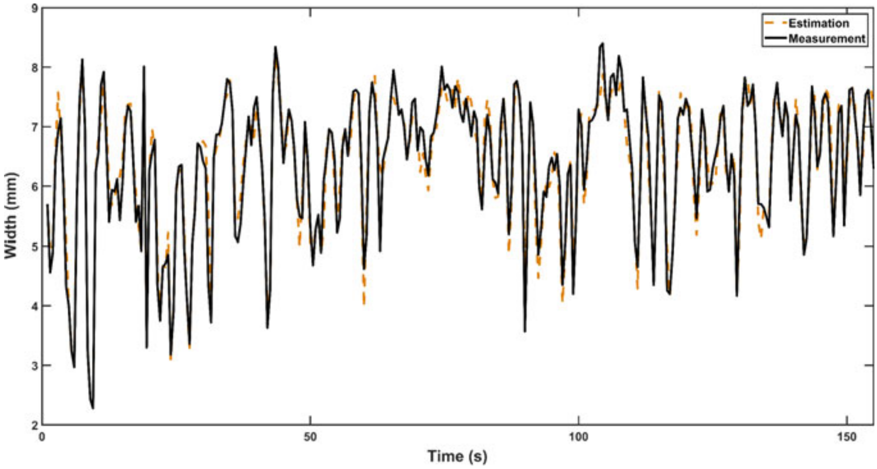

Fig. 13 ANFIS modelling result

Table 4 Estimation accuracy of different model

Model structure	MSE
ARX	0.339
Hammerstein–Wiener	0.273
ANFIS	0.103

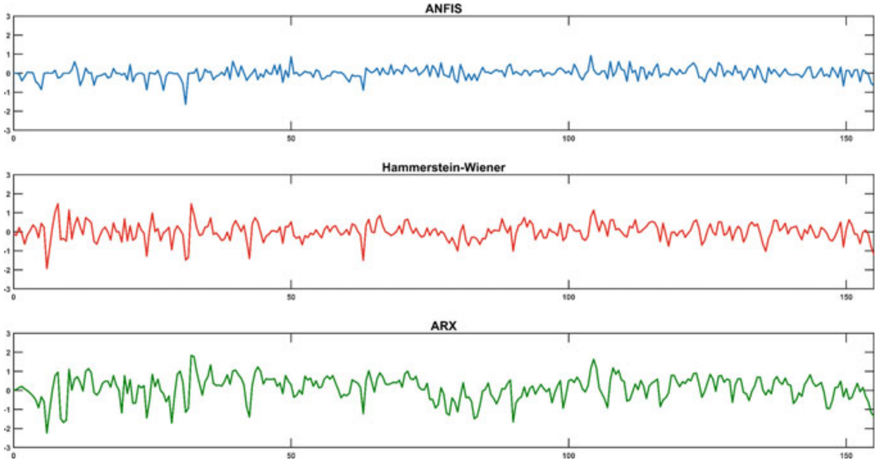

Fig. 14 Estimation error of ANFIS, Hammerstein–Wiener and ARX model

5 Conclusion

This paper shows the potential application of deep learning in automated additive manufacturing and welding inspection. In this study, a passive vision system was developed to monitor the melt pool during wire arc additive manufacturing process. Mask R-CNN was employed to detect and segment the melt pool area, and then the width of melt pool can be obtained. In order to achieve feedback control, system identification for the WAAM process was implemented. Based on experimental data under pseudo-random ternary signal, linear ARX, Hammerstein–Wiener and ANFIS model were built. Validation results demonstrated that the ANFIS model could provide a more accurate estimation to predict the WAAM process.

Acknowledgements The authors gratefully acknowledge the China Scholarship Council for financial support (201704910782), UOW Welding and Industrial Automation Research Centre, the National Natural Science Foundation of China under the Grant No. 61973213, 61873164, and the Shanghai Natural Science Foundation (18ZR1421500).

References

1. Ralph B (1925) Method of making decorative articles. Google Patents
2. Shi J et al (2019) T-GMAW based novel multi-node trajectory planning for fabricating grid stiffened panels: an efficient production technology. J Cleaner Prod: 117919
3. Li F et al (2017) Evaluation and optimization of a hybrid manufacturing process combining wire arc additive manufacturing with milling for the fabrication of stiffened panels. Appl Sci 7(12):1233
4. World's First Class Approved 3d Printed Ship's Propeller Unveiled. Available from: https://www.damen.com/en/news/2017/11/worlds_first_class_approved_3d_printed_ships_propeller_unveiled
5. Müller J et al (2019) Design and parameter identification of wire and arc additively manufactured (WAAM) steel bars for use in construction. Metals 9(7):725
6. Ding D et al (2015) Wire-feed additive manufacturing of metal components: technologies, developments and future interests. Int J Adv Manuf Technol 81(1–4):465–481
7. Xu Y et al (2012) Research on the real-time tracking information of three-dimension welding seam in robotic GTAW process based on composite sensor technology. J Intell Rob Syst 68(2):89–103
8. Fang J, Wang K (2019) Weld pool image segmentation of hump formation based on fuzzy C-means and Chan-Vese model. J Mater Eng Perform 28(7):4467–4476
9. Guo B et al (2016) Weld deviation detection based on wide dynamic range vision sensor in MAG welding process. Int J Adv Manuf Technol 87(9–12):3397–3410
10. Zhan Q et al (2017) A wire deflection detection method based on image processing in wire+arc additive manufacturing. Int J Adv Manuf Technol 89(1–4):755–763
11. Xiong J, Yin Z, Zhang W (2016) Closed-loop control of variable layer width for thin-walled parts in wire and arc additive manufacturing. J Mater Process Technol 233:100–106
12. Krizhevsky A, Sutskever I, Hinton GE (2012) Imagenet classification with deep convolutional neural networks. In: Advances in neural information processing systems
13. He K et al (2016) Deep residual learning for image recognition. In: Proceedings of the IEEE conference on computer vision and pattern recognition
14. Girshick R et al (2014) Rich feature hierarchies for accurate object detection and semantic segmentation. In: Proceedings of the IEEE conference on computer vision and pattern recognition
15. Girshick R (2015) Fast r-cnn. In: Proceedings of the IEEE international conference on computer vision
16. Ren S et al (2015) Faster r-cnn: towards real-time object detection with region proposal networks. In: Advances in neural information processing systems
17. Long J, Shelhamer E, Darrell T (2015) Fully convolutional networks for semantic segmentation. In: Proceedings of the IEEE conference on computer vision and pattern recognition
18. Tsai H-F et al (2019) Usiigaci: Instance-aware cell tracking in stain-free phase contrast microscopy enabled by machine learning. SoftwareX 9:230–237
19. Burke CJ et al (2019) Deblending and classifying astronomical sources with mask R-CNN deep learning. arXiv preprint arXiv:1908.02748
20. He K et al (2017) Mask r-cnn. In: Proceedings of the IEEE international conference on computer vision
21. Lin T-Y et al (2014) Microsoft coco: common objects in context. In: European conference on computer vision, Springer
22. Dutta A, Zisserman A (2019) The VGG image annotator (VIA). arXiv preprint arXiv:1904.10699
23. Kingma DP, Adam BJ (2014) A method for stochastic optimization. arXiv preprint arXiv:1412.6980
24. Hayashi K et al (1995) Neuro fuzzy transmission control for automobile with variable loads. IEEE Trans Control Syst Technol 3(1):49–53

25. Tanaka K, Sano M, Watanabe H (1995) Modeling and control of carbon monoxide concentration using a neuro-fuzzy technique. IEEE Trans Fuzzy Syst 3(3):271–279
26. Liu YK, Zhang YM (2013) Model-based predictive control of weld penetration in gas tungsten arc welding. IEEE Trans Control Syst Technol 22(3):955–966
27. Wills A et al (2013) Identification of Hammerstein–Wiener models. Automatica 49(1):70–81
28. Jang J-S (1993) ANFIS: adaptive-network-based fuzzy inference system. IEEE Trans Syst Man Cybern 23(3):665–685

Research on Fuzzy Comprehensive Evaluation of Seam Quality in Double-Wire Double-Pulsed MIG High-Speed Welding

Huangsheng Xie, Zhihe Fu, Jiaxiang Xue, and Yu Hu

Abstract In this paper, quantitative evaluation method of the welding stability and quality based on current sample entropy and current probability density distribution function were explored. A comprehensive evaluation method of welding quality based on fuzzy logic inference was established, and the method was applied to double wire double pulse. The MIG high-speed welding process stability and weld quality were quantitatively evaluated. The current sample entropy algorithm was used to analyze the effects of twin-wire welding speed, waveform modulation mode, and low frequency on welding stability. From the probability density distribution function, the front and back wire current concentration K was selected as the stability index of double-wire welding. The effects of welding speed, waveform modulation mode, and low frequency on welding stability were studied. Two quantitative indexes of current sample entropy and current concentration were selected to establish a fuzzy logic quantitative evaluation system for double-wire high-speed welding seam quality. The test results show that the correctness rate of the fuzzy logical comprehensive assessment is 85.7%, and the evaluation results obtained by the fuzzy logic inference evaluation system are close to the evaluation results by the experts.

Keywords Double wire · Double pulse · High-speed welding · Low-frequency modulation · Current sample entropy · Fuzzy evaluation

---

H. Xie · Z. Fu
Department of Mechanical and Electrical Engineering, Longyan University, Longyan 364012, China

J. Xue (✉) · Y. Hu
School of Mechanical and Automotive Engineering, South China University of Technology, Guangzhou 510641, China
e-mail: mejiaxue@scut.edu.cn

© Springer Nature Singapore Pte Ltd. 2020

S. Chen et al. (eds.), *Transactions on Intelligent Welding Manufacturing*,
Transactions on Intelligent Welding Manufacturing,
https://doi.org/10.1007/978-981-15-7215-9_5

1 Introduction

The evaluation and judgment of the welding quality of the traditional double-wire high-speed welding is still based on the appearance of the weld appearance. For example, it can be judged whether there are hump, undercut, crack, unwedded by the weld profile. Welding defects are penetration, infusion, and porosity [1–3]. The quality of the weld can directly reflect the stability of the welding process. In the evaluation of weld quality, it is generally based on the criteria of "good" [4–7]. If only relying on the experience of welding technicians, there will be problems of non-uniformity of standards, and the lack of quantitative evaluation standards will bring difficulties in control method research and process performance selection.

At present, the evaluation of welding quality at home and abroad is in the stage of continuous exploration, and some related research has been carried out [8–17]. Li [8] extracted the feature information related to GMAW-P droplets and established a related droplet regression model based on statistical analysis. The model can be used to predict the droplet transfer process accurately. Fang [9] uses high-speed video system and memory oscilloscope to synchronously collect real-time variable polarity argon arc welding current and arc shape information, and compare and analyze five parameters such as welding current frequency, DC electrode connection time, and DC electrode connection time. Literature is on the effects of arc morphology and weld quality. Wang et al. [10, 11] used artificial intelligence to extract welding-related feature information and based on this established a dynamic characteristics evaluation system for CO_2 arc welding power source. Hermans et al. [12] calculated the relationship between the short-circuit frequency and the stability of the welding process by electrical signal statistics and confirmed that the process stability is directly related to the weld pool oscillation. Zhang et al. [13] extracted the current waveform characteristic information and obtained the wavelet analysis method to effectively evaluate the dynamic characteristics of the power supply process. Quinn et al. [14] proposed a method for detecting automatic constant pressure gas-shielded welding defects using current and voltage signals. A defect detection algorithm was established by current and voltage signals to evaluate weld quality. Shi et al. [15] proposed the stability of aluminum alloy pulsed MIG welding by statistical voltage probability density based on the arc voltage probability density distribution function. Xue et al. [16] used the short-circuit time, arcing time, and cycle time of CO_2 welding process as the statistical analysis for statistical analysis and quantitatively evaluated the stability of twin-wire pulse welding through probability density distribution map. Wang et al. [17] collected the current and voltage waveforms of the two arcs during the welding process. The current histogram was used to compare the stability of the two arcs. The relationship between the electrical signal and the stability of the CO_2 gas-shielded flux-cored wire was analyzed.

According to the above discussion, most of the current welding performance evaluation is mainly based on the qualitative analysis of electrical signals, and the electrical signal quantitative evaluation method is less used in the evaluation process. Accurate evaluation of welding performance has become the focus of research in this area with the increasing intelligence of welding power sources. In actual welding, it is difficult to evaluate the welding quality due to the influence of welding-related factors.

In summary, this paper is mainly from the stability of the electrical signal of the welding process combined with the appearance of the weld to the comprehensive evaluation of welding quality. According to the actual application results, the stability of the electrical signal has an important influence on the welding process performance. The electrical signal involves the parameters is related to the welding quality.

2 Stability Analysis of High-Speed Welding Electric Signal Based on Sample Entropy

2.1 Electrical Signal Stability Sample Entropy Evaluation Index

The concept of approximate entropy (ApEn) was introduced into the study of the stability of welding processes [18]. Due to the influence of data length and embedding dimension, the sample entropy (SaEn) algorithm is simplified from the approximate entropy method. The sample entropy does not need to take into account the matching value, and the corresponding calculation accuracy reaches a higher level. The sample entropy algorithm process is as follows.

The original calculated data is a sequence, N is the number, and m is the number of dimensions.

(1) Reconstruct a set of m-dimensional vectors by sequence number:

$$X_m(i) = [u(i), u(i+1), \ldots, u(i+m-1)] \quad (i = 1, 2, \ldots, N-m+1) \tag{1}$$

(2) Define the distance between and the greater of the difference between the two:

$$d[X_m(i), X_m(j)] = \max_{0<k<m-1}(|u(i+k) - u(j+k)|) \quad j \neq i \tag{2}$$

(3) For each $i(1 < i < N-m)$, the number of $d[X_m(i), X_m(j)]$ less than the given threshold r is counted to determine the ratio of its sum to $N - m$:

$$B_r^m(i) = N^m(i)/(N-m) \tag{3}$$

(4) Average value of $B_r^m(i)$:

$$B^m(i) = \frac{\sum_{i=1}^{N-m} B_r^m(i)}{N-m+1} \tag{4}$$

(5) Dimension plus 1 to determine the high-dimensional vector:

$$X_{m+1}(i) = [u(i), u(i+1), \ldots, u(i+m)] \quad (i = 1, 2, \ldots, N-m) \tag{5}$$

(6) Repeat the previous three steps to find the new vector:

$$B_r^{m+1}(i) = N^m(i)/(N-m-1) \tag{6}$$

$$B^{m+1}(r) = \frac{\sum_{i=1}^{N-m} B_r^{m+1}(i)}{N-m} \tag{7}$$

(7) The theoretical entropy of the sequence is:

$$\mathrm{SaEn}(m, r, N) = \lim\left\{-\mathrm{In}\left[B^{m+1}(r)/B^m(r)\right]\right\} \tag{8}$$

If N is a finite value, it can be expressed as:

$$\mathrm{SaEn}(m, r, N) = -\mathrm{In}\left[B^{m+1}(r)/B^m(r)\right] \tag{9}$$

The dimension m, the similar tolerance r, and the sample length N are three parameters that need to be determined for the sample entropy calculation. In the sample entropy calculation, the greater the complexity of the original data sequence, the larger the sample entropy [19]. To this end, the sample entropy is used to discuss the parameters in the current signal, according to the sample entropy standard value given in (10), and the current signal stability level is judged based on the following sample entropy standard deviation index.

$$S = \sqrt{\frac{\sum_{i=1}^{n} (x_i - \bar{x})^2}{n-1}} \tag{10}$$

In order to qualitatively analyze the influence of process parameters on sample entropy, the orthogonal test of double-wire pulse high-speed welding was carried out with the welding speed, low-frequency frequency and waveform modulation as the factors. The orthogonal test design scheme and results are shown in Table 1.

The results of the range analysis are shown in Table 2. From the results, the welding speed has the greatest influence on the result, and the extreme difference reaches 0.508. The waveform modulation method has a great influence on the result, the extreme difference is 0.116, and the low frequency is 0.024, which has little effect on the result.

Table 1 Weld appearance of scientific fuzzy comprehensive evaluation

Sample	Weld surface forming
1#	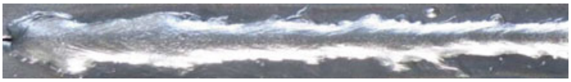
2#	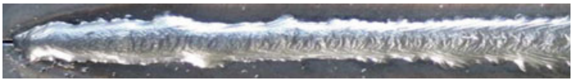
3#	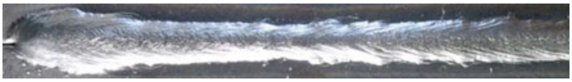
4#	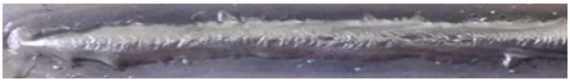
5#	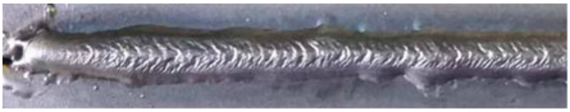
6#	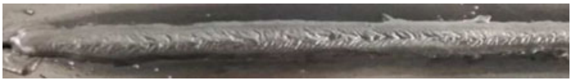
7#	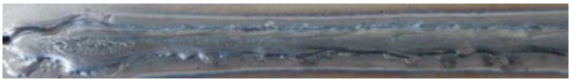
8#	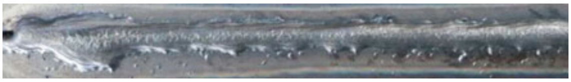
9#	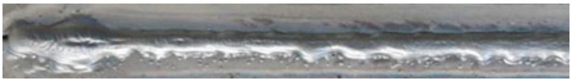

Table 2 Characteristic values of scientific fuzzy comprehensive evaluation

Sample	Front wire current concentration	Rear wire current concentration	Sample entropy of the front wire CSaEn1	Sample entropy of the rear wire CSaEn2
1#	0.328	0.335	0.0198	0.0189
2#	0.321	0.332	0.0159	0.0146
3#	0.34	0.361	0.0136	0.0111
4#	0.289	0.321	0.0259	0.026
5#	0.342	0.358	0.0196	0.0223
6#	0.338	0.337	0.0211	0.0217
7#	0.235	0.24	0.0309	0.0323
8#	0.245	0.246	0.0297	0.0293
9#	0.252	0.263	0.027	0.0267

2.2 Two-Wire High-Speed Welding Electric Signal Sample Entropy Evaluation Test

The double-wire welding electric signal is composed of two signals. The two current pulse parameters can be the same or different. Therefore, when evaluating the stability, it is necessary to comprehensively consider the influence of the two wires and two signals on the result. The instability of any one of the two-wire arc welding affects the process performance. In the assessment, it is necessary to integrate the influence of the two signals on the results and set the sample entropy evaluation index of the welding process, such as sample entropy (SaEn) and current sample entropy (CSaEn). In calculating the mean, in order to remove the singularity existing in the sample entropy value, the sample entropy of each signal is subtracted from the maximum and minimum values of the sampled value and then averaged, as shown in Eq. (11).

$$\mathrm{SaEn} = \frac{\sum_{i=1}^{n} \mathrm{SampEn} - \max[\mathrm{SampEn}] - \min[\mathrm{SampEn}]}{n-2} \tag{11}$$

Equation (12) shows the single-path stability evaluation index of CSaEn and SD (SaEn) which is the standard deviation of sample entropy in twin-wire welding. In Eq. (13), TCSaEn is the entropy index of the double-wire welding sample. CSaEn is taken as the larger of the two signals in the double-wire welding to characterize the stability of the welding process.

$$\mathrm{SaEn} = \mathrm{SaEn} \times \mathrm{SD}(\mathrm{SaEn}) \tag{12}$$

$$\mathrm{TCSaEn} \; = \max(\mathrm{CSaEn}1, \mathrm{CSaEn}\ 2) \tag{13}$$

Now select nine double-wire welding current signals with different parameters and different stability, as shown in Fig. 1.

In the double-wire single-pulse MIG welding test, the peak current of the front and rear wire pulse is 440 A and the base current is 120 A. In the double-wire double-pulse MIG welding test, the welding parameters are strong pulse peak current 390 A, base current 180 A, and weak pulse. The peak current is 390 A and the base current is 120 A. In the double-wire trapezoidal wave pulse MIG welding test, the welding parameters are 390 A for the peak current of the strong and weak pulse, the base current is 180 A, and the base current is 120 A. It can be seen from Fig. 1 that the amplitudes of the current waveform currents of the nine groups of tests did not show

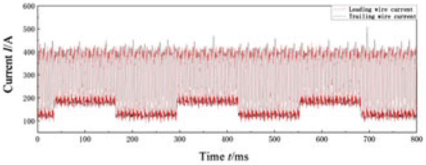

(a) 1# test

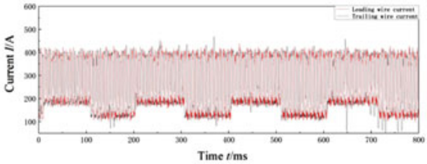

(e) 5# test

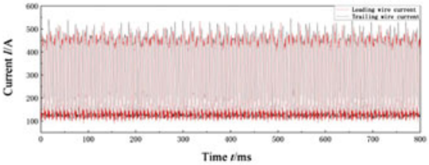

(b) 2# test

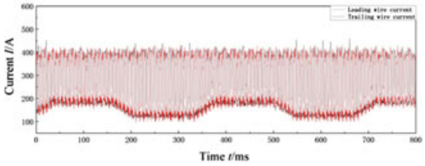

(f) 6# test

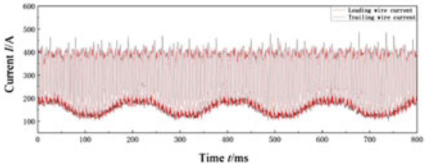

(c) 3# test

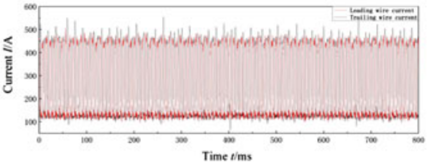

(g) 7# test

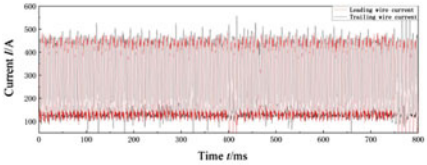

(d) 4# test

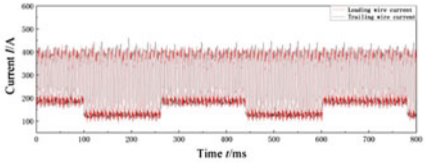

(h) 8# test

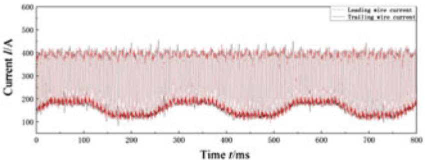

(i) 9# test

Fig. 1 Twin-wire current signal

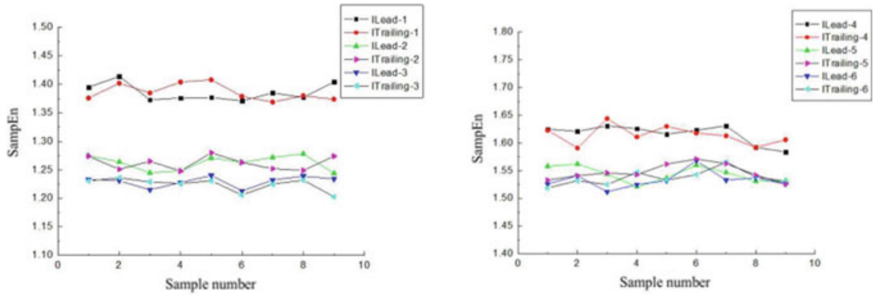

(a) The current sample entropy of double wire of test1#、2#、3#

(b) The current sample entropy of double wire of test 4#、5#、6#

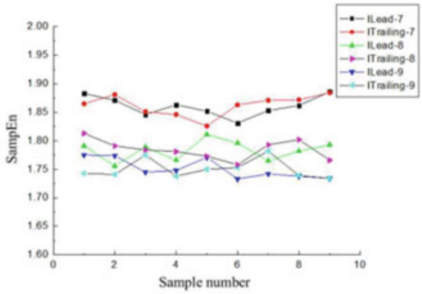

(c) The current sample entropy of double wire of test 7#、8#、9#

Fig. 2 Comparison of sample entropy of two-wire current signal

any significant changes, showing good consistency, and the current amplitudes of the tests 1#, 4#, and 7# were changed more than others. The change in current amplitude of the group test was slightly larger.

The sample entropy comparison of the two-wire current signal is shown in Fig. 2. In the figure, ILead and ITrailing represent the leading wire of the signal and the follower wire current signal. As can be seen from the figure, in general, the sample entropy of the two-wire current signal of 1#, 2#, and 3# is less than the sample entropy of the test 4#, 5#, and 6# twin wires, and the test 4#, 5#, 6# The sample entropy of the two-wire current signal is smaller than the sample entropy of the test 7#, 8#, and 9# twin wires, which indicates that the current signal stability of the test 1#, 2#, and 3# is better than that of the test 4#, 5#, and 6#,7#,8#,9# current signal stability. 1# test current signal sample entropy ratio 2# test, 3# test is large, indicating that the stability of 1# test welding current signal is worse than the stability of the current signal of 2# and 3# test. Similarly, the 4# test current signal sample entropy is larger than the 5# test and the 6# test, and the 7# test current signal sample entropy is larger than the 8# test and the 9# test. The test sample entropy calculation results are shown in Table 3. In the table, CSaEn is the current signal sample entropy, which is the sample entropy of the two-wire current signal. The size can accurately reflect the

Table 3 Evaluation result of scientific fuzzy comprehensive evaluation

Sample	Ma	Mb	Mc	Md	Me	Mf	Single fuzzy evaluation results	Synthesize fuzzy evaluation results	Actual welding effect	Fitting
Front wire 1#	0	0.44	0.56	0.04	0.96	0	B	B	B	√
Rear wire 1#	0	0.3	0.7	0.22	0.78	0	B			
Front wire 2#	0	0.58	0.42	0.82	0.18	0	B	B	B	√
Rear wire 2#	0	0.36	0.64	1	0	0	A			
Front wire 3#	0	0.2	0.8	1	0	0	A	A	A	√
Rear wire 3#	0	0	1	1	0	0	A			
Front wire 4#	0	1	0	0	0.89	0.18	C	C	C	√
Rear wire 4#	0	0.58	0.42	0	1	0	C			
Front wire 5#	0	0.16	0.84	0.08	0.92	0	B	B	C	×
Rear wire 5#	0	0	1	0	1	0	B			
Front wire 6#	0	0.24	0.76	0	1	0	B	B	B	√
Rear wire 6#	0	0.26	0.74	0	1	0	B			
Front wire 7#	0.3	0.7	0.33	0	0	1	D	D	D	√
Rear wire 7#	0.2	0.8	0	0	0	1	D			
Front wire 8#	0.1	0.9	0	0	0.06	0.94	D	D	D	√
Rear wire 8#	0.08	0.92	0	0	0.14	0.86	D			
Front wire 9#	0	1	0	0	0.66	0.34	C	C	C	√
Rear wire 9#	0	1	0	0	0.6	0.4	C			

stability of the welding electrical signal. As can be seen from Table 3, the welding current of no. 3, the stability of the signal, is best.

In summary, the design evaluation index comprehensively considers the influence of various current signals on the sample entropy in the double-wire pulse MIG welding. The current sample entropy can reflect the stability of the welding process, which can be regarded as the performance evaluation of the twin-wire pulse welding process.

2.3 Stability Analysis of High-Speed Welding Based on Probability Density Double Wire

Two-wire High-speed Welding Stability Probability Density Evaluation Index. For the distribution function $F_X(x)$ of any random variable X, the probability density function $f_X(x)$ satisfies:

$$F_X(a) = \int_{-\infty}^{a} f_X(x)\mathrm{d}x \quad \forall - \infty < a < \infty \tag{14}$$

$$\int_{-\infty}^{\infty} f_X(x)\mathrm{d}x = 1 \tag{15}$$

$$P[a < X < b] = F_X(b) - F_X(a) = \int_{a}^{b} f_X(x)\mathrm{d}x \quad \forall - \infty < a < b < \infty \tag{16}$$

If is $f_X(x)$ continuous at a point x, the following relationship exists:

$$f_X(x) = \lim_{x \to 0^+} \frac{F(x + \Delta x) - F(x)}{\Delta x} = \lim_{x \to 0^-} \frac{P\{x < X \le x + \Delta x\}}{\Delta x} \tag{17}$$

$$P\{x < X \le x + \Delta x\} \approx f(x)\Delta x \tag{18}$$

The above equation reflects the probability that the variable appears in the neighborhood of a certain point X.

Introduce the first evaluation index peak current concentration $K1$, the larger the $K1$, the better.

$$K1 = \sum_{j=i_1-n}^{i_1-n} P\mathrm{max}_1(j) + \sum_{j=i_2-n}^{i_1-n} P\mathrm{max}_2(j) \tag{19}$$

The smaller the probability that the current signal is between the peak and the base current, the more stable the current signal and the better the dynamic characteristics of the system. Therefore, this paper designs a second evaluation index $K2$ of the welding current signal, and $K2$ represents the sum of the probabilities of the currents in the area surrounded by the two current peaks.

$$K2 = \sum_{j=l_5}^{l_6} P(j) \tag{20}$$

The probability density-based stability quantization index is represented by the current concentration K, and the larger the K value, the more stable the current signal. Specifically, it is represented by the formula (21).

$$K = K1 - K2 = \sum_{j=i_1-n}^{i_1+n} P_{\max 1}(j) + \sum_{j=i_2-n}^{i_1+n} P_{\max 2}(j) - \sum_{j=l_5}^{l_6} P(j) \tag{21}$$

Double-Wire High-Speed Welding Probability Density Evaluation Test
Figure 3 is the current probability density curve of the nine signals in Table 1, using the current concentration K index to calculate the nine signals in Fig. 3, where $n = 20$, the current signal removes the arcing and arcing segments and selects the first. The calculation is performed from 5000 to 45,000 data points. The calculation results are shown in Table 4. The current concentration K value of the signal 3 in Table 4 is the largest, and the performance is also the most stable; the current concentration K value of the signal 9 is the smallest, which is manifested as unstable welding.

Table 4 The quantitative assessment of probability density distribution

Number	*ILead-1*	*ITrailing-1*	*ILead-2*	*ITrailing-2*	*ILead-3*	*ITrailing-3*
K_1	0.359	0.366	0.359	0.37	0.379	0.399
K_2	0.031	0.031	0.039	0.038	0.039	0.038
K	0.328	0.335	0.32	0.332	0.34	0.361
Number	*ILead-4*	*ITrailing-4*	*ILead-5*	*ITrailing-5*	*ILead-6*	*ITrailing-6*
K_1	0.324	0.355	0.381	0.394	0.377	0.371
K_2	0.035	0.034	0.039	0.036	0.039	0.034
K	0.289	0.321	0.342	0.358	0.338	0.337
Number	*ILead-7*	*ITrailing-7*	*ILead-8*	*ITrailing-8*	*ILead-9*	*ITrailing-9*
K_1	0.266	0.277	0.284	0.279	0.288	0.295
K_2	0.031	0.037	0.039	0.033	0.036	0.032
K	0.235	0.24	0.245	0.246	0.252	0.263

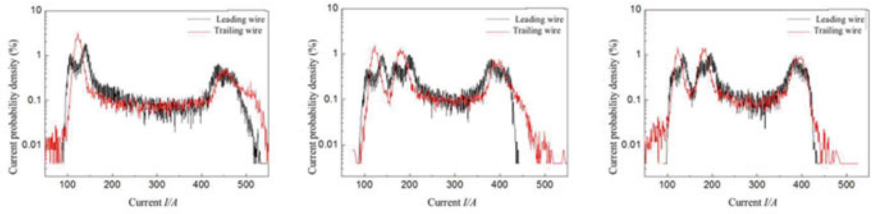

(a) Test 1 # (b) Test 2# (c) Test 3#

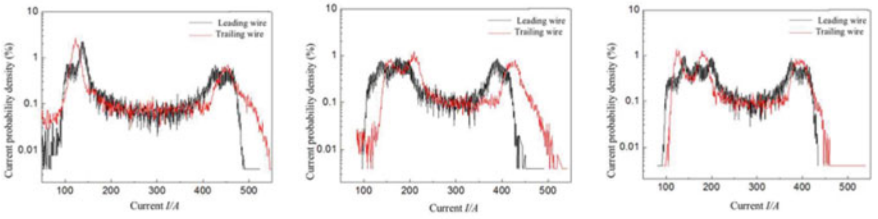

(d) Test 4# (e) Test 5# (f) Test 6#

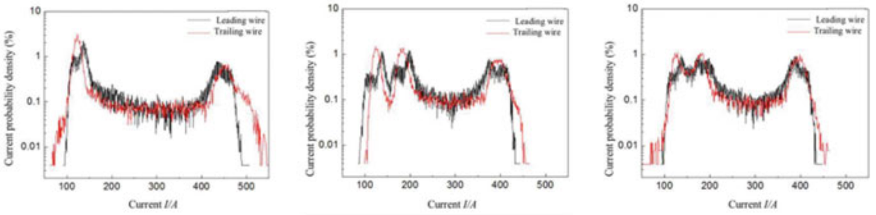

(g) Test 7# (h) Test 8# (i) Test 9#

Fig. 3 Current probability density distribution

2.4 Fuzzy Evaluation of the Quality of Double-Wire High-Speed Welding

According to the experience of weld quality assessment, most relevant qualitative assessment indicators and evaluation results are easily affected by subjective factors, reducing the objectivity of evaluation [20]. According to the professional domain knowledge and expert experience, the fuzzy inference rules are determined. After defuzzification, the accurate numerical evaluation index can be given. Therefore, the fuzzy logic can be used to quantitatively analyze the stability of the welding process. In this paper, a comprehensive evaluation model based on fuzzy inference is established. Through the evaluation and analysis of welding quality, the related factors such as reference current concentration K and current sample entropy CSaEn are integrated in the evaluation process, and the corresponding membership function is determined based on expert experience. Comprehensive analysis obtains relevant fuzzy logic inference rules and performs fuzzy evaluation.

Fuzzy Evaluation Model for Double-Wire High-Speed Welding Seam Quality Some characteristic attributes of things have ambiguity, and it is difficult to give quantitative results for such things. They can only be evaluated with different degrees by means of fuzzy language [21]. In this paper, the fuzzy algorithm is used to evaluate the weld quality. The actual welding effect is divided into five grades: A, B, C, D, and E. In the case of unsustainable welding, arcing occurs, or obvious splashing occurs, and the weld is unevenly formed, and it can be classified into Class E. If the welding can be carried out smoothly, there is obvious splash and stability during welding. If the properties and formability are not good, they are classified into Class D; the welding process can be carried out smoothly, but the welding process is not stable, and the splash is large, and the surface quality of the welding is not very good, then it is classified into C grade; if the corresponding welding stability is high, and no obvious splash is found, if the weld is well formed, it can be classified as Class B; the welding process is stable, almost no splash occurs, and the surface quality of the welding is high. The welding surface of the seam is smooth, dense, and has fish scales and ripples, which are classified as Class A.

According to the actual experience, the membership function of each feature information is established as follows. According to experience, considering the research needs of this paper, the trapezoidal membership function is chosen [22]. The two quantitative evaluation indexes of welding quality are analyzed: current concentration K and current sample entropy CSaEn. The values of these two indicators can be determined based on the correlation function, and the welding quality is evaluated to give quantitative evaluation results.

In the analysis process, the fuzzy subset set by the current concentration K is {Ma, Mb, Mc}, meaning "small," "medium," "large," and the membership function is shown in Fig. 4.

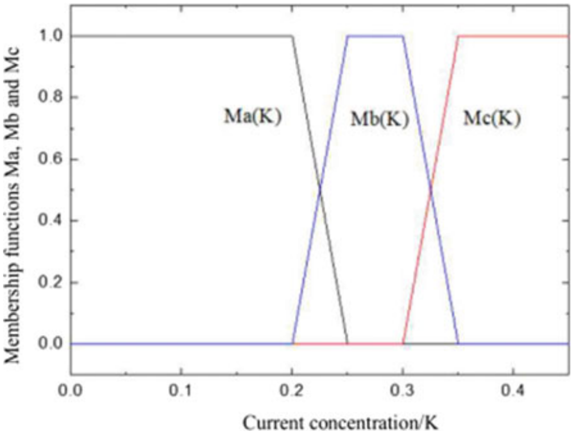

Fig. 4 Membership function of $M(K)$

For the current sample entropy CSaEn, the set is {Md, Me, Mf}, that is, the fluctuation is small, medium, and large.

Double-Wire High-Speed Welding Fuzzy Logic Inference Rules

According to experience, A-E is selected in the analysis process to represent the welding-related fuzzy subset, and the welding level can determine a certain number of inference rules [23].

The best welding quality is Class A, and then the corresponding inference rules are determined based on relevant experience, as follows:

if U(K) is Mc and U(CSaEn) is Md, then W is A;

The high quality is grade B, based on the same experience, and the following inference rules are given:

if U(K) is Mc and U(CSaEn) is Me, then W is B;
if U(K) is Mb and U(CSaEn) is Md, then W is B;

The moderate is Class C. Based on actual experience, the following inference rules are determined:

if U(K) is Mb and U(CSaEn) is Me, then W is C;

The quality is poor, D grade, and there is a short-circuit splash; according to this, actual experience can be summarized as the following inference rules:

if U(K) is Mb and U(CSaEn) is Mf, then W is D;
if U(K) is Ma and U(CSaEn) is Me, then W is D;

The quality is very poor of E grade. In this case, there is obvious arc breaking, welding is not continuous, and obvious splashing occurs during the welding process. The poor weld determines the relevant inference rules.

Details as follows:

if U(K) is Ma and U(CSaEn) is Mf, then W is E;

A total of five inference rules were obtained for each weld quality level, as follows:

For each welding process, according to the current concentration K and the current sample entropy (CSaEn), then based on the different membership functions to determine the relevant membership degree, according to the rules to be assigned to the corresponding level, and then on this basis, fuzzy logic reasoning is performed on the basis, and then the quality of the weld is quantitatively evaluated based on this result. In order to evaluate the effectiveness of such a system during the research process, it can be properly verified.

Analysis of Fuzzy Evaluation Results of Double-Wire High-Speed Welding Seam Quality

Based on the welding speed, low frequency, and waveform modulation method, the orthogonal test of double-wire pulse high-speed welding was carried out to complete nine welds of different quality. The welds obtained in the test are shown in Table 2.

And the parameters are taken to determine the corresponding welds corresponding to *K* and CSaEn. The characteristic quantities of the fuzzy logic comprehensive quantitative assessment are shown in Table 3.

In order to verify the correctness of the fuzzy logic reasoning evaluation results, we observed the actual welding results under the nine process conditions. The welding tests of these nine groups can be completed smoothly. There is no arc breakage in the weld seam, and there are no defects such as cracks. The weld appearance is shown in Table 1. From the results of the weld picture, it can be seen that the 3# test welding process has high stability, the weld is flat and uniform, and the fish scale-like weld bead can be observed on the surface. The weld quality is the best, according to actual experience. Classify its dynamic characteristics into level A. The weld surface formed by 1#, 2#, 6# test is relatively smooth, the weld bead scale is more obvious, but the weld bead edge is less flat, and the weld bead shape is slightly inferior to the 3# test. According to actual experience, The dynamic characteristics are classified into grade B; the surface of the test welds of 4#, 5#, and 9# is not very smooth, and it is slightly worse than the test of 1#, 2#, and 6#. According to actual experience, the dynamic characteristics can be classified into grade C, 7#, 8# test. Although the weld can be continuous, there are obvious curved weld bead, the surface fish scales are not obvious, and according to actual experience, the dynamic characteristics can be classified into grade D. The evaluation results obtained by the fuzzy logic comprehensive quantitative assessment system are shown in Table 3. The comprehensive fuzzy evaluation results of the two-wire welding current characterization information are determined by the poor results of the double-wire single-channel signal fuzzy evaluation results. It can be seen from the table that the correct rate of the system evaluation results is 85.7%, and the evaluation based on the actual welding results is consistent with the results obtained by the fuzzy logic inference evaluation system. However, it is further known that errors have also occurred in this judgment process, and such errors are mainly related to CSaEn's vulnerability to fluctuations in welding parameters, which may cause system failure in the case of large fluctuations.

3 Conclusion

(1) The sample entropy algorithm was used to compare the influence of various parameters of electric signal on the stability of sample entropy. The designed two-wire current sample entropy evaluation index takes into account the current signal pair sample in the double-wire pulse MIG welding process. The influence of entropy, which can reflect the stability during the welding process, can be used as one of the indicators of the performance evaluation model of twin-wire pulse welding.

(2) Based on the sample entropy algorithm, the current concentration degree *K* was taken as the stability quantization parameter, and the influence of the probability

density distribution function on the welding stability was analyzed. The stability evaluation index suitable for double-wire welding was designed.

(3) Welding quality evaluation model based on fuzzy reasoning was designed, and the fuzzy evaluation model result was used as one of the stability evaluation indexes of double-wire welding. The correct rate of the comprehensive fuzzy evaluation is 85.7%, and the evaluation of the actual welding effect is consistent with the results obtained by the fuzzy logic inference evaluation system.

Acknowledgements This research was funded by the National Natural Science Foundation of China (51875213), The High-level Leading Talent Introduction Program of GDAS (2016-GDASRC-0106), Natural Science Foundation of Fujian (2018J01503), Longyan Science and Technology Project (2017LY68).

References

1. Pei Y, Shan J, Ren J (2012) Study of humping tendency and affecting factors in high speed laser welding of stainless steel sheet. Jinshu Xuebao/Acta Metall Sinica 48:1431–1436. https://doi.org/10.3724/SP.J.1037.2012.00416
2. Kiran DV, Basu B, De A (2012) Influence of process variables on weld bead quality in two wire tandem submerged arc welding of HSLA steel. J Meterials Process Technol 212:2041–2050
3. Shi Y, He W, Zhu M et al (2014) Detection and analysis of influence of shield gas on melt drop metal transfer behavior in consumable double-wire bypass coupled GMAW arc. J Lanzhou Univ Technol 40(5):19–22
4. Devakumaran K, Rajasekaran N, Ghosh PK (2012) Process characteristics of inverter type GMAW power source under static and dynamic operating conditions. Mater Manuf Process 27(12):1450–1456
5. Li ZY, Srivatsan TS, Zhao HZ et al (2011) On the use of arc radiation to detect the quality of gas metal arc welds. Mater Manuf Process 26(7):933–941
6. Liu A, Tang X, Lu F (2013) Arc profile characteristics of Al alloy in double-pulsed GMAW. Int J Adv Manuf Technol 65(1–4):1–7
7. Saini D, Floyd S (2014) An investigation of gas metal arc welding sound signature for on-line quality control. Int J Emerg Electr Power Syst 77(3):172–179
8. Li F, Hua X, Wang W, Wu Y (2009) Modeling of droplet transfer electrical characteristics in pulsed gas melted arc welding. Hanjie Xuebao/Trans China Weld Inst 30:97–100
9. Fang C, Yu J, Chen S, Song Y (2007) Effects of VPTIG welding current parameters on arc shape and weld quality. Hanjie Xuebao/Trans China Weld Inst 28:21–25
10. Wang Z, Xue J, Wang F (2007) Dynamic character analysis for the arc welding power source based-on fuzzy logic. China Weld(English Edition) 16:1–6
11. Wang Z, Xue J, Dong F et al (2007) An analysis of the dynamic resistance and the instantaneous energy of the CO_2 arc welding process. China Weld 16(1):77–82
12. Hermans MJM, Ouden GD (1999) Process behavior and stability in short circuit gas metal arc welding. Weld J 78(4):137–141
13. Zhang X, Li J, Li H, Yang L, Huang S (2002) Evaluation of technologic dynamic characteristic of CO_2 arc welding power source basing on wavelet analysis. Jixie Gongcheng Xuebao/Chin J Mech Eng 38:112–116
14. Quinn TP, Smith C, Mccowan C et al (1999) Arc sensing for defects in constant-voltage gas metal arc welding. Weld J 78(9):323–328

15. Shi Y, Nie J, Huang J, Lu L, Fan D (2010) Evaluation method of pulsed MIG welding of aluminum alloy based on probability density of arc voltage signal. Hanjie Xuebao/Trans China Weld Inst 31:13–16
16. Xue J, Jia L, Yi Z (2003) Statistical analysis for the electrical signal of CO_2 welding process. Huanan Ligong Daxue Xuebao/J South China Univ Technol (Natural Science). 31, 37–37
17. Wang F, Hua X, Ma X, Wu Y (2010) Stability analysis of electrical signal in O_2 flux-cored double wire GMAW. Shanghai Jiaotong Daxue Xuebao/J Shanghai Jiaotong Univ 44:457–462
18. Chen H (2017) Study on the technology and process of high speed welding with sine wave modulated pulse MIG. South China University of Technology, Guangzhou
19. Tianfa L (2016) Double pulse MIG waveform modulation method in aluminum alloy and mechanism research. South China University of Technology, Guangzhou
20. Na L, Gu F, Xu YL et al (2017) Real-time monitoring of welding path in pulse metal-inert gas robotic welding using a dual-microphone array. Int J Adv Manuf Technol 90:2955–2968
21. Ou YH, Song YL (2007) Weld location extraction in radiographic images using fuzzy rules generating method. Sci Technol Weld Join 12(1):63–66
22. Naso D, Turchiano B, Pantaleo P (2005) A fuzzy logic based optical sensor for online weld defect detection. IEEE Trans Industr Inf 1(4):259–273
23. Xue J, Zhang X, Huang S (2000) Evaluation of dynamic characteristic of CO_2 arc welding power source by fuzzy logic inference. Huanan Ligong Daxue Xuebao/J South China Univ Technol (Natural Science) 28:4–9

Welding Deviation Extraction during K-TIG Welding Based on K-Means Clustering

Baori Zhang and Yonghua Shi

Abstract During K-TIG welding, due to the strong arc and the narrow seam, it is difficult to accurately identify the deviation of the welding, which would affect the K-TIG automatic welding. In this paper, a novel welding deviation visual inspection method is proposed. A high dynamic range camera is used to capture the welding images. Then, K-means-based image segmentation algorithm is used to automatically divide an image into arc region and seam area. An optimal path method is proposed to extract the feature points on the electrodes from the arc region image and get the position of the electrode tip points. The seam area is processed by a refinement algorithm to obtain the weld position, and finally, the deviation between the electrode tip and the seam is obtained. The experiment proves that the proposed algorithm can realize the automatic identification of K-TIG welding deviation.

Keywords Keyhole deep penetration · TIG welding · Seam deviation detection · Optimal path algorithm

1 Introduction

With the development of welding automation technology, the detection technology of the welding process becomes popular. There are signals used to observe the welding process including electrical signals, acoustic signals, thermal signals, electromagnetic signals, optical signals and so on. Among them, visual inspection means have become a popular detection method in welding process because of its intuition, stability and large amount of information. For weld tracking, intelligent identification of weld deviations is the basis of precise and automatic welding control. The visual inspection of welding deviation has a wide applicability and is applied in the fields of laser welding, arc welding, friction welding and spot welding.

B. Zhang · Y. Shi (✉)
School of Mechanical and Automotive Engineering, South China University of Technology, Guangzhou 510640, China
e-mail: yhuashi@scut.edu.cn

© Springer Nature Singapore Pte Ltd. 2020

S. Chen et al. (eds.), *Transactions on Intelligent Welding Manufacturing*,
Transactions on Intelligent Welding Manufacturing,
https://doi.org/10.1007/978-981-15-7215-9_6

Some researchers use line structure light sensing technology to detect the corners of the weld to achieve the detection of the weld position [1]. Some researchers use cross-marked structured light to achieve weld seam tracking welding of thick plates [2]. Infrared thermography is used to analyze the information of the laser beam deviation from the weld position in laser welding [3]. Some researchers propose a template matching method to detect the weld center line of gas-shielded metal arc welding [4]. A robust image processing method is proposed to extract the welding offset from the welding image containing a lot of noise [5].

K-TIG welding is a novel welding method for medium-thick stainless steel welding, whose most important feature is high efficiency, cleanness and low cost [6]. The technical characteristics of single-side

welding and double-sided forming combined with automation technology can greatly improve the application of K-TIG welding in the industrial field. However, for K-TIG welding, the high current-generated compression current can achieve high penetration, but the strong arc light blocks the details of the welding area [7]. At the same time, the gap between the weldments is usually narrow, which makes it difficult to be identified accurately under the influence of the arc.

Aiming at the problems encountered in the automatic identification of K-TIG welding deviation, this paper proposes a welding deviation identification algorithm based on K-means clustering. Firstly, the brightness distribution characteristics of the K-TIG welding image are analyzed, and the center point of the cluster is determined on this basis. Then, the high dynamic range camera is used to image the K-TIG welding process, and images are divided into arc region, transition zone and seam region via K-means clustering. On one hand, an optimal path algorithm is proposed, in which the feature points of the electrode are detected in the arc region to estimate the position of the electrode tip covered by the arc light. On the other hand, the seam region is processed with a feature refinement algorithm, and then, the straight line is used to fit the position of the center line of the weld. Finally, the relative deviation between the tip of the electrode and the center line of the weld is calculated, and it is converted to the actual deviation on the basis of the camera calibration, and the automatic identification of the K-TIG welding deviation is finally realized.

2 Welding Deviation Identification System

The K-TIG welding process image acquisition system includes K-TIG deep-fusion welding torch, fixture, NIT high dynamic range NC1003 industrial camera and PC with image processing algorithm. Firstly, the brightness distribution of the welded image is analyzed, and the brightness span of the arc region and the seam region is obtained, which is used as the basis for determining the cluster center point. After determining the cluster center points corresponding to the three categories, a welding test is performed to capture the images in real time and transmit them to the PC for subsequent processing. After receiving the image, the PC side performs K-means classification on the image based on the previously obtained center point. Optimal

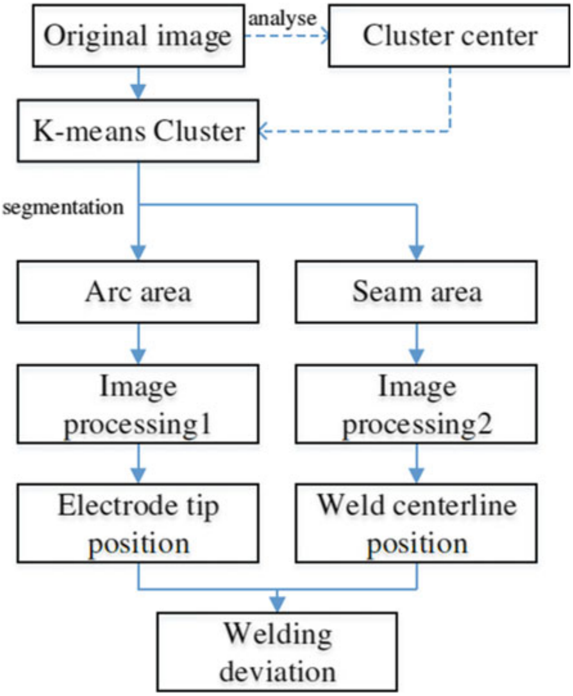
Original image
analyse
Cluster center
K-means Cluster
segmentation
Arc area
Seam area
Image processing1
Image processing2
Electrode tip position
Weld centerline position
Welding deviation

Fig. 1 Flowchart of welding deviation detection process

path processing and electrode tip point position extraction is then performed in the arc region. Then, the weld center line position is extracted via the refinement algorithm and straight line fitting in the seam region. Finally, the deviation between the tip points of the electrode with the center line of the weld seam is obtained. The algorithm flow is shown in Fig. 1.

3 Image Segmentation Based on K-Means Clustering Welding

3.1 Cluster Center Point Determination

According to the traditional K-means clustering algorithm, the center points are randomly set or determined via a time-costing algorithm. In the current research, different algorithms are proposed for the selection of K-means center points, such as K-means++ and data-based density parameter algorithm [8]. Although the clustering accuracy can be improved by using these methods, but they are time-costing and not very suitable for K-TIG welding. A clustering center point determination method based on K-TIG welding image brightness distribution is proposed. The cluster center

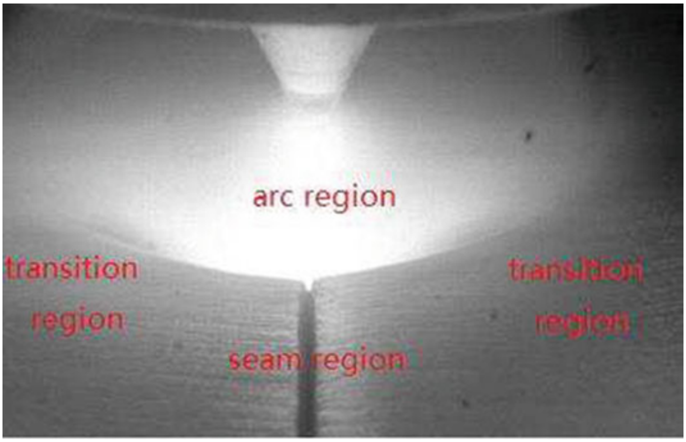

Fig. 2 Definition of different regions in the original image

point can be determined in advance by carrying out experiments before welding, which saves computational cost and ensures clustering accuracy.

K-TIG welding process has no spattering fumes, and the arc shape is stable under the same welding parameters. Moreover, in the case where the welding direction and the camera mounting position are determined, the acquired K-TIG welding image usually has a similar brightness distribution. Therefore, the arc region, the seam region and the transition region can be defined according to the welding experience in advance, as shown in Fig. 2. For images of different regions, the gray value corresponding to each pixel can be regarded as one object, and the three regions divided into three categories, the class center points can be determined by:

$$C_i = \frac{1}{N}\sum_{n=1}^{N} Z_{on}^{i} (i \in [1, 2, 3]) \tag{1}$$

where C_i is the category center, corresponding to arc zone, weld zone, transition zone. Z_{on}^{i} is the gray value corresponding to a pixel in a certain region, n is indexing pixels, N is the total number of the pixels in an image. From the multiple K-TIG welding images, the centers of the classes are obtained by the same method, and their average values are obtained. After the abnormal data is removed (when the area brightness abnormality usually occurs in the arcing and arcing stages), three cluster centers C_1, C_2, C_3 are obtained.

3.2 Image Segmentation

K-means clustering is an important method for spatial data partitioning or grouping [9]. It divides the spatial distance index of the research object into several subsets according to the similarity criterion so that the difference between the elements in the same subset is the smallest, while the difference among the elements in the different subsets is the largest. The usual spatial clustering algorithm is based on various distances, such as Euclidean distance, Manhattan distance and Mingcos distance. Among them, the most commonly used is the Euclidean distance:

$$d_n^i = \left[\sum_{n=1}^{N} \left(Z_n^i - C_i\right)^2\right]^{\frac{1}{2}} \tag{2}$$

where d_n^i is the Euclidean distance and Z_n^i is the gray value of the pixel taken from the image. According to the general principle of spatial clustering, the classification of categories should make the internal similarity of the same class the largest and the degree of difference the smallest. Spatial clustering generally uses distance as the partitioning criterion, that is, the distance between any spatial object and the geometric center of the class to which the object belongs is smaller than the distance of the object from the geometric center of any other class.

K-means algorithm is used to segment the K-TIG welding pattern: Based on what is analyzed above, the number of clusters is determined $k = 3$ and the cluster center point corresponds to each region C_1, C_2, C_3. For each remaining pixel, it is assigned to the nearest class based on its gray value and the Euclidean distance of each center. Then, recalculate the average of the pixels in each class to form a new cluster center. This process is repeated until the following criterion function converges:

$$E = \sum_{i=1}^{k} \sum_{p \in C_i} |p - m_i|^2 \tag{3}$$

where E is the sum of the squared errors of all gray values, p represents the pixels, that is data object, m_i is the average of C_i. After several iterations, the original image is classified into three categories, corresponding to the arc region, the transition region and the seam region, respectively, and the pixels from the same region have the same gray value, as shown in Fig. 3. According to the classification results, different regions are directly separated, and different subsequent image processing is performed.

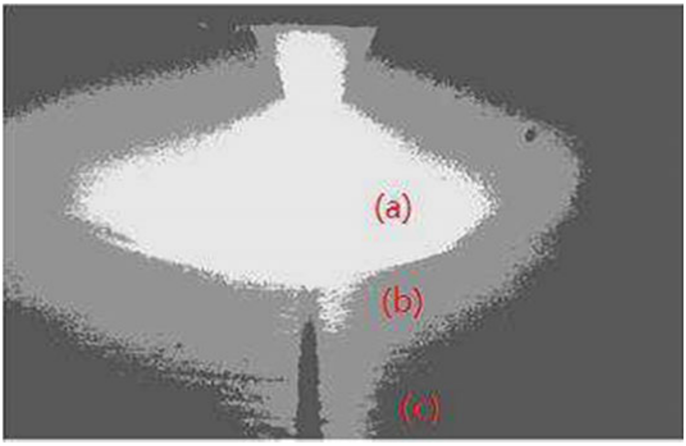

Fig. 3 K-means clustering area division results: **a** arc region; **b** transition region; **c** seam region

4 Subregional Feature Extraction

4.1 *Optimal Path Algorithm for Electrode Tip Position Extraction*

The identification of the weld deviation lies in the real-time positioning of the torch and the extraction of the weld position. However, for K-TIG welding with high arc brightness, it is masked by the arc light from the middle of the electrode, resulting in the inability to directly extract the position of the electrode tip point by visual inspection. This section presents an optimal path traversal algorithm. The feature points on the electrodes are identified from Fig. 4a, and the tip position is determined by extracting the electrode profile. The electrode tip position extraction algorithm flow is shown in Fig. 5.

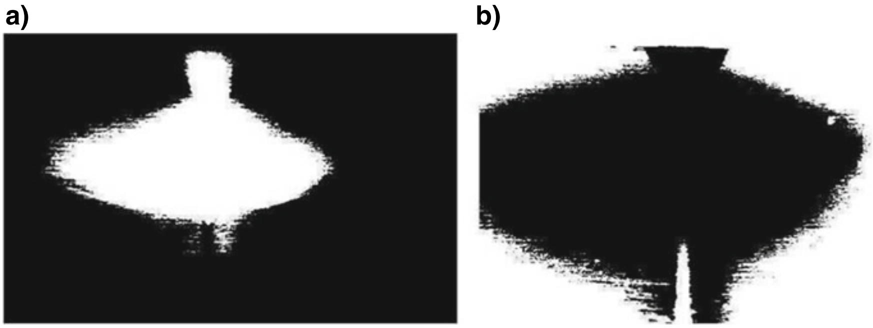

Fig. 4 Binary map after pattern segmentation: **a** arc region; **b** seam region

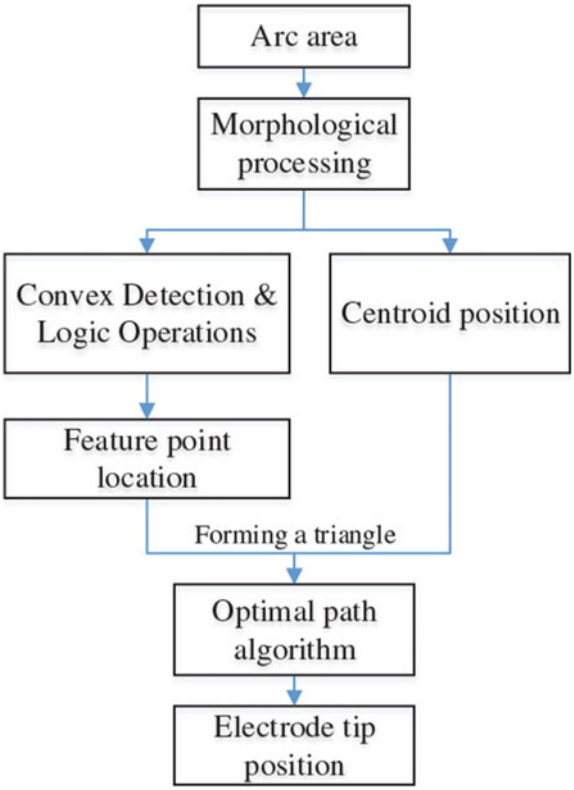
Arc area
Morphological processing
Convex Detection & Logic Operations
Centroid position
Feature point location
Forming a triangle
Optimal path algorithm
Electrode tip position

Fig. 5 Electrode tip position extraction algorithm flowchart

Firstly, the morphological corrosion expansion process is performed on the binary map of the arc region, and the discrete points around the arc are removed to get a smooth edge. Then, the closed pattern is convexly detected, and a minimum convex polygon is extracted which can completely surround the original image [10], as shown in Fig. 6. Then, the convex polygon and the arc region are logically operated to obtain a set of edge regions of several sizes. In this set, the connected domain is sorted, and the two largest connected domains are selected, which are defined as A_1 and A_2, respectively, corresponding to the two regions with the largest left and right, as shown in Fig. 7.

It can be seen that the tip point of the right side of A_1 and the tip point of the left side of A_2 are points on the outline of the electrode so these two feature points can be detected to reconstruct the electrode outline. An optimal path algorithm is proposed, which first traverses all the pixels of the arc region and then calculates out their particle point O according to their positional relationship by the following formula:

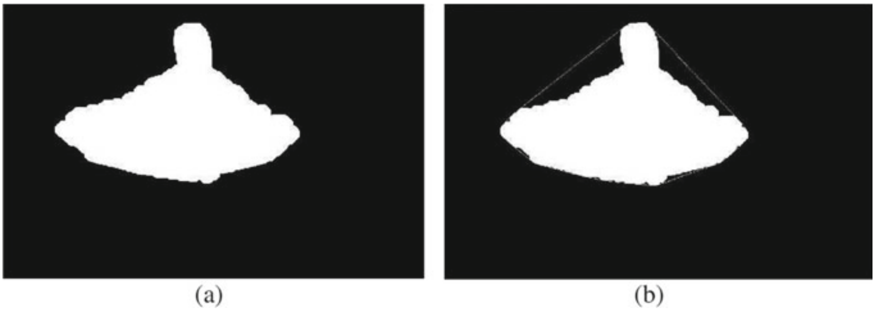

Fig. 6 Morphological processing for feature extraction: **a** morphology edge smooth in arc region; **b** convex hull detection

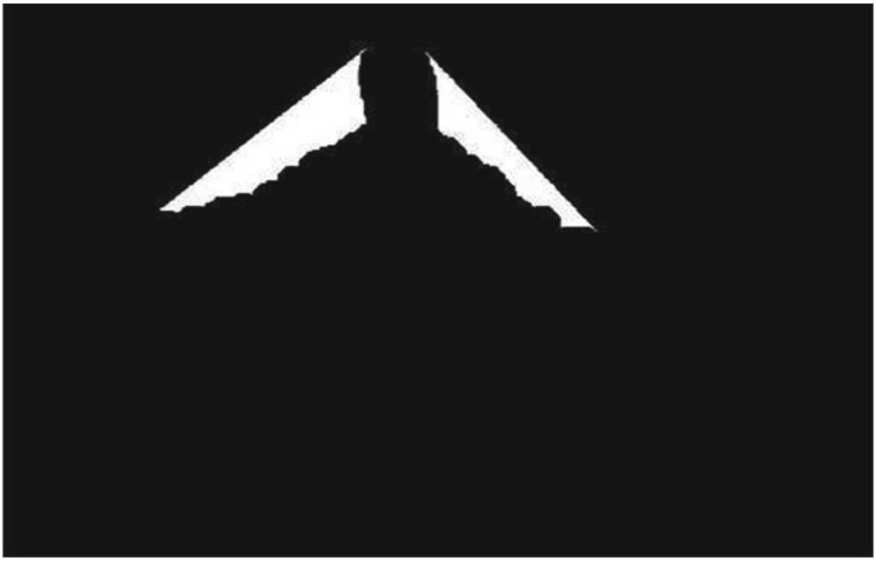

Fig. 7 Largest connected domain A_1 and A_2 in the set after the logical operation

$$\begin{cases} x_0 = \sum_{k=1}^{K} P_k x_k / \sum_{k=1}^{K} P_k \\ y_0 = \sum_{k=1}^{K} P_k y_k / \sum_{k=1}^{K} P_k \end{cases} \tag{4}$$

where (x_0, y_0) is the centroid coordinates, P_k is the pixels value, (x_k, y_k) is the pixel points taken from the arc region, K is the total number of pixels. A pixel R_1^k is selected from A_1, and a pixel R_2^k is selected from A_2, then a triangle is formed with R_1^k, R_2^k, O as vertex, as shown in Fig. 8. When the selected pixel point is changed, the circumference of the triangle also changes. Since the intersection of the electrode and the arc is the

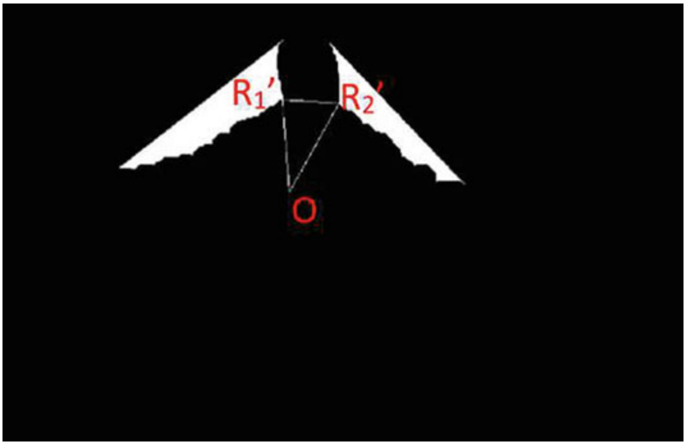

Fig. 8 Form a triangle with R_1', R_2', O as vertices

most central point in the A_1 and A_2, the circumference of the triangle formed by the intersection points and the center point is smaller than the circumference of the other triangles. It is therefore possible to form different triangles by traversing the pixel points in the A_1 and A_2. When the circumference of the triangle is the smallest, the corresponding vertexes are the characteristic point of the electrode to be extracted R_1', R_2':

$$C_{R_1' R_1' O} = \min\left\{C_{R_1^k R_2^k O}\right\} \tag{5}$$

where $C_{R_1^k R_2^k O}$ is circumference of the triangle under different selected points, $C_{R_1' R_2' O}$ is the minimum circumference. The pre-measured inclination of the tip of the electrode is =60°. Therefore, the contour line on the left sides $l_{R_1' O}$ and right sides $l_{R_2' O}$ of the electrode can be derived by combining the above contour feature points:

$$\begin{cases} l_{R_1' O} : \frac{y - y_0}{x - x_0} = \frac{y_{R_1'} - y_0}{x_{R_1'} - x_0} \\ l_{R_2' O} : \frac{y - y_0}{x - x_0} = \frac{y_{R_2'} - y_0}{x_{R_2'} - x_0} \end{cases} \tag{6}$$

where $\left(x_{R_1'}, y_{R_1'}\right)$ and $\left(x_{R_2'}, y_{R_2'}\right)$ are the coordinate values of the left and right feature points of the electrode. Combine two straight line equations to get the intersection of two contour lines (x_e, y_e), which is the position of the tip point of the electrode, as shown in Fig. 9.

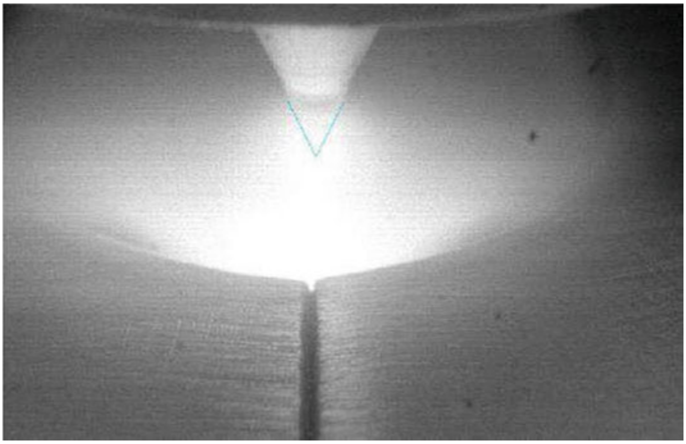

Fig. 9 Tip position of the electrode is obtained

4.2 Refinement Algorithm for Seam Center line Detection

The seam region is binarized as shown in Fig. 4b. The seam is in the middle of the image, but the image also contains the remaining interference areas. Because the seam is slender, different results can be obtained by two morphological treatment methods, and logical operations are performed between the different results to finally obtain the weld features. The flow is shown in Fig. 10. First, the first morphological process is applied to the binary map of the seam region, and the circular window with radius ra1 = 10 is firstly eroded and then expanded, as shown in Fig. 11a. Then, the second morphological process is applied by using a circular window with radius rb1 = 30 for erosion and another circular window of radius rb2 = 50 for expansion, as shown in Fig. 11b. Finally, the results of the two morphological processing are logically subtracted to obtain seam features, as shown in Fig. 11c.

The set of pixel points combined with the weld bead has a strip feature, so the obtained weld feature is refined to obtain a weld center line with burrs, as shown in Fig. 12a. The burr is generally at the head or bottom of the weld, which affects the direction of the weld line. Therefore, a straight line fitting algorithm with burr removal function is proposed to remove the curved part of the end and improve the detection accuracy of the weld, as shown in Fig. 12c. The algorithm strategy is as follows:

1. Traverse all the single pixel points from the seam, forming a set of points Ω.
2. Perform a least squares fit with these points to get a fitted straight line.
3. Get the number of the pixel falling on the fitted line, recorded as N.
4. Remove the first or last pixel of the seam from the point set Ω.
5. Repeat steps 2–4 in the new point set Ω until the N becomes the maximum $N_k(N_{k-1} \le N_k \ge N_{k+1})$.

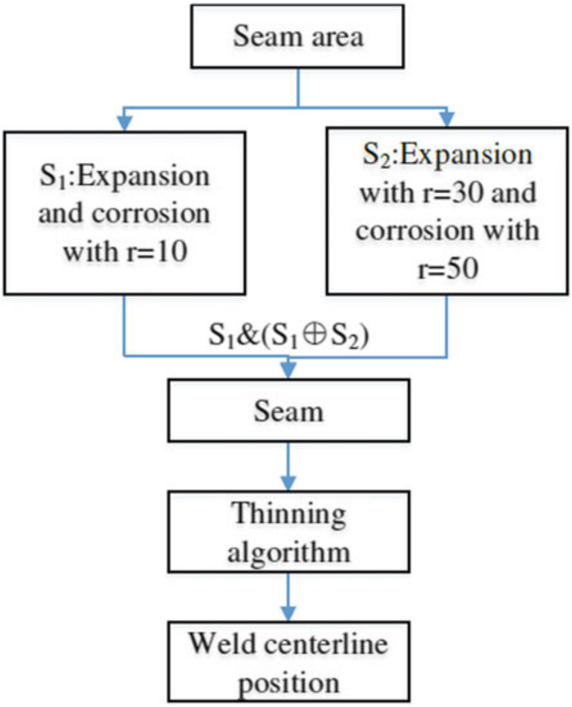
Seam area
S1:Expansion and corrosion with r=10
S2:Expansion with r=30 and corrosion with r=50
S1&(S1⊕S2)
Seam
Thinning algorithm
Weld centerline position

Fig. 10 Weld center line extraction algorithm flow

6. Exit the iteration. When N is maximum, the corresponding point set Ω is the center line of the seam without burr.

5 Test Verification

Experiments were carried out to verify the applicability of the proposed algorithm. Linear welding of 8 mm 304 stainless steel sheets at 500 A was performed. The torch moves along the seam but starts at the point which is 1.5 mm offset the seam and ends at the point which is −1.5 mm offset the seam. In the process, the K-TIG welding deviation extraction algorithm proposed in this paper is used to extract the position of the electrode and the position of the center line of the seam, and calculate the horizontal deviation between the two. After pre-camera calibration, the correspondence between the pixel-level coordinates of the visual inspection system and the world coordinates can be expressed as $\alpha = 0.023$ mm/pixel. The relationship can be obtained from the actual welding deviation. This deviation can be fed back to the welding motion control system, and the motion command can be timely adjusted to ensure good welding results. Comparison is made between several representative images from the test, as shown in Fig. 13. It can be seen that the electrode coincides with the center line of the seam, and the welding deviation is zero. The electrode

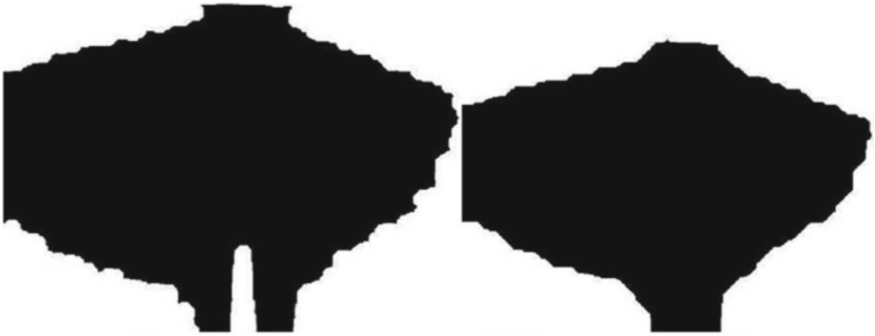

(a) smooth edges (b) Remove strip welds

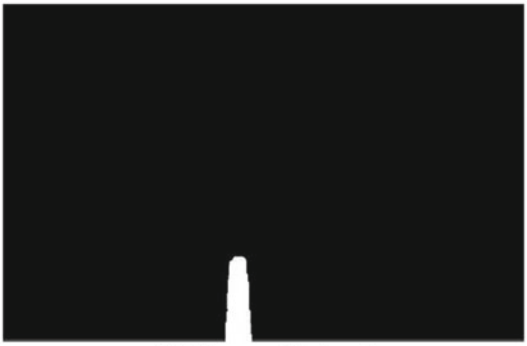

(c) Seam obtained

Fig. 11 Morphological processing

tip is rightly offset from the center line of the seam, and the actual deviation is calculated to be 0.138 mm. When the electrode is left-biased, a deviation of − 0.069 mm is identified. Therefore, the experiment proves that the algorithm can basically detect the deviation of the trajectory. The proposed algorithm has better accuracy and stability of K-TIG welding deviation recognition and provides a basis for realizing K-TIG automatic welding control.

6 Conclusion

During the K-TIG welding process, the arc is stable and bright, and the seam is a fixed butt weld type. In this case, the brightness distribution of the K-TIG welding image has a certain regionality. According to this characteristic, a welding deviation detection method based on K-means clustering is proposed to realize seam deviation detection in the K-TIG welding process. The main conclusions are as follows:

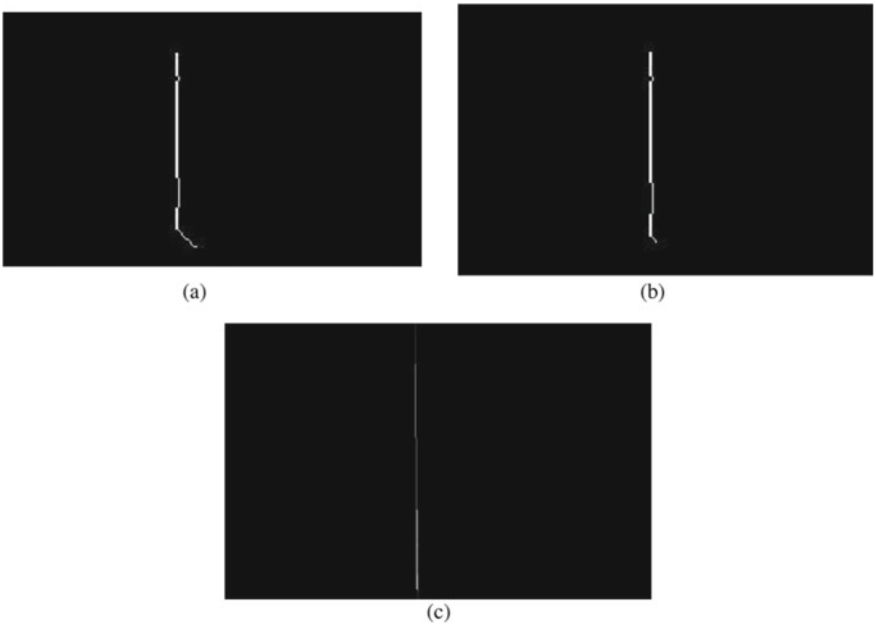

(a)

(b)

(c)

Fig. 12 Seam center line extraction: **a** refinement algorithm; **b** deburring; **c** line fitting

1. Using K-means clustering algorithm to realize K-TIG welding image segmentation, which is divided into arc region, seam region and transition region.
2. The optimal path traversal algorithm is proposed to detect the position of the tip of the electrode. At the same time, the optimized weld image refinement algorithm is proposed to improve the fitting accuracy of the seam center line.
3. The test proves that the proposed K-means algorithm can achieve good detection results for three different welding deviations.

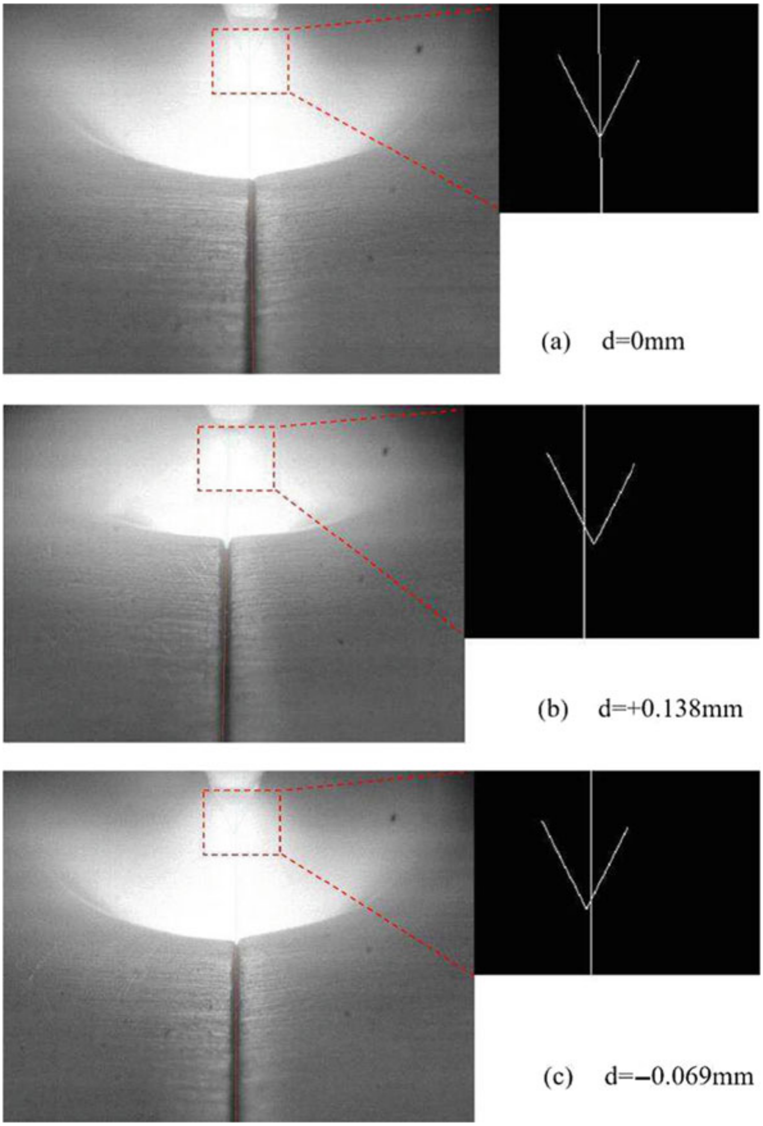

Fig. 13 Comparison between the welding deviations identified by the algorithm under different conditions. **a** The electrode overlaps the seam; **b** the electrode is offset to the right of the seam; **c** the electrode is deflected to the left of the weld

Acknowledgements This work was financial supported by the Key Research and Development Program of Guangdong Province (Grant No. 2020B090928003), and the Guangdong Province Marine Economic Development Project (Grant No. GDOE[2019]A13).

References

1. Wang WC, Gao XD, Ding XD et al (2018) Method for detecting corner points of butt welds without groove. Trans China Weld Soc 39(09):65–68, 135
2. Kiddee P, Fang ZJ, Tan M (2016) An automated weld seam tracking system for thick plate using cross mark structured light. Int J Adv Manuf Technol 87(9–12):3589–3603
3. Gao XD, Huang JY, Mo L (2013) Detection method of deviation angle of laser welded stainless steel micro-gap weld. Trans China Weld Soc 34(12):1–4
4. Wang XJ, Shi YH, Yu GQ, Liang B, Li Y (2016) Groove-center detection in gas metal arc welding using a template-matching method. Int J Adv Manuf Technol 86(9–12):2791–2801
5. Ding Y, Huang W, Kovacevic R (2016) An on-line shape-matching weld seam tracking system. Robot Cim Int Manuf 42:103–112
6. Zhang BR, Shi YH, Gu SY (2019) Narrow-seam identification and deviation detection in keyhole deep-penetration TIG welding. Int J Adv Manuf Technol 101:5–8
7. Zhang BR, Gu SY, Shi YH (2019) Robot deep-melting K-TIG welding system based on weld penetration penetrationdetection. J Mech Eng
8. Wong JAHA (1979) Algorithm AS 136: a K-means clustering algorithm. J R Stat Soc Ser C (Applied Statistics) 28(1):100–108
9. Arthur D, Vassilvitskii S (2007) K-Means++: the advantages of careful seeding. In: Proceedings of the eighteenth annual ACM-SIAM symposium on discrete algorithms. SODA 2007. ACM, New Orleans, Louisiana, USA, 7–9 Jan 2007
10. Li J, Sun LJ (2010) Pedestrian video detection algorithm based on convex clipping. Comput Eng 02:179–181

Thermal Characteristics of Narrow Gap GMA Welding at Vertical Position with Arc Swinging and Shifting

Hu Lan, Huajun Zhang, Jinjun Shao, Gang Li, Rui Pan, and Bin Wang

Abstract Research on thermal characteristics is the base for deeply understanding the process of narrow gap–fine wire–gas protection–one pass one layer–arc swinging and shifting–vertical welding. The plane analytic geometry method is adapted to solve the arc speed and welding line energy by analyzing the arc movement path. Based on classic heat source model of double ellipsoid, update of arc center position and orientation is achieved by coordinate transformation. The dynamic evolution of the weld pool under certain conditions is simulated, and thermal cycle curves of single layer and multilayer are extracted. The results show that the line energy of the process is pulsed and alternately assigned to both sides of the side wall, which lead to a narrow coarse-grained heat-affected zone (CGHAZ). The thermal cycle curve of CGHAZ presents the double characteristic of multi-peak, dwell time at high temperature is short, and cooling rate at low temperature is low. In addition, the weakest CGHAZ in the joint transforms into several micro-zones along the thickness of the weld, and the area ratio of reheated CGHAZ by normalizing, incomplete normalizing, and tempering is 3:2:5. If the thickness of the welding layer is properly controlled, the original CGHAZ of base metal are subjected to the grain refinement under the different layer welding thermal cycles conditions.

Keywords Narrow gap welding · Vertical welding · Arc swinging and shifting · Coarse-grained heat-affected zone · Welding thermal cycle

---

H. Lan · J. Shao · G. Li · R. Pan · B. Wang
Key Laboratory of Urban Rail Transit Intelligent Operation and Maintenance Technology & Equipment of Zhejiang Province, Zhejiang Normal University, Jinhua, Zhejiang 321005, China

H. Lan (✉)
Rongcheng Campus, Harbin University of Science and Technology, Rongcheng 264300, Shandong, China
e-mail: lanhu@zjnu.edu.cn

H. Zhang
Technology Department, Shanghai Zhenhua Heavy Industries Co., Ltd, Shanghai 200125, China

© Springer Nature Singapore Pte Ltd. 2020

S. Chen et al. (eds.), *Transactions on Intelligent Welding Manufacturing*,
Transactions on Intelligent Welding Manufacturing,
https://doi.org/10.1007/978-981-15-7215-9_7

1 Introduction

With the development of major national projects and modern industrial equipment toward high capacity and high parameters, the application of large-scale, heavy-duty, high-strength, and thick-plate metal structures is becoming more and more widespread [1]. However, large size and large wall thickness structures (pieces) are difficult to supply for the entire segment, so manufacturing through connection methods has become the first choice. Narrow gap gas shielded welding (NG-GMAW) is an efficient connection method. With the technical advantages of reducing the deposition amount and saving manufacturing time, it has wide application prospects in the manufacture of large-thickness members [2]. In order to ensure the uniform and reliable fusion of the two side walls during the NG-GMAW process, the key to solving this problem is to make the arc center with a higher energy density. Reasonably, close to the side wall of the angle of the zero-inclined bevel, swinging arc, rotating arc, shaking arc, and other technologies have been proposed and applied to NG-GMAW [3, 4]. Researching the heat in the arc swinging (or/and rotating) process characteristics are an important basis for deep understanding of narrow gap-filament-layer-to-layer-gas shielded welding process.

As we all know, the thermophysical properties of the NG-GMAW process will have an important impact on the thermal and metallurgical processes of its joints. The thermal characteristics of the gap-filament-layer-one-layer-swing-arc-arc-gas shielded welding dynamic process are more complex than conventional non-swing (straight through) or small swing amplitude ($\leq$3 mm) arc welding. At present, there is not much research on the characteristics of heat dissipation, mainly concentrated in scientific research institutions such as Harbin Institute of Technology, Wuhan University, Lanzhou University of Technology, Jiangsu University of Science and Technology, and Guangdong Institute of Welding Technology [5–7]. Zhang et al. [8, 9] by establishing a heat source model of narrow gap-thick wire-one layer two-pass-submerged arc welding, the temperature field of single-wire and double-wire narrow gap submerged arc welding (NG-SAW) temperature fields is simulated and found that the difference in wire attitude forms different temperature field. They also analyzed the temperature distribution characteristics of the single- and double-filament NG-SAW side wall coarse-grained heat-affected zone (CGHAZ) from the perspective of the corresponding relationship between the temperature field and the tissue transformation. Guo-xiang et al. [10] established a three-dimensional model that simulates the narrow gap-filament-layer-one-layer-swing arc-gas shielded welding temperature field and pool flow and found that there is a large vortex in the entire cross section of the pool. The flow of the molten pool is beneficial to the increase of the penetration depth of the side wall, and the width of the high-temperature area around the molten pool is smaller than that of conventional non-swing arc welding. The above research results are of great significance for the study of the thermal characteristics of the narrow gap-filament-gas protection-one-layer-one-swing-swing arc-vertical welding process.

In this paper, the analytical arc method and numerical analysis methods are used to analyze the arc welding process of the narrow gap swing arc GMA (NG-S^2GMA) robot vertical welding and simulate the dynamic evolution of the welding pool. Based on the welding temperature field and thermal cycle curve, we reveal the thermal characteristics of the narrow gap-filament-gas protection-one-layer-one-swing-swing arc-vertical welding process. It is of great scientific significance and engineering application value to lay the foundation for ensuring the optimal thermal process and the best joint performance of NG-S^2GMA robot vertical welding of key structures with large thickness.

2 Experiment

The core equipment of the NG-S^2GMA robot vertical welding system—the welding head—uses a patented product from Japan's Babcock-Hitachi Co., Ltd. (Fig. 1), which has linear movement, lateral swing, radial rotation, and composite action functions (all driven by servomotors), which can realize the efficient welding of thick-walled structural parts with a groove clearance of 18–20 mm and a groove depth of 200 mm. Different from the traditional multilayer and multi-channel filling method used in thick-plate vertical welding, NG-S^2GMA robot vertical welding adopts multilayer single-channel (one per layer) vertical welding method. The groove depth direction moves in a straight line, while the groove width direction movement is realized by the rotation and swing mechanism of the narrow gap head. The pre-curved section with a length of about 14–15 mm and an angle of 14°–15° with the

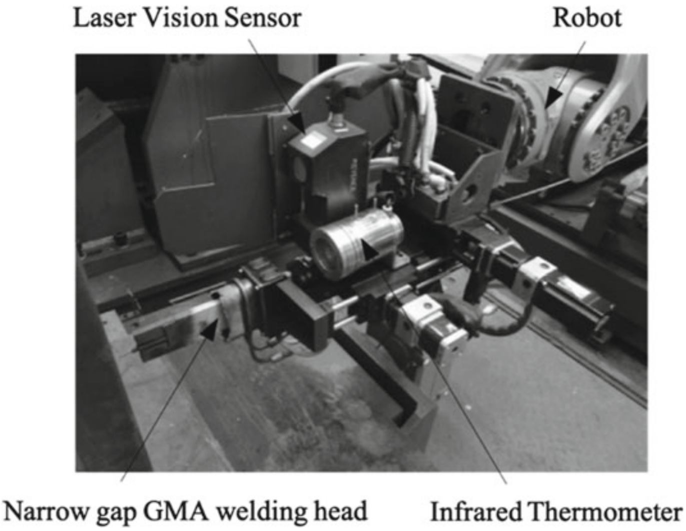

Fig. 1 Welding torch of NG-S^2GMA at vertical position

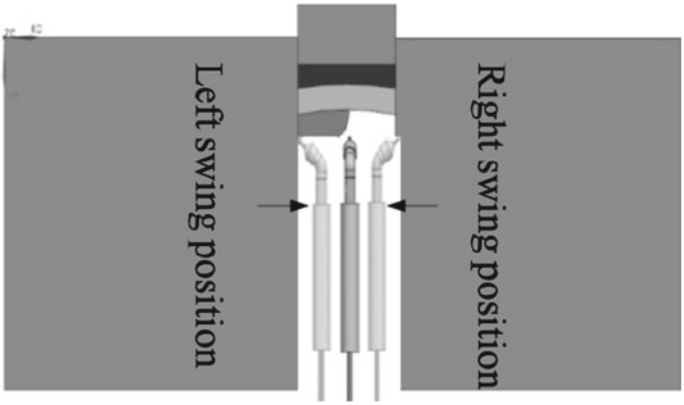

Fig. 2 Top view of NG-S^{2}GMA at vertical position

vertical rod axis is prefabricated at the front end of the conductive rod (the end connected to the conductive tip) so that the orientation of the wire tip changes. When the servomotor on the narrow gap head drives the conductive rod to reciprocate radial rotation, the wire tip (that is, the center of the arc) will rotate around the rod with a constant radius, and the direction of the arc will change periodically. In order to avoid excessive wire feeding resistance and excessively fast arc rotation, which affects the stability of the welding process and also takes into account the convenience of manual adjustment of the distance between the wire end and the groove side wall, the actual welding operation is often the arc rotating around the rod and lateral swing. It should be pointed out that the two sets of back and forth movements of rotation and swing are always synchronized, that is, when the arc moves from the center of the groove to the maximum swing position on both sides of the groove, the arc just rotates around the rod to the maximum rotation angle. The structure shown can obtain stable side wall fusion quality as shown in Fig. 2.

3 Arc Moving Process Analysis and Line Energy Calculation

Accurate control of the spatial position and orientation of the arc is the key to ensuring good fusion of the side walls of the NG-S^{2}GMA robot vertical welding groove. The movement path of the NG-S^{2}GMA robot vertical welding arc is shown in Fig. 3. It is not difficult to see that a complete arc movement process includes the arc's swing movement ($P_1 \rightarrow P_2$ and $P_3 \rightarrow P_4$) between the side walls of the groove (width direction of the groove) and the arc along the length of the groove when the swing is stopped to make a single linear movement ($P_2 \rightarrow P_3$ and $P_4 \rightarrow P_5$). That is to say, the movement speed of the NG-S^{2}GMA robot vertical welding arc is intermittent,

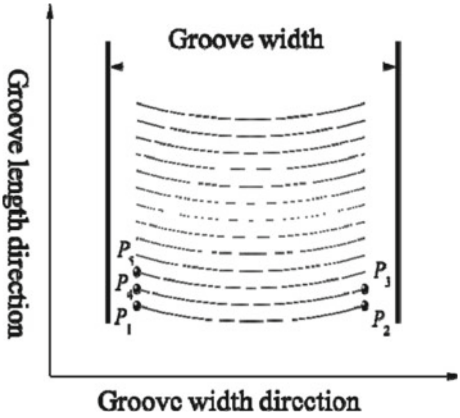

Fig. 3 Arc trajectory of NG-S^{2}GMA at vertical position

and its size and direction change periodically with the spatial position of the arc, which is different from the conventional non-swing gas shielded welding.

It is well known that the calculation formula of welding line energy is $E = UI/v$ which is determined by the welding speed (or arc moving speed) when the welding current and arc voltage are constant. If you want to qualitatively or quantitatively analyze the thermal characteristics of the narrow gap-filament-gas shield-layer-by-layer-rotary pendulum arc-vertical welding process, you need to accurately calculate the speed of the arc along the moving path in Fig. 3. Among them, $P_2 \rightarrow P_3$ and $P_4 \rightarrow P_5$ are a single linear movement section, and the moving speed of the arc v_r is equal to the moving speed of the end of the robot wrist, and its size and direction remain unchanged. While the two sections $P_1 \rightarrow P_2$ and $P_3 \rightarrow P_4$ are swing pendulum movements, the moving speed of the arc is synthesized by the lateral swing speed and radial rotation speed (linear speed) (Fig. 4). The angle of the speed direction has been changing, which can be expressed as:

$$\theta = \begin{cases} \theta\text{max} - \omega \cdot \text{mod}\left(\frac{t}{T}\right) & \text{mod}\left(\frac{t}{T}\right) < \frac{T}{2} \\ \theta\text{max} - \omega \cdot \left[\text{mod}\left(\frac{t}{T}\right) - \left(\frac{T}{2}\right)\right] & \text{mod}\left(\frac{t}{T}\right) > \frac{T}{2} \end{cases} \tag{1}$$

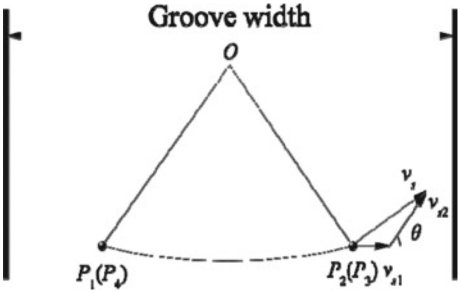

Fig. 4 Arc speed of NG-S^{2}GMA at vertical position

where $\bmod\left(\frac{t}{T}\right)$ is the remainder function of time, t is the total welding time, T is the arc movement period, $T = 2(t_s + t_r)$, $t_s = \lambda / v_{s1}$, and λ are the amplitude of the lateral swing of the arc 5–7 mm, and the swing stop time of the single-side groove is 1.5–1.8 s; ω is the angular velocity of the arc's radial rotation around the rod, $\omega = \theta_{\max}/(\pi \cdot t_s)$; $\theta_{\max}$ is the maximum angle of radial rotation 45°–50°.

If the angle θ between the lateral oscillating speed v_{s1} and the radial rotational speed v_{s2} is known, the moving speed of the vertical welding arc of the NG-S^{2}GMA robot can be expressed as:

$$v = \begin{cases} v_r & P_2 \to P_3 \cup P_4 \to P_5 \\ \sqrt{v_{s1}^2 + v_{s2}^2 + 2v_{s1}v_{s2}\cos\theta} & P_1 \to P_2 \cup P_3 \to P_4 \end{cases} \tag{2}$$

In the formula, $v_{s2} = (l_b + l_w) \cdot \omega \cdot \cos\alpha\ l_b, l_w$ are the parameters that define the radius of rotation of the arc around the rod, l_b is the length of the conductive rod bending section 14–15 mm, l_w is the dry elongation of the welding wire 12–15 mm, α is the conductive rod bending section, and the angle of the rod axis is 14°–15°.

Through experiments, it was found that when the arc's lateral swing speed $v_{s1} = 0.35 \sim 0.45$ m/min^{-1} along the groove width direction and linear movement speed $v_r = 0.09 \sim 0.10$ m/min^{-1} along the groove length direction, the NG-S^{2}GMA robot's vertical welding process has good stability, and the weld seam is beautifully formed and slightly concave. At this time, the speed–time curve of the vertical welding arc of the NG-S^{2}GMA robot in one cycle calculated by Eqs. (1) and (2) is shown in Fig. 5. Obviously, the movement speed of the arc shows a "pulse" characteristic. The speed of the "peak" swing section ($v \approx 1.10 \sim 1.20$ m/min^{-1}) exceeds the speed of the "base value" linear section ($v \approx 0.10$ m/min^{-1}) by more than ten times, and the "duty cycle" is about 0.4. As mentioned above, while keeping

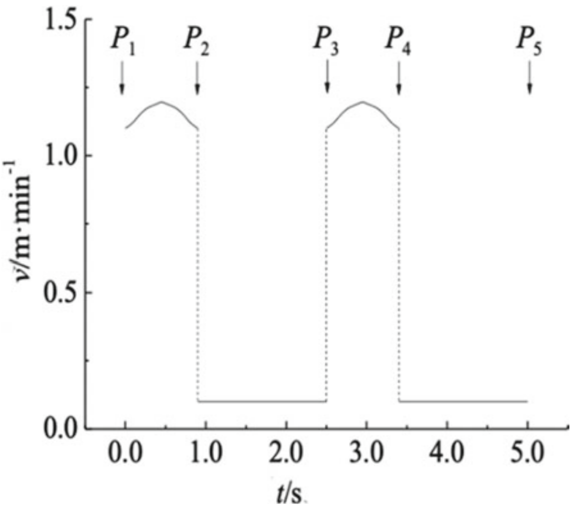

Fig. 5 Variation of arc speed in robotic NG-S^{2}GMA welding at vertical position

the arc power constant, the linear energy of the NG-S^{2}GMA robot's vertical welding arc is opposite to the change law of the arc moving speed; that is, the swing pendulum segment can be regarded as the "base value" of the pulse line energy. The straight-line segment is the "peak value" of the pulse line energy. The national standard GB/T 3375-94 positions the welding speed as the length of the weld completed in a unit of time, from which the arc line energy in half or one cycle is calculated as:

$$E = \frac{UI}{v_r} \cdot \frac{t_r + t_s}{t_r} \tag{3}$$

Considering that the length of the trajectory l_s of the swing welding arc of the NG-S^{2}GMA robot's vertical welding arc is about four times the length of the straight line trajectory l_r, it may be possible to calculate the arc energy according to the actual motion trajectory in segments and express it as:

$$E' = \frac{UI}{v_r} \cdot \frac{t_r}{t_r + t_s} + \frac{UI}{v_s} \cdot \frac{t_s}{t_r + t_s} \tag{4}$$

In the formula, v_s is the combined speed of arc swing pendulum $1.10 \sim 1.20\text{m/min}^{-1}$. Divide Eqs. (3) and (4) to get:

$$\frac{E}{E'} = \frac{v_s}{t_r} \cdot \frac{(t_r + t_s)^2}{v_s t_r + v_r t_s} \approx 2.3 \tag{5}$$

From the calculation result of Eq. (5), the arc energy calculated by method 2 is less than half of method 1. In order to confirm the rationality of the above two-line energy calculation methods, try high-quality offshore engineering steel (advanced low alloy quenched and tempered high-strength steel Q690E) NG-S^{2}GMA robot vertical welding (No. 1-1$^\#$) and conventional non-swing arc GMA robot vertical welding (No. 1-2$^\#$ and 1-3$^\#$) heat-affected zone width comparison test. During the test, the distance between the end of the welding wire (the center of the arc) and the side wall of the groove and the direction of the arc remain unchanged. The measurement results of the width of the joint heat-affected zone (excluding the high-temperature tempering zone) under different specifications are shown in Table 1. It can be clearly seen from Table 1 that as the line energy increases ($12.1 \rightarrow 24.1\ \text{kJ/cm}^{-1}$), the width of the heat-affected zone of the base material side wall increases (1.8 → 2.4 mm). The existing research results show that it is not the total

Table 1 Width of HAZ in vertical GMA welding under different processes

	I (A)	U (V)	V (m/min^{-1})	θ (°)	λ (mm)	t_s (s)	E (kJ/cm^{-1})	W (mm)
1-1$^\#$	125	22.5	0.09	45	6	1.6	12.5	1.8
1-2$^\#$	125	22.5	0.14	–	–	–	12	1.8
1-3$^\#$	125	22.5	0.07	–	–	–	24.1	2.4

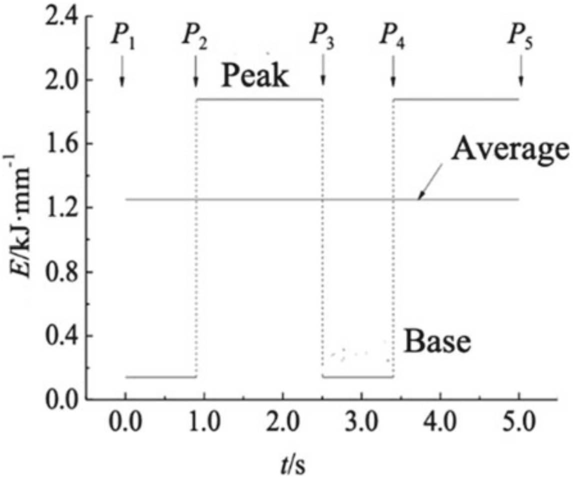

Fig. 6 Variation of weld heat input in robotic NG-S^{2}GMA welding at vertical position

energy of the arc that actually affects the width of the heat-affected zone of the side wall, but the heat input of the arc to the side wall. The width of the heat-affected zone of the NG-S^{2}GMA robot vertical welding (1-1$^\#$) is the same as the width of the heat-affected zone of the (1-2$^\#$) joint using the conventional non-swing arc GMA robot vertical welding. The heat input of the base material side wall under the two-process specifications is basically the same (~12 kJ/cm^{-1}). Using Eq. (4), it is reasonable to calculate the line energy according to the arc movement path in sections (Fig. 6).

It is worth noting that the total arc energy of the NG-S^{2}GMA robot vertical welding is cyclically transferred to the side wall of the base material on both sides, and the fusion of the side walls of the groove is “time-sharing” rather than synchronized. The heat required for side wall fusion mainly comes from the “peak value” of the pulse arc line energy. The “base value” plays a good role in preheating and post-heat slow cooling. In addition, the width of the heat-affected zone of the (1-1$^\#$ and 1-2$^\#$) joints is 1.8 mm, indicating that only 2/3 of the pulse arc energy “peak” of the NG-S^{2}GMA robot vertical welding process on the side wall of the base material. The lower side wall heat input is beneficial to the damage of base metal strength, plasticity, and toughness, especially advanced high-strength steel and ultra-high-strength steel. Regarding the whereabouts of residual energy and what kind of joint forming characteristics will be produced by the intermittent arc movement process, further research and analysis of the dynamic evolution of the weld pool is needed.

4 Analysis of Evolution of Molten Pool Morphology and Joint Forming Characteristics

In view of the fact that high-speed camera is not suitable for the monitoring of deep and narrow working conditions approaching zero bevel angle, the paper uses a computer to simulate the dynamic evolution process of narrow gap–fine wire–gas protection–one pass one layer–arc swinging and shifting–vertical welding. The heat source model uses a double-ellipsoid heat source model, and the heat flux distribution function of the front half ellipsoid can be expressed as [11]:

$$q_f(x, y, z) = \frac{6\sqrt{3} f_f Q}{abc_1\pi\sqrt{\pi}} \exp\left\{-3\left(\frac{x^2}{a^2} + \frac{y^2}{b^2} + \frac{z^2}{c_1^2}\right)\right\} \quad (6)$$

The heat flux density distribution function of the second half ellipsoid can be expressed as:

$$q_r(x, y, z) = \frac{6\sqrt{3} f_r Q}{abc_2\pi\sqrt{\pi}} \exp\left\{-3\left(\frac{x^2}{a^2} + \frac{y^2}{b^2} + \frac{z^2}{c_2^2}\right)\right\} \quad (7)$$

In the formula, a, b, c_1, c_2 is the coefficient that defines the shape of the heat source; f_f, f_r is the energy distribution coefficient that defines the front and rear hemispheres; $f_f + f_r = 2$ generally takes $f_f = 0.6$, $f_r = 1.4$; Q is the total power of the arc heat source, $Q = \eta UI$, and η is the thermal efficiency coefficient.

The moving process of the vertical welding arc of the NG-S^{2}GMA robot can be regarded as the continuous updating process of the spatial position and direction of the arc center (end of the welding wire) in the groove. Similar to the method described in [12], the movement process of the arc along the path ($P_1 \rightarrow P_2 \rightarrow P_3 \rightarrow \ldots$) in Fig. 3 is simulated by the segmented coordinate transformation method. The dynamic evolution of the molten pool morphology is shown in Fig. 7. It is not difficult to see that it is different from the synchronous fusion of the two side walls of the groove during conventional gas welding with no swing or small swing amplitude. The side welding of the side walls of the NG-S^{2}GMA robot vertical welding with a groove gap of 18–20 mm is obvious. The fusion process of the one-sided side wall is a linear movement section when the swing is stopped. It confirms the conclusions drawn from the above dynamic analysis of the "intermittent arc movement" and "pulse arc line energy" dynamic processes. Looking at Fig. 7, we can also find that when the arc moves from one side of the groove to the other side of the groove ($P_1 \rightarrow P_2$, $t = 15$–16 s), the moving speed of the arc increases rapidly by ten times. Due to the low surface tension, part of the liquid-deposited metal quickly moves with the arc center, and the surface morphology of the molten pool is elongated, which causes the heat input that originally affected the side wall of the base material to shift-dynamic redistribution of the molten pool heat. After that, the arc line energy remained at the base level, the peak temperature of the molten pool continued to decrease (2400 → 1900 °C), and the melting depth was shallow. When the arc moves to the other side of the groove ($P_2 \rightarrow P_3$, $t = 16$–17.5 s), the swing motion temporarily stops, and the side wall of the base material begins to receive continuous heat input from the peak value of the pulse arc energy. The "tailing" of the molten pool gradually disappears, the volume gradually increases, the peak temperature continues to rise (1900 → 2400 °C), the melting depth also increases, and the molten pool basically returns to the shape

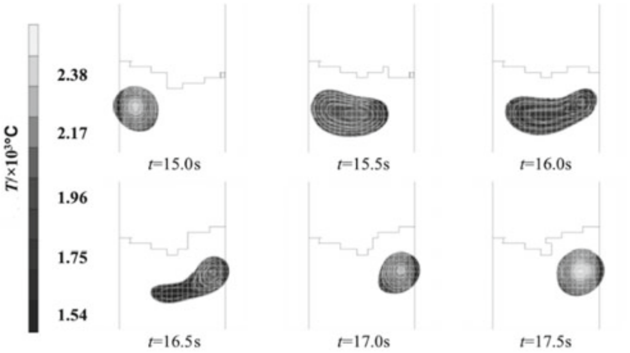

(a) Surface topography

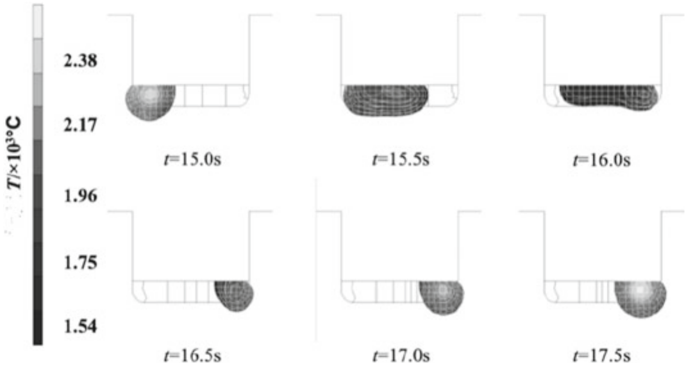

(b) Cross-sectional morphology of the molten pool

Fig. 7 Evolution of molten pool in robotic NG-S^2GMA welding at vertical position

before the swinging movement. That is to say, the main reason for the narrow gap-filament-gas protection-layer-by-layer-swing pendulum arc-vertical welding joint heat-affected zone is the intermittent movement of the arc to cyclically alternate heat input to the base material side wall. The actual joint appearance of Q690E low alloy quenched and tempered high-strength steel NG-S^2GMA robot vertical welding is shown in Fig. 8. The surface is formed uniformly and beautifully, the side wall of the base metal is well fused (melting depth ~1 mm), the thickness of the welding layer is moderate (3–4 mm), and the welding waveform is like "building blocks" instead of "fish scales," The cross section of the weld is like a "peanut shell" instead of a "finger," and the penetration depth between the weld layers is consistent with the change in arc energy. The peak penetration is large (2–3 mm), and the base penetration is small (~1 mm). The above joint forming characteristics are the result of the evolution process of the dynamic shape of the molten pool.

As one of the preferred technologies for welding thick-walled structural parts, narrow gap-filament-gas shield-layer-by-layer-swing pendulum arc can obtain a

Fig. 8 Weld appearance of robotic NG-S^{2}GMA welding at vertical position

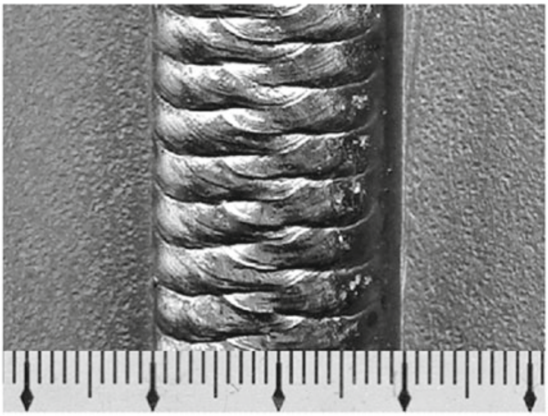

(a) Weld surface forming

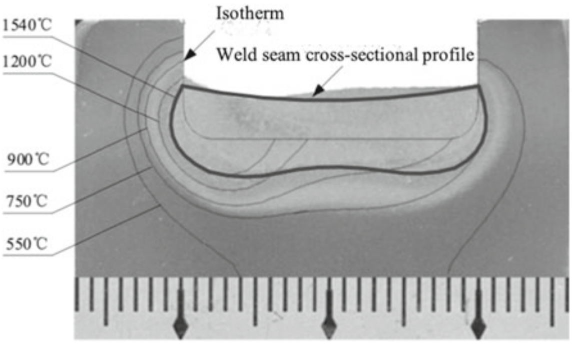

(b) Weld seam cross-sectional profile

narrower base material heat-affected zone (HAZ) through smaller welding line energy. The width of the HAZ of the vertical welding joint of the experimental steel NG-S^{2}GMA robot is basically controlled at about 3 mm, distributed according to the isotherm away from the fusion line (Fig. 7b). HAZ can be divided into coarse-grained heat-affected zone (CGHAZ, 1200–1540 °C), fine-grained heat-affected zone (FGHAZ, 900–1200 °C), dielectric-critical heat-affected zone (ICHAZ, 750–900 °C), and subcritical heat-affected zone (SCHAZ, 550–750 °C). The width ratio of each micro-area is 2:2:1:3 (different from SCHAZ > CGHAZ > FGHAZ > ICHAZ in conventional non-swing gas shielded welding). Although the width of CGHAZ is only 1/4 of HAZ (~0.8 mm), the peak temperature of the thermal cycle experienced by this micro-area is high, which is prone to coarsening and embrittlement. As a result, the performance of the micro-zone is “deteriorated” and becomes the “short board” of the entire joint. For the NG-S^{2}GMA robot vertical welding, what kind of thermal process has CGHAZ experienced? This is the basic premise for analyzing the evolution of the structure and performance of the test steel CGHAZ.

5 Analysis of Thermal Cycle Curve in Coarse-Grained Region and Transformation of Micro-Region

In order to reveal the thermal characteristics of the narrow gap-filament-gas shield-layer-by-layer-swing-arc-arc-vertical welding process, the CGHAZ temperature curves of GMA vertical welding joints under different specifications were obtained (Fig. 9). It can be clearly observed from Fig. 9 that, unlike the “single-peak” thermal cycle curve formed by conventional non-swing arc GMA robot vertical welding (2-2$^{\#}$ and 2-3$^{\#}$), NG-S^{2}GMA robot vertical welding (2-1$^{\#}$) presents a “multi-peak” characteristic. It consists of a “primary peak” and multiple “secondary peaks” immediately adjacent to it. Statistics show that the time interval between adjacent peaks–peaks (or troughs–troughs) on the thermal cycle curve 2-1$^{\#}$ is exactly the arc movement period (~5 s). It shows that the crest is caused by the arc approaching the side wall of the base material (temperature measurement point) successively during the intermittent reciprocating movement in the groove, and the trough is formed by the arc gradually away from the side wall of the base material (temperature measurement point). Therefore, “multi-peak” can be regarded as an inherent thermophysical characteristic of swing arc welding. However, the thermal cycle characteristic parameters (such as high-temperature residence time, cooling time) of the multi-peak curve (2-1$^{\#}$) and single-peak curve (2-2$^{\#}$ and 2-3$^{\#}$) are quite different. The test conditions and statistical results are listed in Table 2.

Fig. 9 Heat cycle curves of CGHAZ in vertical GMA welding under different processes

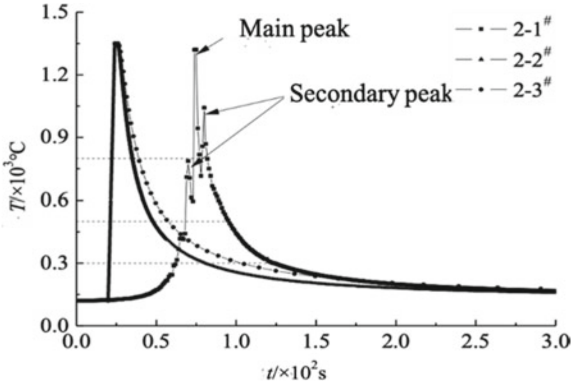

Table 2 Cooling rate of CGHAZ in vertical GMA welding under different processes

	T_0 (°C)	E (kJ/cm^{-1})	Interval time		
			t_H	$t_{8/5}$	$t_{8/3}$
2-1$^{\#}$	120	12.5	1.5	17.6	45.8
2-2$^{\#}$	120	24.1	4.9	13	45.8
2-3$^{\#}$	120	32.6	6	18.3	64.1

Comparing the thermal cycle curve parameters calculated in Table 2 found that under the same cooling time, the line energy of the NG-S^{2}GMA robot vertical welding (2-1$^\#$) is about the half of the conventional non-swinging arc GMA robot vertical welding (2-2$^\#$). The high-temperature residence time of 2-1$^\#$ CGHAZ is also less than 1/3 of 2-2$^\#$. However, the cooling time $t_{8/5}$ of 2-1$^\#$ exceeds 2-2$^\#$ 4.6 s. Similarly, under the same cooling time, the line energy of 2-1$^\#$ is less than 2/5 of 2-3$^\#$. The high-temperature residence time above 1200 °C is only 1/4 of 2-3$^\#$. This shows that the NG-S^{2}GMA robot vertical welding can obtain a slower cooling rate through a smaller line energy, which is conducive to improving the cold crack resistance of the joint. The high-temperature residence time of CGHAZ is short, which is helpful to avoid the structure being too thick and improves the thermal crack resistance of the joint; that is, the NG-S^{2}GMA robot vertical welding process has good comprehensive crack resistance. The analysis believes that the forming process of the "building blocks" (thickness 2.5–3 mm) of the joint is strong evidence of the "pulsed" characteristics of the heat input of the base material side wall. From the perspective of the effect of heat, the superposition process of three "building blocks" on the side next to the temperature measurement point corresponds to the three valleys of the thermal cycle curve → the peak temperature rise section. On the other side of the bevel, the "building blocks" superimposed on the above three "building blocks" correspond to the peak → valley cooling section. In other words, the "main peak" of the thermal cycle curve is generated when the "building blocks" are stacked close to the temperature measurement point, and the pause time of the arc swing is approximately equal to the high-temperature residence time. The two "building blocks" superimposed are similar to the preheating of the front arc to the rear bead in double-arc welding, and the three "building blocks" superimposed thereafter are similar to the post-heating of the rear arc to the previous bead in double-arc welding. In Fig. 9, the three trough temperatures formed by the superposition of "building blocks" on the opposite side of the temperature measurement point are 596, 715, and 750 °C, respectively. Multiple pulse preheating and post-heating have played a good slow cooling effect.

The thick-walled component NG-S^{2}GMA robot vertical welding adopts a multi-layer single-pass filling method, and the rear weld bead (layer) is bound to have a thermal effect on the previous weld bead (layer) and HAZ. The welding layer of NG-S^{2}GMA robot vertical welding head is relatively thin (3–4 mm), and the penetration depth of the welding seam when the arc swing is paused is large (2–3 mm). This means that the thickness of the arc heat action exceeds 5 mm, and basically, the current layer of weld beads will affect the previous two layers of weld beads. In other words, the base material side wall CGHAZ will undergo reheating processes such as normalizing, incomplete normalizing, and tempering of the rear weld bead (layer). The thermal cycle curve shows the dual characteristics of "multi-peak," and the organization and performance of the micro-area change accordingly. Taking the welding layer thickness of 3.5 mm as an example, the thermal process of the multi-layer vertical welding of the NG-S^{2}GMA robot is simulated by superimposing the HAZ isotherms during single-layer vertical welding. The isotherm distribution and micro-zone division of the CGHAZ of the base material side wall are obtained as shown in Fig. 10. In order to distinguish the description, each micro-area is described

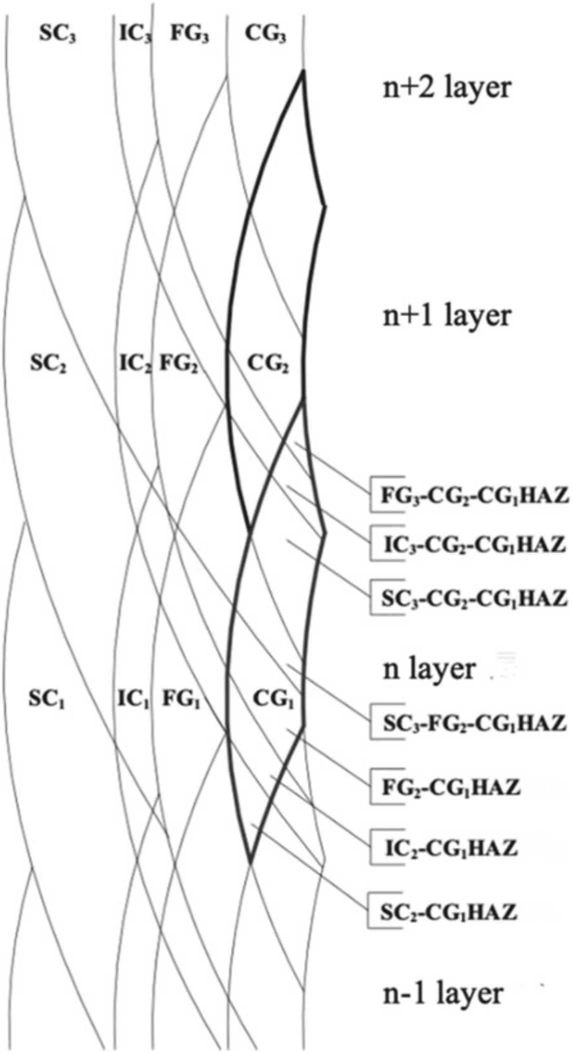
SC₃
IC₃
FG₃
CG₃
n+2 layer
n+1 layer
SC₂
IC₂
FG₂
CG₂
FG₃-CG₂-CG₁HAZ
IC₃-CG₂-CG₁HAZ
SC₃-CG₂-CG₁HAZ
n layer
SC₁
IC₁
FG₁
CG₁
SC₃-FG₂-CG₁HAZ
FG₂-CG₁HAZ
IC₂-CG₁HAZ
SC₂-CG₁HAZ
n-1 layer

Fig. 10 Evolution of CGHAZ in robotic NG-S^2GMA welding at vertical position

with English letters and Arabic numerals. Arabic numerals represent the number of welding thermal cycles experienced by CGHAZ. Observe the distribution of the HAZ isotherms shown in Fig. 10, and CGHAZ of the base metal side wall corresponding to each weld is shaped like a "big knife" (the thick red line and the blue thick line mark the part). When the weld of the $n + 1$ layer is completed, the base material CGHAZ of the n layer has experienced secondary overheating, normalizing, incomplete normalizing, and tempering from top to bottom. It is transformed into four micro-zones, namely CG2-CG1HAZ, FG2-CG1HAZ, IC2-CG1HAZ, and SC2-CG1HAZ. The proportion of the area of each micro-zone is 40, 39, 12, and 9%. When the $n + 2$ layer weld is completed, CG2-CG1HAZ is transformed into three micro-zones (FG3-CG2-CG1HAZ, IC3-CG2-CG1HAZ, and SC3-CG2-CG1HAZ), and the proportion of the area of each micro-zone is 4, 8, and 28%. FG2-CG1HAZ transforms into two micro-zones (SC3-FG2-CG1HAZ and FG2-CG1HAZ), which occupy about 16 and 23% of the area. In short, after undergoing the reheating effect of the rear weld bead (layer), the weakest CGHAZ in the vertical welding joint of the NG-S^{2}GMA robot forms several micro-areas along the thickness direction of the weld. Experience normalizing (FG3-CG2-CG1HAZ and FG2-CG1HAZ), incomplete normalizing (IC3-CG2-CG1HAZ and IC2-CG1HAZ), and tempering (SC3-CG2-CG1HAZ, SC3-FG2-CG1HAZ, and SC2-CG1HAZ), the area ratio of the micro-area is 3:2:5. Moreover, if the thickness of the welding layer is properly controlled, the original CGHAZ of the base material is basically eliminated. This shows that the NG-S^{2}GMA robot vertical welding process itself has the function of optimizing the joint structure and performance. However, due to the different reheat processes experienced by each transition micro-region, its organization and performance improvement mechanisms and effects are also different, and further research is needed.

6 Conclusion

1. Due to the intermittent movement of the arc, the narrow gap–fine wire–gas protection–one pass one layer–arc swinging and shifting–vertical welding line energy changes are pulse characteristics. The heat required for the fusion of the base material side wall comes from the peak value of the pulse arc line energy.
2. Narrow gap–fine wire–gas protection–one pass one layer–arc swinging and shifting–vertical welding total energy are distributed alternately to the side wall of the base material on both sides. The side wall thermal cycle curve has multi-peak characteristics, residence time at high temperature is short, cooling rate at low temperature is slow, and heat influence zone of coarse crystal is narrow.
3. The weakest coarse-grained heat-affected zone in the joint is transformed into several micro-zones along the thickness of the weld by the reheating effect of multilayer welding. The original coarse-grained heat-affected zone is basically eliminated, but the structure and performance of each transition micro-zone are different, and the improvement mechanism is also different.

References

1. Wang P, Liu X, Lu F-g (2016) Application of deep-narrow gap welding method in manufacturing component with heavy section. J Mech Eng 52(2):56–61
2. Zheng Y-w, Cai Z-p, He Y-c et al (2016) Study on the influence of fusion ratio on carbon migration phenomenon in the narrow gap welding of dissimilar steels. J Mech Eng 52(12):74–80

3. Zhang F-j, Guo J-l, Zhang G-d (2017) Key technologies of narrow gap gas shielded arc welding. Electr Weld Mach 47(7):30–33
4. Lan H, Zhang H-j, Chen S-b et al (2014) Correlation of arc sound and arc-sidewall position in narrow gap MAG welding. J Mech Eng 50(12):38–43
5. Li W-h, Gao K, Wang J-y et al (2015) A vison sensing based welding deviation detection algorithm for rotation arc narrow gap MAG welding. J Shanghai Jiao Tong University 49(3):353–356
6. Xu W-h, Lin S-b, Yang C-l et al (2017) Study on droplet transfer of swing arc narrow gap GMAW. Trans China Weld Inst 38(2):109–114
7. Gu Y-f, He G-y, Shi Y et al (2016) Detection and analysis of arc shape and droplet transfer behavior of narrow gap GMAW. J Shanghai Jiao Tong University 50(10):1526–1534
8. Zhang L, Liu C-q, Yu J-w et al (2016) Numerical analysis of temperature field of narrow gap submerged arc welding. Trans China Weld Inst 37(3):83–87
9. Zhang L, Liu C-q, Yu J-w et al (2016) Numerical analysis of microstructure evolution of coarse grained zone in sidewall during narrow gap submerged arc welding. Trans China Weld Inst 37(4):103–106
10. Guoxiang X, Jiayou W, Pengfei L et al (2018) Numerical analysis of heat transfer and fluid flow in swing arc narrow gap GMA welding. J Mater Process Technol 252:260–269
11. Ligang W, Jason C, Degala VK et al (2016) CFD simulations of GMA welding of horizontal fillet joints based on coordinate rotation of arc models. J Mater Process Technol 231:221–238
12. Lan H, Zhang H-j, Chen A-j et al (2015) Numerical simulation on dynamic process and thermal physical properties of narrow gap MAG vertical welding. Trans China Weld Inst 36(7):77–82

Kinematics Analysis of Mechanical Arm of a Ten-Joint Tunnel Arch Installation Trolley

Long Xue, Junfen Huang, Jiqiang Huang, Kang Huang, Yingyu Cao, and Wei Fang

Abstract At present, the installation of steel arch centering is still completed by manual operation of trolley mechanical arm with low degree of automation. Kinematics analysis is one of the key technologies to realize automatic installation of supporting steel arch for multi-joint and heavy-load arch-centering manipulator. Through the D–H method, the link coordinate system of the trolley manipulator was established, the transformation matrix between the joints was obtained, the forward kinematics model was established, and the initial position and pose of the grab at the end of the manipulator were determined. According to the pose requirements of arch installation for the manipulator end grips, the Jacobian matrix was reconstructed, the inverse kinematics algorithm was written, and the inverse kinematics solution of the manipulator was obtained. On this basis, the motion path planning of the manipulator was completed, and the automatics positioning of the manipulator end grips was realized. The forward and inverse kinematics algorithms of the manipulator were verified by the simulated tunnel test, and the test results show that the accuracy of arch installation meets the requirements.

Keywords Trolley mechanical arm · Forward kinematics · Inverse kinematics · Trajectory planning

1 Introduction

In recent years, with the rapid development of China's economy, China's transportation infrastructure construction has also developed rapidly. In railway construction, new requirements and tests are put forward for the mechanization and automation of tunnel construction in China. Especially, in the construction of soft surrounding rock

---

L. Xue · J. Huang (✉) · J. Huang · K. Huang · Y. Cao · W. Fang
Beijing Institute of Petrochemical Technology, 102617 Beijing, China
e-mail: huangjunfen@bipt.edu.cn

K. Huang · W. Fang
Beijing University of Chemical Technology, 100029 Beijing, China

© Springer Nature Singapore Pte Ltd. 2020

S. Chen et al. (eds.), *Transactions on Intelligent Welding Manufacturing*,
Transactions on Intelligent Welding Manufacturing,
https://doi.org/10.1007/978-981-15-7215-9_8

tunnels, in order to control the surrounding rock deformation and prevent collapse, the installation of supporting steel arches after excavation is particularly critical [1].

In the past two years, the arch installation trolley has gradually replaced the manual installation method, and the mechanization of arch installation has been initially achieved. However, most of the current installation methods are manually operated mechanical arms to achieve the installation of steel arch frames, and the degree of automation is not high [2–6]. Due to the shortcomings of low efficiency, poor accuracy, and high danger, manual operation is an urgent problem to be solved.

There are many joints (ten joints), long arm length (13 m at most), large load, and some errors in the manufacturing and installation process so the D–H parameter cannot be used in the forward kinematics modeling [7], and the numerical iteration method needs to be used in the inverse kinematics solution.

The first step to realize the automation of the mechanical arm of the gantry crane is to study its forward kinematics and inverse kinematics [8]. The research on the forward kinematics of the trolley manipulator is to find the spatial position and attitude of the end grab under the condition that the structural parameters and joint variables of each link are known so as to monitor the end position and attitude of the manipulator in real time and provide the initial position and attitude for the positioning path planning of the manipulator. Under the condition of knowing the initial position and target space position of the manipulator at the end of the manipulator, inverse kinematics reversely calculates each joint variable and ensures the manipulator moves from the known initial position to the target space position through path planning so as to provide basic data for the automatic construction of the manipulator of the arch installation trolley.

2 Mechanical Arm Structure of the Arch Installation Trolley

The structure of the mechanical arm of the arch installation trolley is shown in Fig. 1. It consists of ten joints. Joints 1–5 form the forearm, and joints 6–10 form the forearm. It should be particularly pointed out that an artificial gondola is installed at the joint 5 and the gondola should always be kept horizontal during the installation of the arch.

3 Forward Kinematics Analysis of the Mechanical Arm of Arch Installation Trolley

The forward kinematics analysis is used to determine the current spatial pose of the grab at the end of the trolley manipulator. The solution method is to establish a coordinate system at each joint. According to the connecting rod parameters of the adjacent joints, the transformation matrix of the adjacent joint coordinate system is

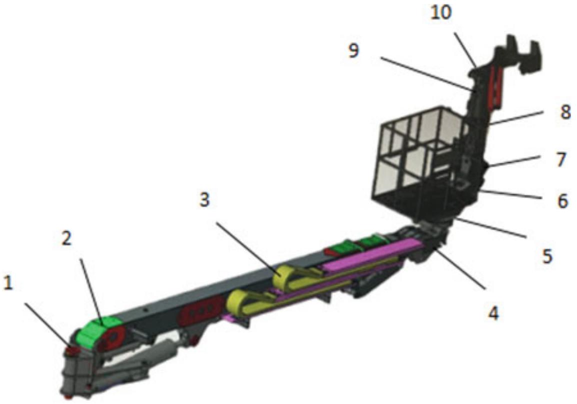

Fig. 1 Schematic diagram of mechanical arm of the arch installation trolley. 1. Boom first yaw joint. 2. Boom pitch joint. 3. Boom telescopic joint. 4. Boom secondary pitch joint. 5. Rotary joint of boom suspension. 6. Forearm pitch joint. 7. Forearm yaw joint. 8. Forearm telescopic joint. 9. Forearm secondary yaw joint. 10. Forearm grip pitch joint

obtained, and the transformation matrix of the coordinate system $\{10\}$ relative to the coordinate system $\{0\}$ is obtained by multiplication.

$$ {}^{0}_{10}T = {}^{0}_{1}T\,{}^{1}_{2}T\,{}^{2}_{3}T \ldots\ldots {}^{9}_{10}T \tag{1} $$

${}^{0}_{10}T$ is a function of ten joint variables. If the value of each joint position sensor of the manipulator, that is, the joint variable of each joint can be obtained, we can calculate the position and orientation matrix of the end grab coordinate system $\{10\}$ in the base coordinate system $\{0\}$ ${}^{0}_{10}T$.

3.1 Determination of Link Coordinate System and D–H Parameters

The mechanical arm of the arch installation trolley is an open-chain structure composed of ten joints and nine rods connected in series by joints. To perform kinematics analysis, a matrix is needed to establish the position and attitude relationship of each rod. The D–H method is a commonly used method to establish the relationship between the position and posture of the rod, which is performed in two steps.

Determination of the link coordinate system
Take the intersection of the joint axes i and $i + 1 (i = 1, 2, \ldots, 9)$ or the intersection of the common vertical line and the joint axis i as the origin of the link coordinate system $x_i y_i z_i$. The z_i-axis is specified along the joint axis i from inside to outside.

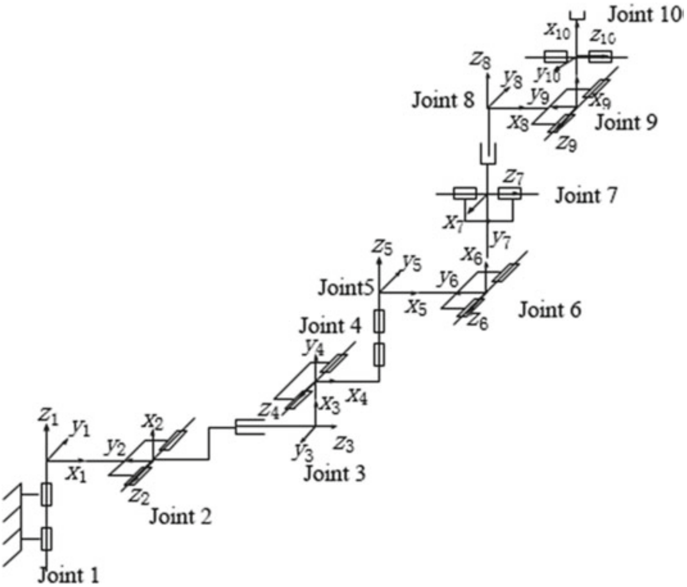
Joint 10
x_{10}
z_{10}
z_8
y_8
y_{10}
Joint 8
y_9
x_9
Joint 9
x_8
z_9
z_7
Joint 7
x_7
y_7
x_6
z_5
y_5
y_6
Joint5
x_5
z_6
Joint 6
Joint 4
y_4
z_4
x_3
x_4
z_1
y_1
x_2
y_2
x_1
z_2
z_3
y_3
Joint 3
Joint 2
Joint 1

Fig. 2 Schematic diagram of the mechanism of the arch installation robot arm

The common vertical lines of the x_i-axis and the z_i-axis and z_{i-1}-axis are merged, and z_{i-1} points to z_i. The y_i-axis is determined by the right-hand rule [8].

Based on the above principles, the link coordinate system is established as shown in Fig. 2.

Determination of the D–H parameters

According to the link coordinate system, a transformation matrix of adjacent links L_{i-1} to L_i, that is, a transformation matrix of the coordinate system $x_{i-1}y_{i-1}z_{i-1}$ to $x_i y_i z_i$, parameterized by two rotation parameters and two translation parameters: a_{i-1} means the distance from z_{i-1} to z_i along the x_{i-1}-axis; α_{i-1} means around x_{i-1}-axis, which rotates from z_{i-1} to z_i; d_i represents the distance from x_{i-1} to x_i along the z_i-axis; θ_i represents rotation from x_{i-1} to x_i around the z_i-axis angle.

Based on the above principles, the theoretical D–H parameters can be determined as shown in Table 1. Due to certain errors in machining and installation accuracy, some D–H parameters need to use actual measured values. The values in bold in Table 1 are actually measured D–H parameters, and the rest are theoretical D–H parameters.

Table 1 D–H parameters of arch installation robot arm

i	α_{i-1}	a_{i-1} (m)	d_i (m)	θ_i
1	0°	0	0	0
2	**90.3792°**	**0.33703**	0	θ_2
3	90°	0.03	**6.4833**	0
4	−90°	0.023	0	θ_4
5	**−90.4833°**	**0.67172**	**0.649**	θ_5
6	**90.1886**	**0.5978**	0	θ_6
7	90°	0.346	0	θ_7
8	90°	0	**1.04464**	0
9	90°	**0.055**	**0.13632**	θ_9
10	90°	**0.32541**	0.137	θ_{10}

3.2 Forward Kinematics Modeling

According to the D–H parameters determined above, the transformation matrix of adjacent joints can be obtained.

The general expression of ${}_{i}^{i-1}T$ is:

$$ {}_{i}^{i-1}T = \begin{bmatrix} \cos\theta_i & -\sin\theta_i & 0 & a_{i-1} \\ \sin\theta_i \cos\alpha_{i-1} & \cos\theta_i \cos\alpha_{i-1} & -\sin\alpha_{i-1} & -\sin\alpha_{i-1} d_i \\ \sin\theta_i \sin\alpha_{i-1} & \cos\theta_i \sin\alpha_{i-1} & \cos\alpha_{i-1} & \cos\alpha_{i-1} d_i \\ 0 & 0 & 0 & 1 \end{bmatrix} \tag{2} $$

Substituting the D–H parameters of the robot arm into Eq. (2), the transformation matrix of the adjacent joints of each robotic arm can be obtained as:

$$ {}_{1}^{0}T = \begin{bmatrix} \cos\theta_1 & -\sin\theta_1 & 0 & a_0 \\ \sin\theta_1 & \cos\theta_1 & 0 & 0 \\ 0 & 0 & 1 & d_0 \\ 0 & 0 & 0 & 1 \end{bmatrix} \tag{3} $$

By multiplying the ten-joint transformation matrices, the positive kinematics equation of the end gripper coordinate system of the arch-mounted trolley mechanical arm relative to the base coordinate system is:

$$ {}_{1}^{0}T\,{}_{2}^{1}T\,{}_{3}^{2}T \ldots\ldots {}_{10}^{9}T = {}_{10}^{0}T = \begin{bmatrix} n_x & a_x & o_x & p_x \\ n_y & a_y & o_y & p_y \\ n_z & a_z & o_z & p_z \\ 0 & 0 & 0 & 1 \end{bmatrix} \tag{4} $$

In the above formula, $\begin{bmatrix} n_x & a_x & o_x \\ n_y & a_y & o_y \\ n_z & a_z & o_z \end{bmatrix}$ is the attitude matrix of the end gripper relative to the base coordinate system, and among them, $\begin{bmatrix} n_x & n_y & n_z \end{bmatrix}^{\mathrm{T}}$ is the projection of the *x-axis* of the end gripper coordinate system $x_{10}y_{10}z_{10}$ in the base coordinate system $x_0y_0z_0$;$\begin{bmatrix} a_x & a_y & a_z \end{bmatrix}^{\mathrm{T}}$ is the projection of the *y-axis* of the end gripper coordinate system $x_{10}y_{10}z_{10}$ in the base coordinate system $x_0y_0z_0$; $\begin{bmatrix} o_x & o_y & o_z \end{bmatrix}^{\mathrm{T}}$ is the projection of the *z-axis* of the end gripper coordinate system $x_{10}y_{10}z_{10}$ in the base coordinate system $x_0y_0z_0$; $\begin{bmatrix} p_x & p_y & p_z \end{bmatrix}^{\mathrm{T}}$ is the position in the coordinate origin of the end gripper coordinate system $x_{10}y_{10}z_{10}$ in the base coordinate system $x_0y_0z_0$.

According to the positive kinematics model, given each joint variable, the position and attitude matrix of the end gripper coordinate system relative to the base coordinates can be calculated, thereby completing the forward kinematics solution of the end gripper of the robot arm of the arch installation trolley.

4 Inverse Kinematics Solution of Mechanical Arm for Arch Installation Trolley

Inverse kinematics [9–11] is used to determine the joint variables of the manipulator's end gripper when it is in the target's spatial position and pose, which provides the basic data for the manipulator's moving path planning.

Since each arm of the arch installation trolley has ten joints and 3D space has six degrees of freedom, the arm is redundant [12], and there is no unique solution to its inverse kinematics. Therefore, according to the actual situation (the basket is installed at the joint 5, and the horizontal direction is always required during the movement), the whole mechanical arm is divided into a boom and a forearm, the boom is composed of 1–5 joints, and the forearm is composed of 6–10 joints as shown in Fig. 3.

4.1 Inverse Kinematics Analysis of Forearm

Due to the length of the arm, the whole arm will produce a certain deflection during the installation of the arch frame, resulting in a certain deviation between the actual arrival of the end and the theoretical calculation. In order to reduce the deflection, it is stipulated that the forearm is always vertical to the boom during the working process; that is, the two pitch joint variables of the *jib* are 0. For the second adjustment, the starting value of the telescopic joint variable of the forearm is also 0. The two joint variables can be determined by the given end pose. At this point, the arm shape of

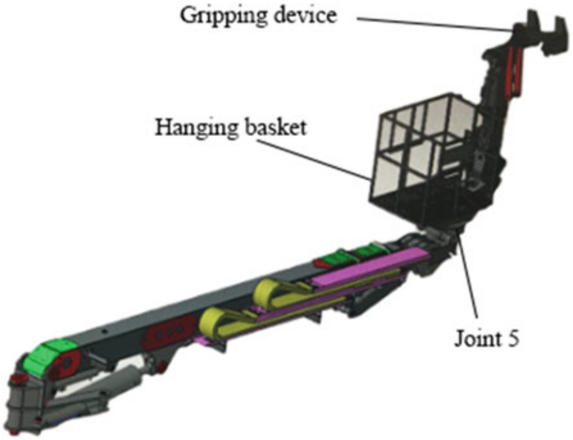

Fig. 3 Schematic diagram of arch installation mechanical arm

the small arm is relatively fixed, then the end pose of the big arm can be determined, and the inverse kinematics of the big arm can be solved.

4.2 Inverse Kinematics of Boom

Due to the fact that the D–H parameters of the boom are mostly measured in the process of forward kinematics modeling, the joint transformation matrix will appear multivariate multiple terms which cannot be eliminated in the calculation, so the inverse kinematics of the boom cannot be solved analytically. In this paper, the Jacobian method of vector product is used to solve the approximate analytical solution of the boom through iteration.

The basket is installed at the fifth joint of the boom. During the working process, the basket must be level. Therefore, in this paper, in order to calculate the inverse movement time of the large arm, it is necessary to reconstruct the Jacobian matrix of position and add the constraints of two sets of joint variables, even if the two yaw joints (one joint and five joints) and two pitch joints (two joints and four joints) of the large arm are linked.

Original position Jacobian matrix J:

$$v \cdot t = J \cdot q = J_1\theta_1 + J_2\theta_2 + J_3\theta_3 + J_4\theta_4 + J_5\theta_5 \tag{5}$$

Reconstruct the Jacobian matrix: Let $\theta_1 = -\theta_5$, $\theta_2 = -\theta_4$ and get a new Jacobian matrix J:

$$v \cdot t = J \cdot q = (J_1 - J_5)\theta_1 + (J_2 - J_4)\theta_2 + J_3\theta_3 \tag{6}$$

$$J = [J_1 - J_5 \quad J_2 - J_4 \quad J_3]_{3\times 3} \tag{7}$$

After the above transformation, the Jacobian matrix becomes a 3×3 matrix, which ensures the attitude of the terminal on the premise of ensuring the position of the terminal.

4.3 Inverse Kinematics Solution of Boom

1. Construction of Jacobian Matrix by Vector Product Method

According to the vector product method to construct the Jacobian matrix, the Jacobian matrix of the large arm can be obtained as follows:

$$J = \begin{bmatrix} Z_1 \times {}^1p_5 & {}^0Z_2 \times {}^2p_5 & {}^0Z_3 & Z_4 \times {}^4p_5 & {}^0Z_5 \times {}^5p_5^0 \\ Z_1 & Z_2 & 0 & Z_4 & Z_5 \end{bmatrix} \tag{8}$$

In the above formula, the upper three lines of the matrix are the position Jacobian matrix, and the lower three lines are the attitude Jacobian matrix. In this paper, the position Jacobian matrix is rebuilt to solve the inverse movement of the boom. By adding joint linkage constraints, the end position and attitude of the boom are guaranteed at the same time. Therefore, the attitude Jacobian matrix is no longer needed.

In this matrix, $z_i (i = 1, 2, 3, 4, 5)$ is the unit vector of the coordinate system $x_i y_i z_i (i = 1, 2, 3, 4, 5)$, and $i_{p_s^0}$ is the representation of the origin of the boom end coordinate system $x_5 y_5 z_5$ in the base coordinate system $x_0 y_0 z_0$ with respect to the coordinate system $x_i y_i z_i (i = 1, 2, 3, 4, 5)$.

2. Trajectory Planning

In order to move the manipulator from the starting position to the ending position determined by the forward kinematics analysis, a motion track needs to be planned. The track is interpolated into several parts, and each interpolation distance has a starting point and an ending point. The inverse solution from the given starting and ending position, i.e., each joint variable, is obtained by solving the inverse solution on each distance and summing up each inverse solution. The value of interpolation copies will affect the accuracy and speed of inversion. If the number of copies is too small, the accuracy will be reduced. If the number of copies is too large, the number of cycles will increase and the speed of inversion will be reduced.

Specify uniform linear movement of the end of the mechanical arm. The straight line is interpolated into several parts so that the end of the mechanical arm moves in a uniform straight line on each section [13, 14].

The interpolation length of each segment is calculated according to the starting position (x_0, y_0, z_0) calculated by the forward kinematics and the given ending position (x_1, y_1, z_1):

$$\Delta l = \left(\Delta x^2 + \Delta y^2 + \Delta z^2\right)^{1/2} / n \tag{9}$$

In the above formula, $\Delta x = x_1 - x_0$, $\Delta y = y_1 - y_0$, $\Delta z = z_1 - z_0$, n is interpolation number.

And define the direction vector of the line: $s = (\Delta x, \Delta y, \Delta z)$.

Thus, the joint variables corresponding to the movement of the end of the manipulator from the start point to the end point can be calculated for each interpolation distance q:

$$q_i = J_{i5\times3} \cdot s \cdot \Delta l \tag{10}$$

After each cycle, the joint variable on the corresponding interpolation distance can be obtained. The joint variable of n times can be summed; that is, the total joint variable q from the given initial position to the end position of the manipulator can be obtained; that is, the inverse kinematics of the boom can be solved.

$$q = \sum_{i=1}^{n} q_i \tag{11}$$

5 Verification of Forward and Inverse Kinematics of Manipulator

The forward and inverse kinematics algorithms are programmed by MATLAB, and the experiment was carried out in the simulation tunnel. Variables of each joint were solved by the theoretical position of the end of the manipulator (x_{10}, y_{10}, z_{10}). The error between the actual and theoretical positions of the end of the manipulator is within 5 cm (Table 2), which meets the accuracy requirements of the arch installation.

Table 2 Errors of arch installation between the actual and theoretical positions (unit: m)

Order	Coordinate	Theoretical value	Actual value	Error
1	x_{10}	6.6035	6.6382	0.04
	y_{10}	−2.9903	−2.9486	
	z_{10}	3.4027	3.4161	
2	x_{10}	7.0983	7.1302	0.0478
	y_{10}	−3.0181	−3.0454	
	z_{10}	1.0609	1.0628	
3	x_{10}	7.1431	7.1612	0.0464
	y_{10}	−3.2265	−3.1924	
	z_{10}	−1.2374	−1.2632	

6 Conclusion

In this paper, the D–H method was used to establish the link coordinate system for the robot arm of the tunnel arch installation trolley, and the parameters of each link of the robot arm were actually measured. The forward kinematics model was solved, and the initial space pose of the manipulator end gripper was determined. According to the actual working situation of the manipulator, the ten joints were grouped and integrated. In the inverse kinematics solution, the Jacobian matrix was reconstructed and the trajectory planning was performed to complete the inverse kinematics solution. The forward and inverse kinematics algorithms were developed by MATLAB. Experiments were performed in a simulated tunnel to ensure that the end of the robot arm moves straight to the target position at a uniform speed, verifying the correctness of forward and inverse kinematics.

Acknowledgements This work is supported by the National Key Research and Development Program of China (2018YFB1306900) and project jointly supported by the Beijing Natural Science Foundation and Beijing Education Commission (KZ201810017022).

References

1. Pu Q, Luo K (2012) Technical research on the installation of tunnel arches. Constr Mechanization 33(07):51–53+8
2. Luo K, Guan H, Pu Q (2012) Forward kinematics research and workspace simulation of arch mounting robot. Constr Mach 43(04):29–33+7–8
3. Xiong :L (2012) Research on key technology of steel arch mounting manipulator. Zhengzhou University, Zhengzhou
4. Zhang M, Wang L (2018) Overview and development trend of arch brakes at home and abroad. Construction Machinery Technology & Management 31(03):73–77
5. Zhu C, Xu Y (2009) Construction points of tunnel steel arch support. West Explor Eng 21(S1):245–246
6. Kang B (2011) A new type of arch installation machine for tunnel construction. Tunnel Constr 31(05):624–628+642
7. Denavit J, Hartenberg RS (1955) A kinematic notation for lower-pair mechanisms based on matrices. J Appl Mech 22(2):215–221
8. Craig John J (2006) Introduction to robotics mechanics and control. Mechanical Industry Press, Beijing
9. Ren X, Li H (2016) Modeling kinematics comparison of complex multi-joint manipulators. J Jilin University (Information Science Edition) 34(06):753–760
10. Rui T, Gong L, Qiao Y (2001) Motion relationship and attitude analysis of excavator working device. Mod Mach 03:56–58
11. Zhan C (2013) Research on design and motion control of steel arm mounting robot. Henan University of Science and Technology, Luoyang
12. Gao H, Zhang M, Zhang X et al (2017) Kinematics analysis of seven degrees of freedom manipulator. Mod Manuf Eng (08):29–33+77

13. Zhao B, Liu J, Wang Y (2008) Robot planning control of engineering machinery working device. Mach Electron 06:26–28
14. Liu Y, Huang T (2012) Inverse kinematics analysis and trajectory planning of 6R manipulator. J Mech Eng 48(03):9–15

Research of Multi-source Information Sensing Technology in Defect Detection on Automatic Welding

Dapeng Yang, Junfeng Han, Na Lv, and Zhiqiang Feng

Abstract As one of the key technologies of large-scale machinery construction, welding technology has been attached great importance to by shipbuilding enterprises all over the world. With the general progress and development of welding intelligent automation technology, most of the welding work in simple operating environment is gradually transformed from manual operation to welding robot. Through the integration of automation to operate it, so the detection of welding quality is also an important part. Because of the complex physical and chemical reactions in the welding process, a variety of information sources can be extracted for analysis and identification. In the process of robot welding, the accurate extraction and analysis of the effective feature information in the dynamic process of welding are an effective guarantee for the automation and intelligence of welding. In this part, the detection of weld defects can help the welding quality from another aspect. Through the real-time monitoring and analysis of defects, the corresponding features can be extracted to the penetration of the dynamic process of welding. Status provides reference significance.

Keyword Welding automation · Defect detection · Multi-source information · Real-time monitor · Sensing technology

---

D. Yang · J. Han
School of Electrical and Information Engineering, Guangxi University of Science and Technology, Liuzhou 545000, China

N. Lv (✉)
Department of Information Detection and Instrument, Shanghai Jiao Tong University, Shanghai 200240, China
e-mail: nana414526@163.com

D. Yang · J. Han (✉) · Z. Feng
School of Mechanical and Marine Engineering, Beibu Gulf University, Qinzhou 535000, China
e-mail: hanjf@139.com

© Springer Nature Singapore Pte Ltd. 2020

S. Chen et al. (eds.), *Transactions on Intelligent Welding Manufacturing*,
Transactions on Intelligent Welding Manufacturing,
https://doi.org/10.1007/978-981-15-7215-9_9

1 Introduction

The information extracted from welding dynamic process includes vision, spectrum, arc sound, temperature and gas, among which the extraction and analysis of visual information are the most mature and widely used research method. The visual information has the characteristics of intuitionistic real time, and the research technology is increasingly mature; the extraction and analysis of spectral information are also rich in information, which is also commonly used. The arc sound is produced by the action between the arc and the molten pool during welding, which contains the stable information of welding quality and rich monitoring information, and has gradually become the hot spot of welding information detection; the research progress in this field is slow because of the complex operating environment ratio and the lack of precise detection equipment, which leads to the lack of practical research. The research results of above can significance reflect the theoretical hypothesis.

The evaluation of welding quality is based on the degree of weld penetration. It is interfered by many factors in the process of welding, and there will be defects such as incomplete penetration, depression, crack and so on. Visual sensing is the most promising and common sensing method because of its rich and intuitive information and the characteristics of imitating human visual behavior. Defect recognition of molten pool image is also one of the applications of vision sensing technology.

With the rapid development of information technology and electronic industry, optical CCD device has become an important core device of welding process information monitoring. The sensor uses the sensitive characteristics of CCD in visible or invisible band to image. It does not participate in the welding circuit and does not affect the welding process, and the required hardware is simple and easy to maintain. At the same time, it is helpful for the research progress of weld pool defect identification.

In Ref. [1], CCD vision sensor system is used to track and collect the information in the welding process, and a fusion pool image segmentation method based on fuzzy c-means clustering collaborative active contour model is proposed. In Ref. [2], a monocular passive vision image acquisition system for GMAW arc spectrum features is designed (Fig. 1). The average gray value of the image is used to judge the interference degree of arc light on the image of the weld pool, and the threshold setting in the wavelet transform modulus maximum edge detection algorithm is limited to extract the weld pool contour and feature coefficient. According to the characteristics of weld pool image noise, a weld pool image with clear features is obtained by improving the filtering algorithm and bilinear interpolation algorithm. The characteristic parameters of weld pool are obtained by thresholding segmentation, and the pattern recognition of common weld defects is realized. In Ref. [3], passive vision sensing technology is reconstructed on welding robot, CCD vision sensor and narrow light filter are equipped to collect image information of molten pool with a small amount of stray light, and image information collected in CO_2 gas shielded welding is preprocessed. It is found that Canny operator with threshold value of [0.1, 0.5] can extract image information of molten pool edge more than wavelet multi-scale in processing molten

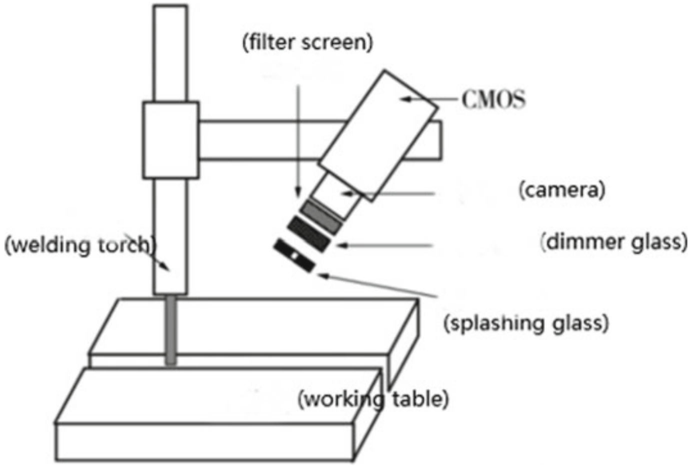

Fig. 1 Schematic diagram of visual sensing system [2]

pool edge. Edge image information is more suitable. In Ref. [4], a molten pool image shooting system based on a new photosensitive technology—LinLog technology—is established, which can overcome the interference of strong arc light in the process of shooting molten pool image and obtain a clear and complete molten pool image, so as to detect the defect characteristics of the weld more accurately.

The detection of welding defects by means of weld pool image mostly relies on CCD optics to collect image information, and different algorithms are proposed to extract feature information for comparative analysis. With the development of intelligent technology and intelligent image extraction, the feature information extraction technology of molten pool defect will be more perfect.

2 Ultrasonic Testing Technology

As a rapid and effective method of welding defect detection, the detection technology based on sound sensor has been widely used in welding automation, which provides corresponding support for the guarantee and improvement of welding quality. With the development of computer technology and artificial technology, the detection technology will be further combined with information processing and automatic control, and the welding defect detection technology based on sound will get faster development [5].

Ultrasonic non-destructive testing technology is to use the principle of ultrasonic propagation and reflection, to send laser to the target, through the calculation and analysis of the echo shape and speed to obtain the appearance and shape of the tested object. In the process of welding, ultrasonic testing technology can get rid of the limitation of the environment and can detect the accuracy of the welding process in a timely and comprehensive manner to detect whether there are welding defects [6]. In the detection technology of welding defect, ultrasonic detection is also one of the more commonly used methods. Because of its real-time and high accuracy, it is also a hot spot to study the welding quality, but the degree of combination with welding automation still needs to be developed.

In Ref. [7], the ultrasonic flaw detection technology is used to detect the defects of plug weld (Fig. 2). By analyzing the characteristics of conventional echo map, the possible defects in plug weld are identified and judged. Literature [8] developed and established a high-frequency ultrasonic scanning system platform, which realized high-precision mechanical scanning, high-frequency ultrasonic receiving and sending, high-speed acquisition and imaging of full-wave data. It can directly find small defects such as weld porosity and significantly improve the detection of welding defects. In Ref. [9], the influence of welding defects on ultrasonic passing through the welding joint was studied, and the sensitivity of welding parameters was determined to be related to the frequency of ultrasonic conduction excitation. In Ref. [10], the ultrasonic phased array detection technology is used to conduct intuitive qualitative and quantitative analysis of arc welding defects, and the full-wave acquisition is realized. The detection image is combined with the actual workpiece geometry information to more effectively find the welding defects.

Ultrasonic testing technology is often used to detect the internal defects of welding structures, which has the advantages of wide detection range, deep, fast transmission speed, harmless to people and convenient operation. It is the focus of most researchers at home and abroad and has done a lot of research work. But there are also many difficulties to be overcome, such as real-time detection of welding quality and avoiding defects, and better integration with welding automation.

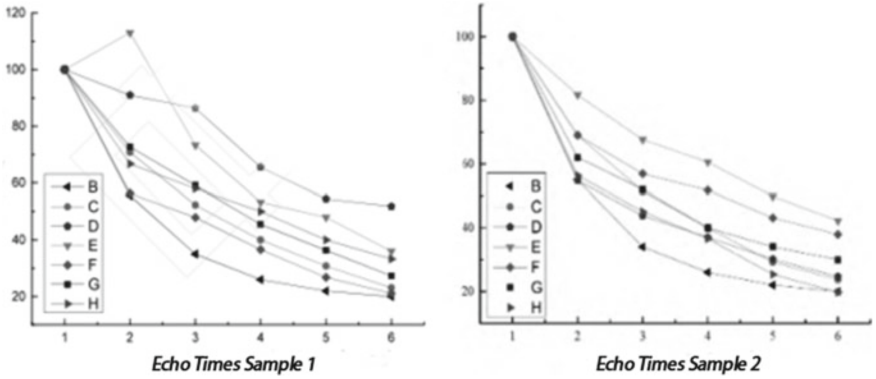

Fig. 2 The ultrasonic flaw detection technology is used to detect the defects of plug weld

3 Spectrum Detection Technology

In the process of welding, many kinds of light radiation signals are often generated. Different types of light signals are collected by different types of photoelectric sensors, and then all kinds of light signals are sorted into light spectrum. Then, the content of various chemical elements generated during the weld can be collected and analyzed in order to define the welding quality. The defect state could be identified according to the principle of spectrum detection technology [11].

In Ref. [12], the high-dimensional signals collected by the spectrometer are input into the data-driven software based on the stack automatic encoder, and the algorithm automatically extracts obvious features to realize the real-time detection of welding defects. Particle swarm optimization algorithm is used to optimize the algorithm, so as to enhance the ability of extracting feature parameters from the original data and provide an effective algorithm software for the real-time detection of high-power disk laser welding. In Ref. [13], the spectrum diagnosis of aluminum alloy laser arc composite weld defects is carried out (Fig. 3a, b). Based on the principal component analysis and threshold segmentation method, the data extraction and redundant information elimination are realized. The main information of aluminum alloy composite welding spectrum is found, which proves that the spectrum diagnosis technology can effectively detect the weld crack sensitivity and element burn rate. In Ref. [14], an experimental platform for automatic spectrum information collection of welding process was built to detect the porosity defects in aluminum alloy pulsed GTAW process, and the spectrum signal of arc was collected and processed in real time. A spectrum sensing system based on linear CCD was developed. Literature [15] collected spectral radiation information during laser welding by spectrometer and studied the influence of different elements on welding quality. It was found that in the spectral range of different wavelengths, Fe, Cr, S, C and other elements had a certain correlation with the variation of welding quality. In Ref. [16], an on-line detection method for welding defects of robot aluminum alloy based on random forest and optimal feature subset is proposed, which can select effective spectral features from high-dimensional arc spectrum, improve defect recognition accuracy and have better recognition rate compared with RBF model and BP model.

Spectral detection technology has been widely used in welding quality, with the characteristics of simple operation, qualitative analysis, good selectivity and high sensitivity. It has been used by many researchers to analyze the welding penetration state and also used in some welding automation projects, but it also has limitations, such as the analysis needs to be based on relative comparison. A set of standard samples must be used as the basis for quantitative analysis, and the evaluation results are easily affected by the matrix. There are still some difficulties to be solved by researchers.

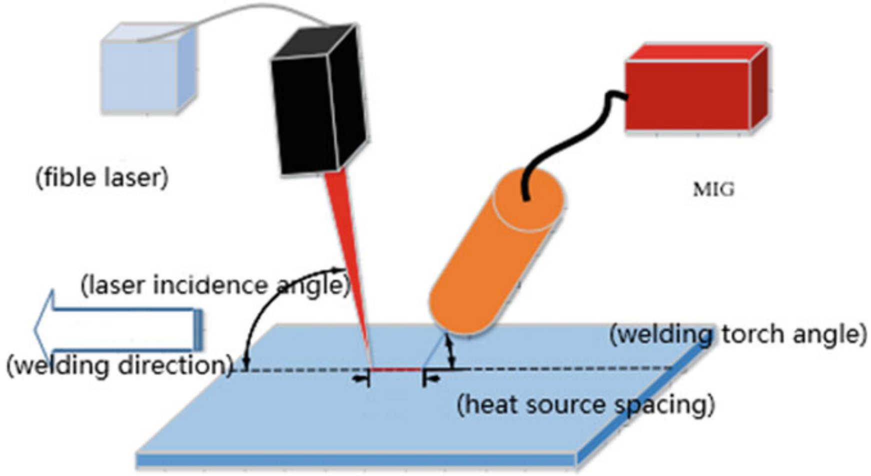
(fible laser)
MIG
(laser incidence angle)
(welding torch angle)
(welding direction)
(heat source spacing)

(a) Schematic diagram of process test during composite welding

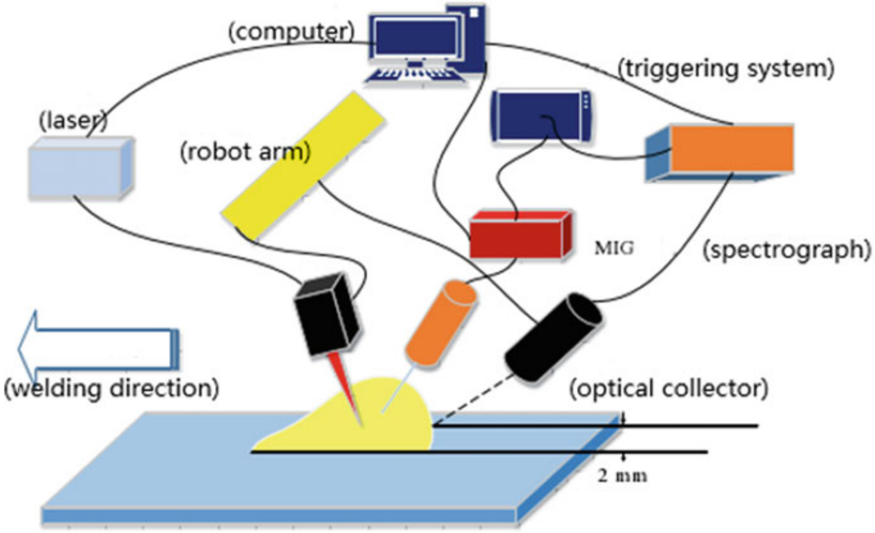
(computer)
(triggering system)
(laser)
(robot arm)
MIG
(spectrograph)
(welding direction)
(optical collector)
2 mm

(b) Schematic diagram of plasma spectrum information collection method in welding process

Fig. 3 Spectrum signal acquisition system (from Ref. [13])

4 Magneto-Optic Imaging Detection Technology

Magneto-optical imaging technology is a new visual non-destructive testing technology based on Faraday magneto-optical effect. Its principle is to use alternating magnetic field to excite the layer eddy current of the tested weldment. Through magneto-optical imaging to detect the normal magnetic field caused by the welding defect, the magneto-optical image of the defect can be obtained. It has high sensitivity, high speed, easy to realize automation and high reliability (Fig. 4). In recent years, magneto-optical imaging technology has been used in the detection of micro-gap welds, and the detection accuracy can be less than 0.1 mm [17].

In Ref. [18], the method of two-dimensional discrete Fourier transform is applied to the magneto-optical image of laser welding crack, and the checking calculation and experimental verification are carried out. The spectrum data of laser welding crack under different excitation intensity is obtained. After analysis, it shows that the frequency domain of the magneto-optical image of laser welding crack has a certain corresponding relationship with the characteristics of space domain. Literature [19] takes laser welding low-carbon steel plate as the test object, uses constant magnetic field and 50 Hz alternating magnetic field to excite the welding defects, obtains the real-time magnetic field distribution in the defect area and finds that compared with constant magnetic field excitation, the information obtained by alternating excitation is more accurate and complete. In Ref. [20], the MFL feature of magneto-optical imaging under the excitation of alternating magnetic field is applied to the contour reconstruction of welding defects, the MFL reconstruction model is established, and the data obtained by numerical simulation method is used for verification. The results show that the image data of MFL feature of magneto-optical imaging can realize the two-dimensional contour reconstruction of welding defects.

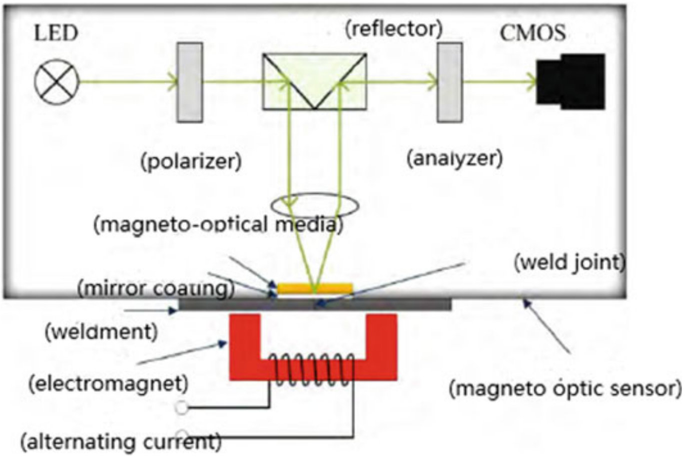

Fig. 4 Schematic diagram of seam magneto-optical imaging (from Ref. [17])

In Ref. [21], a new method of non-destructive detection of welding defects based on the principle of magneto-optical imaging is studied, which extracts the features of micro-welding defects on the surface of high-strength steel, trains and recognizes the welding defects according to adaBoost classification algorithm and constructs the features to automatically recognize the magneto-optical image. In Ref. [22], the magnetization rule of weld crack under alternating magnetic field is explored for the weld crack of carbon steel (Q235), and the simulation experiment of the weld magneto-optical imaging non-destructive testing under alternating electromagnetic field excitation is carried out. It is found that the light intensity map obtained by magneto-optical imaging sensor will not have a large difference in magnetic induction intensity due to the different starting point of sampling. According to the characteristics of defect magneto-optical image, a method of welding defect detection based on the texture features of magneto-optical image is proposed in Ref. [23]. The image features are extracted by GLCM, and then the features of magneto-optical image are further extracted by Gabor transform. A defect classification model based on SVM is constructed.

As a new detection technology, magneto-optical imaging technology has obvious advantages in welding defect detection, and it is easy to realize automatic construction, so it has great development space in welding real-time detection. In the same way, magneto-optical imaging also has corresponding short plates, such as only applicable to magnetic materials, and the results are easily affected by the light path of the light source. It is still necessary for scholars to further study its characteristics and further improve the corresponding detection technology optimization.

5 Development Trend

To sum up, with the development of industrial technology, the detection technology of welding multi-source information defects depends on the continuous progress of various sensor performance and the continuous improvement of corresponding information extraction and analysis algorithm. Its prospect is very considerable, but there are also many difficulties to be overcome, such as the realization of welding automation, real-time detection of welding penetration status, and whether there are defects in the weld. The new defect detection technology comes into being with the continuous exploration of various kinds of information, such as magneto-optical imaging detection and magnetic flux leakage detection, but it still needs to be improved to improve the reliability of welding automation.

Acknowledgements This work is supported by the National Natural Science Foundation of China under the Grant No. 51975367, 61401275 and the Chine Postdoctoral Fund No. 2016M601588 and No. 2017T100295 and the Startup Fund for Youngman Research at SJTU (SFYR at SJTU) No. 18X100040049.

References

1. Fang J, Wang K, Huang Y (2019) Image recognition of weld pool during the formation of high-speed GMAW hump weld bead. J Weld 40(2):42–46
2. Zhu Y, Wu Z, Wang A, Li L (2018) Research on welding defects based on the contour characteristics of GMAW weld pool. Electric Weld Mach 41(11):13–18
3. Zhao B (2014) Feature recognition of CO_2 welding defects based on molten pool vision. Guangxi University of Science and Technology, Guangxi
4. Li M (2011) Research on image acquisition system of molten pool based on linlog photosensitive technology. In: 16th National Welding academic conference proceedings of Chinese society of mechanical engineering, pp 162–166
5. Chi D, Qi C (2018) Review on acoustic nondestructive testing of welding defects in China. Precis Form Eng 9(1):74–81
6. Wang L (2019) Application analysis of ultrasonic nondestructive testing technology in metal material welding. Nanfang Agric Mach 49(15):135
7. Liu B, Yue F, Ren X, Chen S, Cao J (2019) Research on defect assessment method of plug welding ultrasonic flaw detection. Prog Build Steel Struct 20:17
8. Lu H, Xing L, Zhao X (2014) High frequency micro ultrasonic visual scanning inspection of welding defects. Welding 3(9):19–23
9. Ochoa P (2019) Villegas Irene Fernandez, groves Roger m, Benedictus rinza. diagnostic of manufacturing defects in extremely well-developed thermoplastic composite joints using ultrasonic guided waves. NDT & E International, p 107
10. Xing L, Lu H (2014) Research on ultrasonic phased array detection technology for arc welding defects. Welding 3(11):59–62
11. Jiang W, Fan J, Liu D, He G (2017) Characterization method of laser welding defects based on spectral analysis. Ind Instrum Autom Device 46(5):13–15
12. Zhang Y, Gao X, You D, Zhang N (2019) Data-driven detection of laser welding defects based on real time spectrumeter signals. IEEE Sens J 19:20
13. Hu Y (2017) Spectral diagnosis of defects in laser arc hybrid welding of aluminum alloy. Huazhong University of Science and Technology, Hubei
14. Huang Y (2017) Study on the characteristics of hydrogen pore formation and compensation control method of aluminum alloy AC GTAW based on arc spectrum information. Shanghai Jiaotong University, Shanghai
15. Jiang W, Fan J, Liang Z, He G (2017) The relationship between element spectral information and weld quality in laser welding. J Test Technol 31(5):448–454
16. Zhang Z, Yang Z, Ren W, Wen G (2019) Rabdom forest-based real-time defect detection of Al AIIOY in mechanical arc welding using optical specification. J Manuf Processes 42:51–59
17. Gao X, Lan C, Chen Z, You D, Li G (2017) Dynamic detection and identification of welding defects by magneto-optical imaging. Opt Precision Eng 25(5):1135–1141
18. Du L, Gao X, Zhang N, Ji Y (2019) Frequency domain characteristic analysis of magneto-optical imaging of laser welding cracks. Laser Technol 42(5):10
19. Ma N, Gao X, Zhou X, Zhang Y (2018) Characteristic analysis of magneto-optical imaging of welding defects under magnetic field excitation. Laser Technol 42:525–530
20. Gao X, Zhou X, Li Y, Dai X, Zhang N (2019) The application of magneto-optical imaging magnetic flux leakage characteristics in the reconstruction of welding defect contour. Opt Precision Eng 27:1863–1869
21. Gao X, Xie Y, Chen Z, You D (2017) Fractal feature detection of high strength steel welding defects by magneto-optical imaging. J Weld 38(7):1–4
22. Ma N, Gao X, Dai X, Zhang N (2019) Magnetic field simulation and magneto-optical imaging detection of welding cracks. Opt Precis Eng 40(9):077–081
23. Lan C, Gao X, Ma N, Zhang N (2018) GLCM Gabor recognition method for texture characteristics of magneto-optical imaging of welding defects. J Weld 39(6):096–099
24. Wang Y, Gao D, Liao M (2003) Application status and development of NDT technology in welding field. NDT 25(3):140–142

25. Tian W (2017) Research on pattern recognition algorithm and real-time detection system of welding defects based on infrared vision. Huazhong University of Science and Technology, Hubei
26. Sun Z, Li H, Tao W (1992) Computer pattern recognition of welding defects. Nondestr Test 14(9):241–243
27. Gao X, Du L, Ma N (2019) Magnetio-optical imaging characteristics of well defects under alternation and rotating magnetic field exception. Options Laser Technol 112:188–197
28. Li Y, Gao X, Zheng Q (2019) Weld cracks nondestructive testing based on magneto optical imaging under alternative magnetic field exemption. Sens actors A-PHYSICAL 285:289–299
29. Gao X, Li G, Chen Z (2018) Modeling for detecting well defects based on magneto optical imaging. Appl Options 57(21):6110–6119
30. Gao X, Ma N, Du L (2018) Magnetio optical imaging characteristics of well defects under alternative magnetic field exemption. Options Express 26(8):9972–9983
31. Gao X, Lan C, You D (2017) Welding nondestructive testing using magnetic optical imaging induced by alternative magnetic field. J Nondestr Eval 36(3):55
32. Lv N, Xu Y, Zhang Z et al (2013) Audio sensing and modeling of arc dynamic characteristic during pulsed Al alloy GTAW process. Sens Rev 33(2):7
33. Lv N, Xu Y, Zhong J et al (2013) Research on detection of welding penetration state during robotic GTAW process based on audible arc sound. Ind Rob Int J 40(5):8–18
34. Lv N, Zhong JY, Chen HB et al (2013) Penetration feature extraction and modeling of arc sound signal in GTAW based on wavelet analysis and hidden Markov model. In: IEEE International Symposium on Industrial Electronics (ISIE). IEEE, pp 1–6
35. Lv N, Xu YL, Li SC, Chen SB (2017) Automated control of welding penetration based on audio sensing technology. J Mater Process Technol 250:81–98
36. Lv N, Fang G, Zhao H, Chen S, Zou J (2016) Real-time monitoring of welding path in pulse metal-inert gas robotic welding using a dual-microphone array. Int J Adv Manuf Technol 90(9–12):1–14
37. Lv N, Zhong J, Chen H, Lin T, Chen S (2014) Real-time control of welding penetration during robotic GTAW dynamical process by audio sensing of arc length. Int J Adv Manuf Technol 74(1–4):235–249
38. Lv N, Xu Y, Zhang Z, Wang J, Chen B, Chen S (2013) Audio sensing and modeling of arc dynamic characteristic during pulsed Al alloy GTAW process. Sens Rev 33(2):141–156
39. Lv N, Xu Y, Zhong J, Chen H, Wang J, Chen S (2013) Research on detection of welding penetration state during robotic GTAW process based on audible arc sound. Ind Robot Int J 40(5):474–493
40. Lv N, Zhong J, Wang J, Chen S (2014) Automatic measuring and processing system of audio sensing for real-time arc height control of pulsed GTAW. Sens Rev 34(1):51–66 [Outstanding Paper Award Issued by Emerald Literati Network, An International Award (SCI index, IF: 1.2769)]

Short Papers and Technical Notes

Research on Resonant High-Voltage Plasma Power Supply

Zixin Hu, Song Yuan, Zhuoran Wang, and Min Zeng

Abstract In view of the shortcomings of traditional high-voltage plasma power supply, such as large volume, complicated circuit, and poor control precision, this paper proposes a high-voltage plasma power supply with embedded control system. In this work, the working principle of circuit is firstly introduced, and a main circuit model with MATLAB/Simulink is built so as to analyze the working process in circuit. In addition, the structure of control system and the programmed control flowchart are addressed in detail. Finally, a prototype with output voltage of 15 kV and output current of 200 mA is built to verify the validation. The result shows that the experimental waveform is consistent with the simulation waveform, which can meet the actual requirements.

Keywords Resonance · Soft switching · MATLAB–Simulink · High voltage · Plasma

1 Introduction

Most of the early power supplies are linear with low efficiency about 35%; moreover, a large area of heat sink as a cooling condition is required to solve the problem of high temperature. Besides, since the linear power supply operates at power frequency of 50 Hz, the transformer is too big to place in applications where space is limited. Therefore, a high-voltage plasma power supply is built based on the resonance principle, so as to solve the problems of large volume, complex circuit, poor stability, and low efficiency of traditional power supply [1]. The high-voltage plasma power supply is a digital power supply in core of digital chip that has characteristic of

---

Z. Hu · S. Yuan · Z. Wang · M. Zeng (✉)
School of Mechanical and Automotive Engineering, South China University of Technology, Guangzhou 510641, China
e-mail: memzeng@scut.edu.cn

M. Zeng
National Defense Key Disciplines Laboratory of Light Alloy Processing Science and Technology, Nanchang Hangkong University, Nanchang 330063, China

© Springer Nature Singapore Pte Ltd. 2020

S. Chen et al. (eds.), *Transactions on Intelligent Welding Manufacturing*,
Transactions on Intelligent Welding Manufacturing,
https://doi.org/10.1007/978-981-15-7215-9_10

strong expandability and flexibility. In the benefit of high level of integration of digital power supply, less peripheral circuits are required compared with the traditional analog power supply with strong anti-interference so that the high precision can be kept even under the complicated working conditions. At present, high-voltage plasma power supplies are widely used in the field of cleaning screen, plasma arc welding, plasma ball-milling treatment, and plastic surface corona treatment with high research value.

The improvement and application of plasma power are paid much attention in foreign country. Scholtz [2] designed an asymmetric pulsed bipolar power supply to generate low-temperature plasma, which can maintain stable running during a wide range of operating parameters. In the application of Sewage treatment, Supanarapan [3] made a high-voltage plasma power supply performing excellent in processing sewage with an output voltage up to 25 kV. In addition, it is found that the quality of coating in plasma spraying is directly proportional to the power, validating the importance of high-voltage plasma power supply [4].

In order to achieve the lightweight, high efficiency, and provide a good human interaction interface, this paper studies the resonant high-voltage plasma power supply with embedded circuit control. The structure of the thesis is as follows. The working principle of the high-voltage plasma circuit is introduced in the second part of the article. The third part is implemented in Simulink/MATLAB environment, which simulates the main circuit of the high-voltage plasma power supply and analyzes its output waveforms. The fourth part designs the control circuit and makes the high-voltage plasma power supply prototype with output of 15 kV/200 mA. In this part, the reliability of the prototype was verified by comparing the consistency of the simulated waveform with the experimental waveform of the power supply. Conclusion is the last part of the article.

2 The Principle of High-Voltage Plasma Circuit

The block diagram of the high-voltage plasma power supply is shown in Fig. 1. The main circuit consists of a rectifying and filtering circuit, a resonant converter, and a high-frequency transformer.

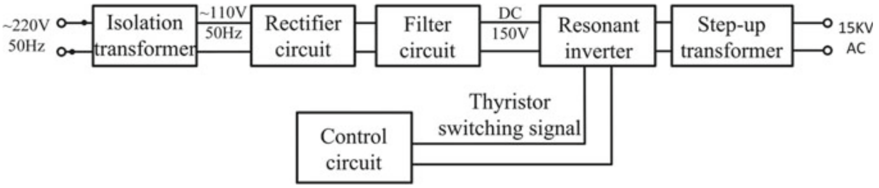

Fig. 1 Block diagram of high-voltage plasma power supply

220 V AC voltage is stepped down to 110 V AC voltage through isolation transformer, which achieves electrical isolation, thus improving safety and reliability. The obtained 110 V AC is a sine wave, which needs to be rectified and filtered to smooth the DC voltage, and its output is 150 V DC voltage.

Zero-current-switching resonant converter [5] is also the main core of this high-voltage plasma power supply. Its function is to change the front 150 V DC voltage output into sinusoidal waveform through the resonant network, realizing resistive network resonance by controlling the switching-on frequency, and obtain several times of the input voltage on the resonant element. Finally, the obtained high voltage is further increased to about 15 kV AC voltage through a step-up transformer, which is supplied to the load side for high-voltage plasma gas. The control circuit provides driving signals for the resonant circuit to control the ON-OFF state of the switch.

3 Main Circuit Simulation of High-Voltage Plasma Power Supply

3.1 Modeling Based on MATLAB–Simulink

As shown in Fig. 2, the structure of the main circuit consists of 220 V AC power supply, 220 V/110 V step-down transformer, rectifier diodes, filter inductor, resonant inductor, resonant capacitor, and SCR that is anti-paralleled with a freewheeling diode and capacitor. The resonant capacitor is in series with the primary side of the high-frequency transformer, while the secondary side is in series with the load.

The switch adopts the thyristor model in Simulink/MATLAB, which its control signal utilizes pulse frequency modulation (PFM) to trigger the state of the switch. The frequency of the control signal, its duty cycle of the high level is 4%, can be adjustable from 7 to 18 kHz. In addition, the parameters of the main circuit in the simulation are as follows (Table 1).

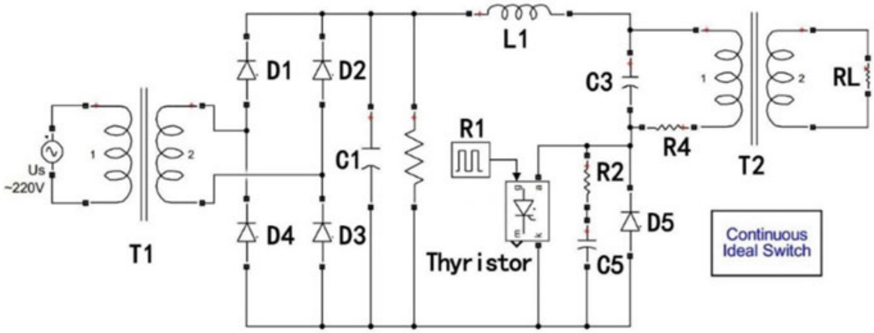

Fig. 2 Main circuit simulation model of high-voltage plasma power supply

Table 1 Parameters of the main circuit

Input voltage Us(V)	220
Isolation transformer T1 turns ratio	2:1
Step-up transformer T2 turns ratio	1:40
Transformer equivalent leakage inductance (mH)	8
Filter capacitor C1 (μF)	2200
Resonant inductor L1 (mH)	36
Resonant capacitor C3 (μF)	1
Snubber resistor R2 (kΩ) and capacitor C5 (μF)	3/0.1
Current limiting resistor R4 (Ω)	1.5

3.2 Simulation Results

The main waveform diagram of the main circuit simulation of the high-voltage plasma power supply is shown in Fig. 3. The simulated thyristor trigger pulse frequency is 8 kHz, corresponding to the short pulse waveform in the fourth waveform diagram of Fig. 3.

From Fig. 3, the resonant capacitor C3 voltage is charged to saturation at $t1$, the inductor L1 current is reversed, and the thyristor is naturally turned off, achieving ZCS. The resonant current is zero-crossed for the second time at $t2$, and the free-wheeling diode is turned off in reverse. Meanwhile, the thyristor is already in the OFF state, and the voltage across the thyristor rises at this time. As shown in Fig. 4, when the thyristor control signal is 7 kHz, the high-voltage transformer $t2$ boosts the primary side resonance voltage to the 15-kV level.

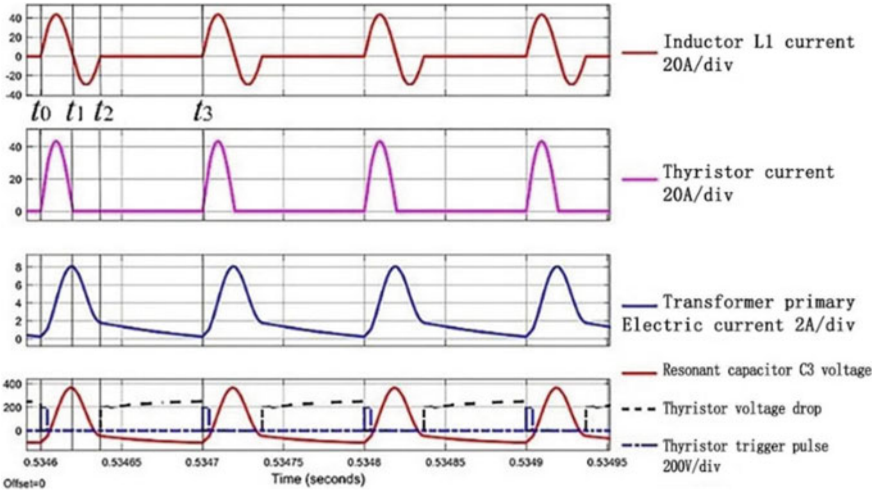

Fig. 3 Main waveform of simulation

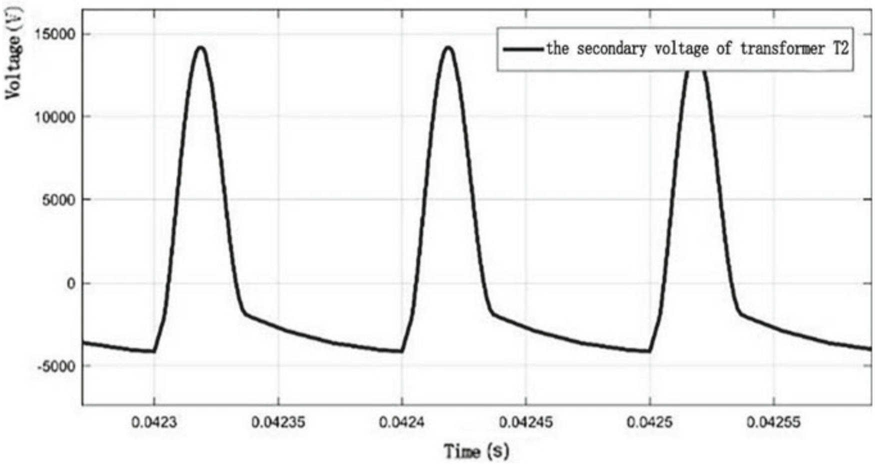

Fig. 4 Output voltage of the secondary T2

4 Design of High-Voltage Plasma Power Supply

4.1 Design of Control Circuit

The block diagram of the control circuit is shown in Fig. 5. The control circuit is based on the microchip STM32F103cbt6. Meanwhile, the main circuit version integrates 232 communication module, LCD display module, power supply circuit, thyristor

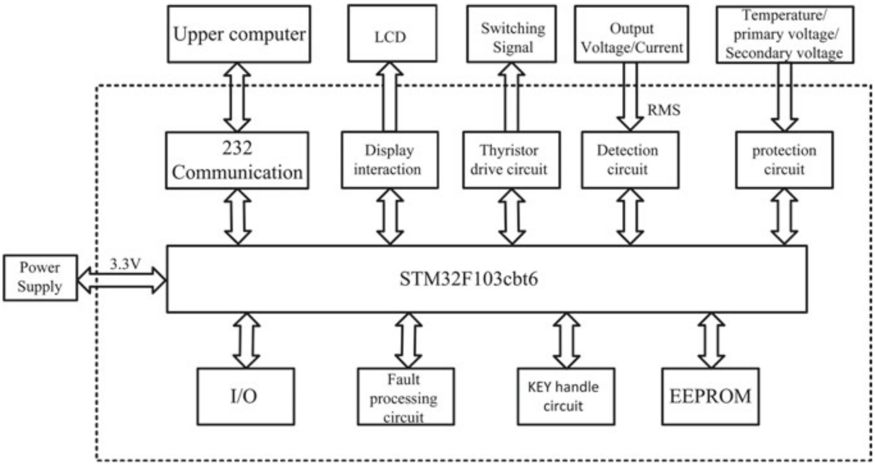
Upper computer
LCD
Switching Signal
Output Voltage/Current
Temperature/ primary voltage/ Secondary voltage
RMS
232 Communication
Display interaction
Thyristor drive circuit
Detection circuit
protection circuit
Power Supply
3.3V
STM32F103cbt6
I/O
Fault processing circuit
KEY handle circuit
EEPROM

Fig. 5 Block diagram of control circuit

drive circuit, voltage and current detection circuit, protection circuit, I/O interface, fault processing circuit, key handle circuit, and EEPROM memory.

The operation instructions sent by the upper computer are transmitted to the microchip through RS232, and then the microchip sends control instructions to each module. After the main circuit works normally, through Hall sensor, the voltage and current detection circuit collects voltage and current outputting from main circuit which will be calculated as a RMS value and passed into the microchip. The RMS value of the output voltage and current can be displayed on the LCD screen through software programming. During the operation of the main circuit, it is necessary to provide protection for the power supply. In this part, the temperature switch is added to the protection circuit; moreover, the upper limit of output voltage, primary current, and the power supply in time display the fault type. At last, the EEPROM memory saves the set parameters and restores the original settings after power off.

The flow diagram of the main program is shown in Fig. 6.

A high-voltage plasma prototype is built according to the circuit mentioned above, and then the prototype is debugged on the experimental platform. The scene picture is shown in Fig. 7. The main modules of the prototype are as follows: ① control board; ② LCD screen; ③ the rectifier bridge and SSR; ④ SCR; ⑤ start button; ⑥ 220 V/110 V transformer.

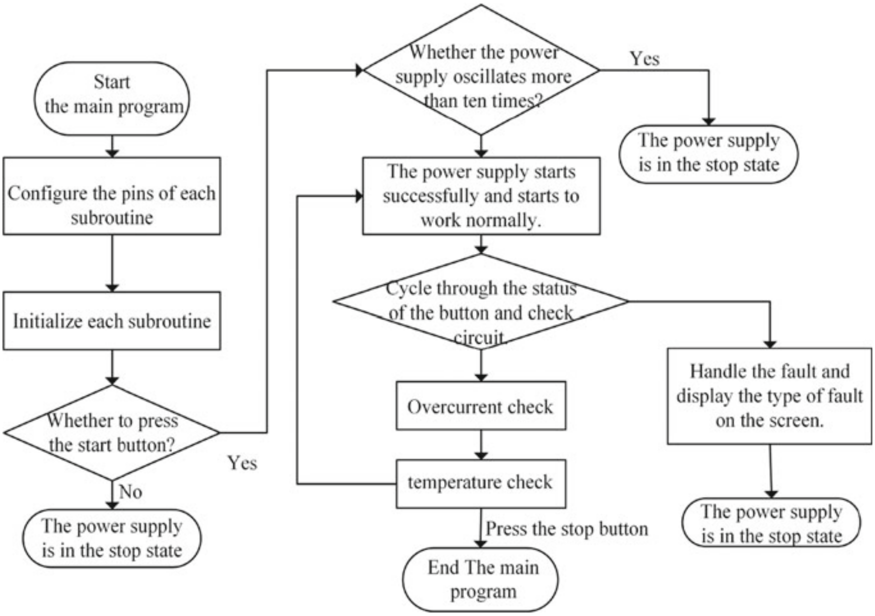
Start
the main program
Configure the pins of each subroutine
Initialize each subroutine
Whether to press the start button?
Yes
No
The power supply is in the stop state
Whether the power supply oscillates more than ten times?
Yes
The power supply is in the stop state
The power supply starts successfully and starts to work normally.
Cycle through the status of the button and check circuit
Overcurrent check
temperature check
Press the stop button
End The main program
Handle the fault and display the type of fault on the screen.
The power supply is in the stop state

Fig. 6 Flow diagram of the main program

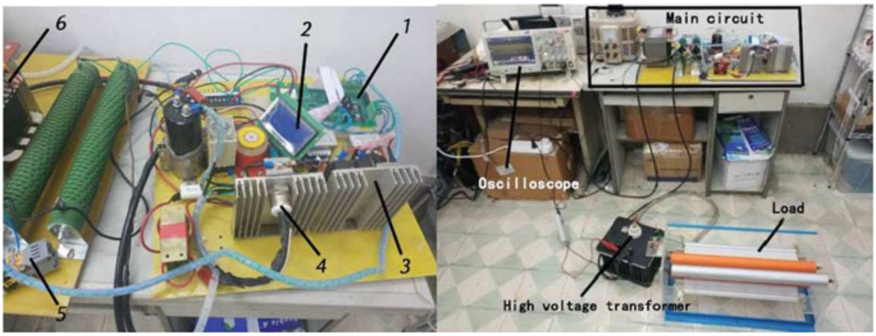

Fig. 7 Picture of experimental scene

4.2 Experimental Waveform

As shown in Fig. 8, the peak-to-peak value of the output voltage is 14.6 kV at 7 kHz. The peak value of the voltage is the same as the simulation data. Comparing Figs. 3, 4, 8 and 9, it can be found that the driving signal waveform of the thyristor in prototype is the same as the waveform in simulation. Also, both output voltages in simulation and experiment are all complete sinusoidal waveforms with the same peak voltage. The prototype experiment further validates the consistency of the theoretical and simulation models.

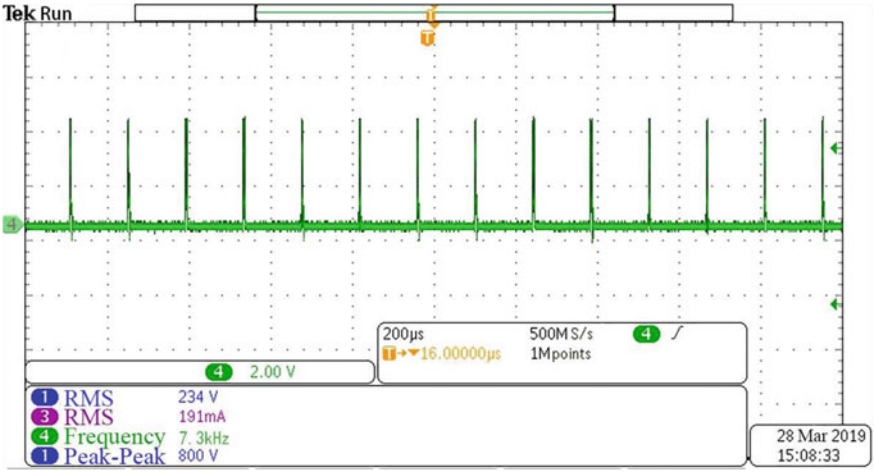

Fig. 8 Waveform of drive signal

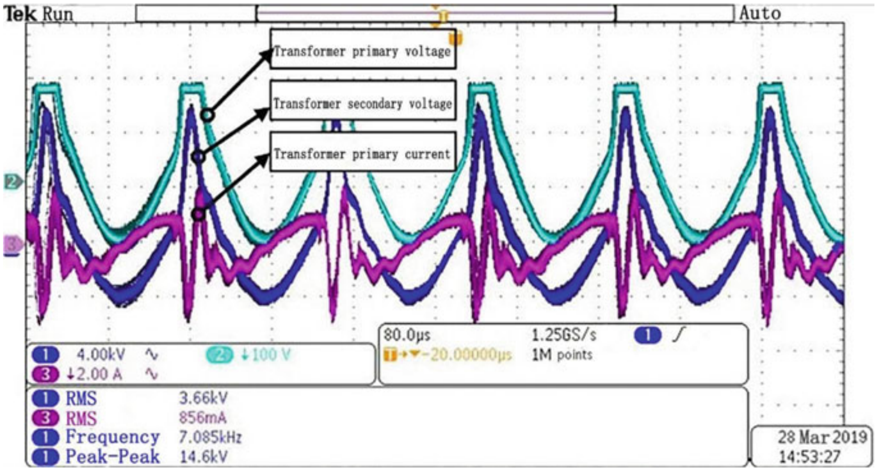

Fig. 9 Waveform of 7 kHz output

5 Conclusion

In this paper, the main circuit of high-voltage plasma power supply is designed based on resonant converter. The control scheme adopts pulse width frequency modulation (PFM). Therefore, the output voltage can be adjusted by the frequency of the switching signal to achieve the purpose of boosting. Then, the simulation interface of MATLAB/Simulink is used to verify the function of the circuit. At last, the prototype is made and debugged, and the experimental waveform is consistent with waveform in the simulation which proves the reliability of the high-voltage plasma power supply.

Acknowledgements Thanks for the Nation-supported Program(2018YFD0400903). Thanks for the National Defense Key Disciplines Laboratory of Light Alloy Processing Science and Technology, Nanchang Hangkong University (EG201780504).

References

1. Zhang Chunxia (2019) Application of power electronics technology in switching power supply. Int Circ Appl 36(04):63–64
2. Scholtz JS, Fontana LC, Mezaroba M (2018) Asymmetric bipolar plasma power supply to increase the secondary electrons emission in capacitive coupling plasmas. IEEE Trans Plasma Sci 46(8):2999–3007
3. Supanarapan T, Marungsri B (2018) Optimal power supply frequency for wastewater treatment by using underwater plasma discharges. In: Proceedings of the 2018 2nd international conference on electrical engineering and automation (ICEEA 2018)

4. Ctibor P, Hrabovsky M (2010) Plasma sprayed TiO_2: the influence of power of an electric supply on particle parameters in the flight and character of sprayed coating. J Eur Ceram Soc. 30(15):3131–3136
5. Songjiang Li (2016) Study on the forward-flyback PFC converter with quasi-resonant (QR) control. Hang-zhou University of Electronic Science and Technology

Information for Authors

Aims and Scopes

Transactions on Intelligent Welding Manufacturing (TIWM) is authorized by Springer for periodical publication of research papers and monograph on intelligentized welding manufacturing (IWM).

The TIWM is a multidisciplinary and interdisciplinary publication series focusing on the development of intelligent modeling, controlling, monitoring, and evaluating and optimizing the welding manufacturing processes related to the following scopes:

- Scientific theory of intelligentized welding manufacturing
- Planning and optimizing of welding techniques
- Virtual and digital welding/additive manufacturing
- Sensing technologies for welding process
- Intelligent control of welding processes and quality
- Knowledge modeling of welding process
- Intelligentized robotic welding technologies
- Intelligentized, digitalized welding equipment
- Telecontrol and network welding technologies
- Intelligentized welding technology applications
- Intelligentized welding workshop implementation
- Other related intelligent manufacturing topics

Submission

Manuscripts must be submitted electronically in WORD version on online submission system: https://ocs.springer.com/ocs/en/home/TIWM2017. Further assistance can be obtained by emailing Editorial Office of TIWM, Dr. Yan ZHANG: zm_1977nsh@163.com, or anyone of the Editors-in-chief of TIWM.

© Springer Nature Singapore Pte Ltd. 2020

S. Chen et al. (eds.), *Transactions on Intelligent Welding Manufacturing*,
Transactions on Intelligent Welding Manufacturing,
https://doi.org/10.1007/978-981-15-7215-9

Style of Manuscripts

The TIWM includes two types of contributions in scopes aforementioned, the periodical proceedings of research papers and research monographs. Research papers include four types of contributions: Invited Feature Articles, Regular Research Papers, Short Papers, and Technical Notes. It is better to limit the full length of Invited Feature Articles in 20 pages; Regular Research Papers in 12 pages and Short Papers and Technical Notes both in six pages. The cover page should contain paper title, authors name, affiliation, address, telephone number, email address of the corresponding author, abstract (100–200 words), keywords (3–6 words) and the suggested technical area.

Format of Manuscripts

The manuscripts must be well written in English and should be electronically prepared preferably from the template "splnproc1110.dotm" which can be downloaded from the website: http://rwlab.sjtu.edu.cn/tiwm/index.html. The manuscript including texts, figures, tables, references, and appendixes (if any) must be submitted as a single WORD file.

Originality and Copyright

The manuscripts should be original and must not have been submitted simultaneously to any other journals. Authors are responsible for obtaining permission to use drawings, photographs, tables, and other previously published materials. It is the policy of Springer and TIWM to own the copyright of all contributions it publishes and to permit and facilitate appropriate reuses of such published materials by others. To comply with the related copyright law, authors are required to sign a Copyright Transfer Form before publication. This form is supplied to the authors by the editor after papers have been accepted for publication and grants authors and their employers the full rights to reuse of their own works for non-commercial purposes such as classroom teaching.

Author Index

B
Bu, Wende, 27

C
Cao, Yingyu, 125
Chen, Shanben, 3, 57

F
Fan, Ding, 45
Fang, Wei, 125
Feng, Zhiqiang, 137
Fu, Zhihe, 75

H
Han, Junfeng, 137
Hu, Ande, 45
Huang, Jiankang, 45
Huang, Jiqiang, 125
Huang, Junfen, 125
Huang, Kang, 125
Hu, Yu, 75
Hu, Zixin, 149

K
Ke, Liming, 27

L
Lan, Hu, 109
Li, Gang, 109
Li, Huijun, 57
Lv, Na, 137

P
Pan, Rui, 109
Pan, Zengxi, 57
Polden, Joseph, 57

S
Shao, Jinjun, 109
Shi, Yonghua, 93
Sun, Wenjun, 27

W
Wang, Bin, 109
Wang, Shanlin, 27
Wang, Zhuoran, 149

X
Xia, Chunyang, 57
Xie, Huangsheng, 75
Xue, Jiaxiang, 75
Xue, Long, 125
Xu, Jingyuan, 3

© Springer Nature Singapore Pte Ltd. 2020
S. Chen et al. (eds.), *Transactions on Intelligent Welding Manufacturing*,
Transactions on Intelligent Welding Manufacturing,
https://doi.org/10.1007/978-981-15-7215-9

Xu, Yanling, 57
Xu, Zhenya, 45

Y
Yang, Dapeng, 137
Yuan, Song, 149

Z
Zeng, Min, 149
Zhang, Baori, 93
Zhang, Huajun, 109
Zhang, Shiyu, 57